Abstract

This thesis discusses the dynamics and structure of suspensions of near hard-sphere colloidal particles. The colloidal PMMA (Polymethylmethacrylate) particles studied are sterically stabilised by coating with thin PHSA (Poly-12-hydroxystearic acid) layers. Such PMMA colloidal suspensions show phase behaviour which is similar to simple atomic systems, such as rare gases. Therefore, they serve as analogues for atomic materials.

In chapter 2 the Brownian motion of particles in a very dilute system is studied by dynamic laser light scattering. The scattered field autocorrelation function is processed to investigate particle diffusion. As a result, not only particle size can be measured but also the polydispersity (the standard deviation of the particle size distribution divided by the mean size) of the sample system can be estimated. We also describe an attempt to fractionate a polydisperse system.

Chapter 3 mainly reports on the study of the colloidal crystals formed at high particle concentrations. The close-packed random-stacked structure with a high degree of randomness found in our samples has never been observed in atomic materials. The theory developed by A. J. C. Wilson introduces the faulty stacking probability, α, to characterise the close-packed random-stacked structures. A model is then established to analyse the data by reference to the theory. The experimental results suggest that the observed random-stacked structure is metastable and that the equilibrium structure is

probably face-centred cubic rather than hexagonal close-packed. The other intriguing phenomenon is that the structure of colloidal crystals changes with time. A possible explanation is offered and an attempt is made to improve the theory.

Declaration

This thesis has been composed by myself and it has not been submitted in any previous application for a degree. The work reported within was executed by me, unless otherwise stated.

October 1994

Acknowledgements

I would like to take this opportunity to express my thanks to many people who helped me with this work. Firstly, my principal acknowledgement should go to my supervisors: Professor Peter Pusey and Dr Wilson Poon. To Peter, who leads me to unearth new phenomena and overcome some difficulties, I owe him a great debt for many inspiring discussions. And thanks to Wilson for his keen inspection at all stages of this work.

To each of my colleagues in the group of soft-condensed matter, I am very grateful. They are Dr Steve Ilett, Dr Phil Segrè, Mr Angus Pirie, Mr Mark Haw, and many others. I will cherish the friendship forever.

The colloidal particles used were kindly donated by Professor R. H. Ottewill of Bristol University and Dr S. M. Underwood of the Royal Melbourne Institute of Technology. My thanks are also due to them.

All the equipment in the light scattering laboratory were carefully maintained by technicians. Without their service, the experiments would not have gone smoothly. Therefore, I have to thank Mr H. Vass and Mr S. Duffield.

Finally and above all, I would like to record my sincere gratitude to my parents for their financial support and constant encouragement. When I was confronted with tough conditions and my research work was deadlocked, their inspiration helped me to pass this dark period. Eventually, all the difficulties were overcome.

Contents

List of Tables

List of Figures

Chapter 1

General introduction

The term "colloid" was coined by Thomas Graham in 1861 to distinguish types of matter. Colloidal suspensions are defined as complex fluids which consist of a liquid where particles, much larger than the molecules of the suspension medium, are suspended. The radius of colloidal particles is set in the range $1nm \lesssim R \lesssim 1000nm$. The upper and lower limits confirm that the particle motion is not dominated by extraneous effects such as gravitational settling and that the particle is larger than the molecules of the suspension medium, respectively. However, there is no sharp distinction between colloidal and non-colloidal systems. [1]

The study of colloidal suspensions has been developing for many decades, such as dynamic and thermodynamic properties, phase behaviour, and structure factor of colloidal systems. The structure and dynamics of colloidal systems can be studied by light scattering experiments. Light scattering techniques have been used comprehensively in many fields for more than two decades. Owing to the coherence and stable amplitude of laser, a dynamic laser light scattering experiment exploits laser light to provide information about the dynamics of Brownian particles in colloidal suspensions. A static laser light scattering experiment is also applicable to the study of the structure of colloids because the wavelength of a visible laser beam is comparable with the

interparticle spacing of colloidal systems.

In chapter 1, the motives of this study and the sample system are introduced. We also describe how to make a near index matched sample which is suitable for light scattering experiments. In addition, the phase behaviour of a pure colloidal system is illustrated. An intriguing phenomenon, crystallisation (or disorder-order transition) of hard spheres, is discussed in the final section.

Chapter 2 reports on the fundamental theory of light scattering and explains the way in which the scattered light by colloidal dispersions can be used to study particle diffusion. We also describe a technique established to measure the polydispersity (the standard deviation of the particle size distribution divided by the mean size) of colloidal suspensions. Based on the success of this technique, an attempt was made to fractionate a polydisperse system.

The main new research in this thesis, reported in chapter 3, deals with the structures of colloidal suspensions, in particular colloidal crystals. The quantitative and qualitative interpretation of the scattered pattern by colloidal crystals are made by reference to the theory developed by A. J. C. Wilson. Some new results are reported and possible interpretations are also offered.

1.1 Motivations

Colloidal systems have drawn the attention of scientists for the past two decades, colloid plus polymer mixtures appeal to them as well. In the realm of application a range of industrial and agricultural products, such as paints, inks, reinforced plastics, many foodstuffs such as milk and other dairy products can be considered to be mixtures of colloidal components. In addition, many biological materials, such as tissue and blood

cells can be described as colloidal particles, interacting with other colloidal and non-colloidal constituents of a living system [2].

Many fascinating phenomena are encountered in the study of colloidal suspensions, for example, the diffusion of the particles, phase transitions, and the kinetics and mechanism of crystallisation. Colloidal suspensions also serve as analogues for atomic materials. The small size and short relaxation time of atoms prevent the experimental study of topics, such as kinetics and mechanism of crystallisation, for atomic systems. This leads to an attempt to study these effects by means of their colloidal analogues. Typically, a colloidal particle is 10^3 times larger than an atom. The relaxation time, which is the time taken by the particle to diffuse a distance equal to the radius, of an atomic material is about 10^9 times shorter than that of a typical colloid. A dilute suspension is structurally similar to an ideal atomic gas; at higher suspension concentrations, the particles develop short-ranged positional correlations similar to those of atoms in a dense liquid; at still higher concentrations, colloidal crystals are formed. Therefore, the study of colloidal suspensions provides a variety of feasible approaches to study some phenomena of fundamental physics. [1][2][3][4]

1.2 Sample system

The colloidal particles used in this thesis consist of Polymethylmethacrylate (PMMA) "core" with Poly-12-hydroxystearic acid (PHSA) "shell". Particles used were kindly donated by Professor R. H. Ottewill of Bristol University and Dr S. M. Underwood of the Royal Melbourne Institute of Technology. In the preparation procedure used by them the PMMA core was coated with a close-packed layer of PHSA whose thickness is small compared to the core radii. The thickness of the stabiliser layer was about $10nm$, a small fraction of the particle radius. Therefore, the colloidal particles studied here are sterically-stabilised and can be regarded as hard spheres. There are two effects that have to be emphasised. Firstly, the configurational entropy of the attached polymer,

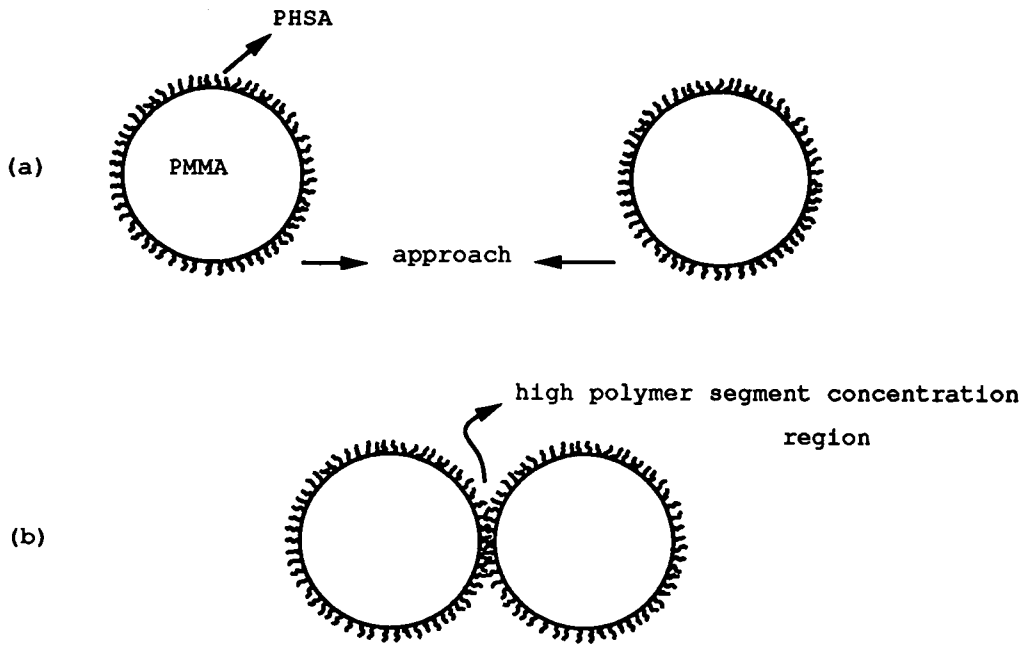

Figure 1.1. From stage (a) to stage (b) configurational entropy of attached polymer is lost and a local "osmotic pressure" is caused by the higher polymer concentration region.

PHSA layer, will be lost when two colloidal particles approach. This is called "volume restriction effect". Secondly, when the layers of two colloidal particles overlap, the high polymer segment concentration between them will lead to a local "osmotic pressure", counteracting the approach in our system. Figure 1.1 illustrates the mechanisms of this model system in steric stabilisation [5].

In general, the total interaction potential of sterically-stabilised particles is the sum of the steric contribution and a van der Waals attraction. The schematic plot of the potential of average force is shown in figure 1.2. The depth of the pair potential for sterically-stabilised colloidal particles immersed in a suspension medium whose refractive index is very close to that of colloidal particles may be many times smaller than kT, and the width very small with respect to the particle size. The similarity of near

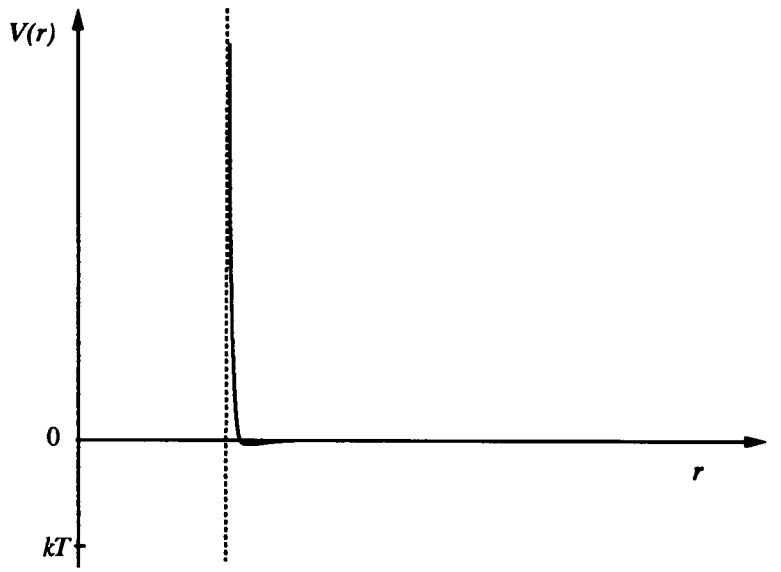

Figure 1.2. Schematic plot of the potential of average force, $V(r)$, for sterically-stabilised particles with repulsive "volume restriction" force plus repulsive local "osmotic" force plus attractive van der Waals force.

hard-sphere colloidal suspensions to simple liquids is due to the similar shape of their pair potentials, although there can be important differences in the depth and the width of the potential well [5]. Moreover, an ideal single-size or monodisperse colloidal system is impossible to obtain. Typically, the polydispersities of the colloidal suspensions used here are about 5%. This is an important difference between atoms and colloids.

1.3 Sample preparation

The stock solution of PMMA latex stabilised by PHSA was prepared. The density of PMMA particles is taken as $1.188 \pm 0.001 gm/cm^3$, the density of bulk PMMA (perspex). The suspension medium is cis-decalin whose density is $0.894 \pm 0.001 gm/cm^3$ and refractive index 1.481 [6]. Concentration is measured in terms of volume fraction ϕ, defined as the volume V of a sample occupied by N particles, $\phi = \frac{4}{3}\pi R^3 \frac{N}{V}$. Usually, the volume fraction of the stock solution was controlled to be about 0.30. Square $1 \times 1 cm^2$

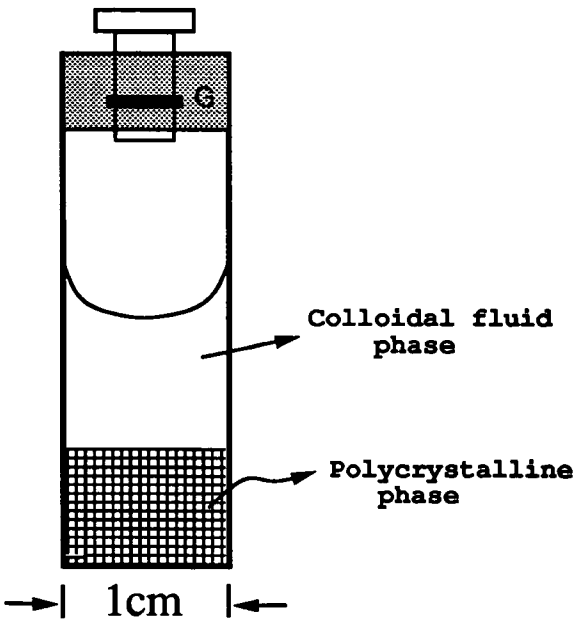

Figure 1.3. A square $1 \times 1cm^2$ cross section sample cell was used in a light scattering experiment. The colloidal fluid and solid coexistence phase is demonstrated.

sample cells (shown in figure 1.3) were used in a light scattering experiment. To do a light scattering experiment, the refractive index of solvent needs to be close to that of the colloidal particles, 1.500 ± 0.005, so that multiple scattering is minimised. This near index-matching situation could be achieved by adding filtered tetralin whose refractive index is 1.541 (density $0.973 \pm 0.001 gm/cm^3$ [6]) until the transmission through the cell was about 90% for red line of a He-Ne laser. If the ratio by volume of tetralin to solvent (cis-decalin + tetralin) is around 0.30, the red line of He-Ne laser having transmission through the sample of about 90% can be reached.

To make a highly concentrated sample, it is required to centrifuge the particles down in the sample cell with weighed stock solution and then remove a weighed amount of supernatant, cis-decalin. Afterwards, a weighed amount of filtered tetralin chosen to achieve the volume ratio of tetralin to solvent, about 0.30, has to be added in the cell to approximately match the refractive index of the particles. Empirically, the error of

the volume fraction of the sample made is estimated to be about 0.001.

1.4 Phase behaviour

Colloidal suspensions undergo phase transitions analogous to those observed in simple atomic systems. Disordered fluid and ordered crystalline phases can be observed in colloidal systems as in atomic systems, and phase transitions can also be observed. The phase behaviour of concentrated suspensions of nearly hard colloidal spheres has been comprehensively studied by Pusey and others [7][8]. The slight difference between experiment and theory has also been pointed out. Whereas computer simulations use identical and hard spheres, those in our sample system are nearly hard spheres and slightly polydisperse.

The phase diagram of nearly hard colloidal spheres is shown in figure 1.4. The freezing and melting concentrations of hard spheres obtained from computer simulations [9][10] are 0.494 and 0.545, respectively. This result is different from that of a real colloidal system. To compare with hard-sphere theory, it is common to scale [7][8] the measured "core" volume fraction to coincide with the theoretical hard-sphere freezing point. The volume fraction of PMMA cores can be calculated by assuming that the PHSA coating contributes a negligible amount to the mass of the particles and by taking literature values for the density of PMMA and suspension medium (see section 1.3). Therefore, the effective hard-sphere volume fraction ϕ_E is defined as $(\frac{0.494}{\phi_f})\phi$, where ϕ_f is the measured freezing point and ϕ the measured core volume fraction. The measured freezing point ϕ_f is not universal and depends on the characteristics of the sample system used, such as particle polydispersity. However, by using this scaling factor these authors found that the effective radius increment for the particles is about the thickness of the stabiliser layer.

Particle diffusion in colloidal fluid phase has been comprehensively studied [1]. In an

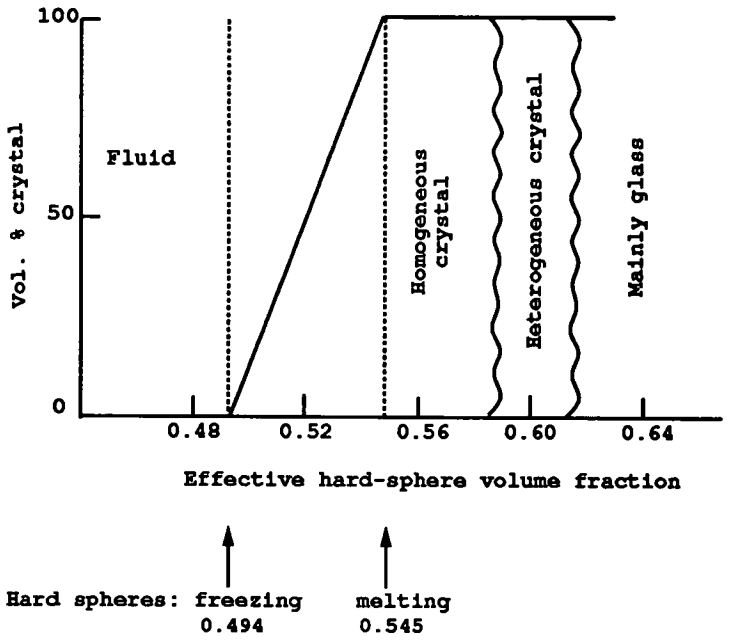

Figure 1.4. Phase diagram of nearly hard colloidal spheres. Arrows at the bottom indicate the volume fractions, obtained from computer simulations. See text for details. (After Pusey and van Megen)

extremely dilute system (called a colloidal gas), the free particle diffusion coefficient can be easily disclosed by the use of a dynamic light scattering experiment (see chapter 2). At higher concentrations, the positions of colloidal particles are no longer independent although the distribution of colloidal particles in solvent is random. Not only the short-range correlations between the positions of neighbouring particles become significant, but also hydrodynamic interaction appears. These effects make the diffusion of colloidal particles at high concentrations very complicated. However, it is believed that a fairly complete understanding of colloid diffusion at high concentrations can be achieved within the next decade [4].

For $\phi > 0.494$, a polycrystalline phase can be obtained. Between the freezing and melting concentrations shows that the equilibrium state is a coexistence of fluid ($\phi = 0.494$) and crystal ($\phi = 0.545$), and phase separated by a visible boundary due to

gravitational settling of the crystallites. For $\phi > 0.545$, small compact crystallites which fill the cell are observed. The crystal structures of the polycrystalline phases were found to be closed-packed random-stacked structures by light scattering experiments (See chapter 3.). For $\phi > 0.58$, amorphous or glassy phases and partially heterogeneous crystallisation region will appear. After slowly tumbling the samples, one can obtain reproducible metastable fluid phases. If samples are left undisturbed again, the range of behaviour mentioned above will reoccur, corresponding to the appropriate volume fractions.

1.5 Disorder-order transition

It might seem puzzling that sterically-stabilised colloidal particles, almost with no interparticle attraction, could crystallise. Kirkwood, offering a speculation to explain the unusual phenomenon of the limiting value of a single parameter λ in his calculation when he developed a theory of the radial distribution function in nonpolar liquids composed of spherical molecules, is the first to point out the possibility of freezing transition for hard spheres [11]. A model of hard spheres representing a particle that only shows interaction when touching was adopted by Hoover *et al.* [9][10]. Through their computer simulation work the freezing point and melting point of hard spheres are located at $\phi_f = 0.494$ and $\phi_m = 0.545$, respectively. Detailed experimental observation [7][8] (described in the previous section) supported this argument.

The disorder-order transition has been studied recently through density functional theory [12]. In this theory the freezing of hard spheres can be described as a competition between the "configurational entropy" s_{conf} favouring disorder and the "correlational entropy" s_{corr} favouring localisation. The liquid-solid coexistence is determined by finding a liquid and a solid that have the same pressure and the same chemical potential at constant temperature. Recall that $\triangle f = \triangle u - T\triangle s$, where f is the Helmholtz free energy per unit volume, u and s are the internal energy and the entropy per unit

volume, respectively. In the case of hard spheres, there is no contribution to the internal energy from potential forces. Therefore, even though this argument (disorder-order transition) has been formulated in recent density functional theory calculation [12], it is still necessary to give a clear picture to interpret "'correlational entropy".

The latest interpretation of disorder-order transition of hard spheres introduced the concept of "free-volume entropy" [14][15]. It is well known that a fluid is more disordered than a solid in spatial configuration (see figure 1.5). According to the second law of thermodynamics, equilibrium is a state of maximum entropy (maximum disorder). In the case of hard spheres, there is no contribution to internal energy from potential energy. If there only exists "configurational entropy" in the system, then solid phase will never occur. However, as Ackerson [15] remarked "Locally, however, there is more jamming together in the random structure than in the crystalline structure. Thus, there are more ways or possibilities for moving the particles around a little bit in the crystalline state than in the random structure." (see figure 1.5). The local free volume then plays a crucial role in favouring solid phase. Once the gain in "free-volume entropy" exceeds the loss in "configurational entropy", the disorder-order transition could occur.

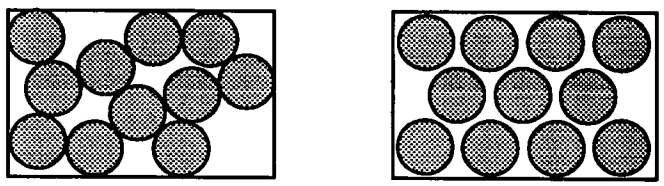

Figure 1.5. (a) A disordered arrangement of hard spheres in which the configurational entropy is high, but the free-volume entropy is low (for the spheres can not move). (b) An ordered arrangement of hard spheres in a box of the same size in which the free-volume entropy is high (there is more room for spheres to undergo local motions) but the configurational entropy is low. (After H. N. W. Lekkerkerker, unpublished.)

Chapter 2

Dynamic light scattering

2.1 Introduction

The main idea of this chapter is to review the general theory of light scattering and to explain the way in which the fluctuating intensity of the light scattered by colloidal suspensions can be used to study the dynamics of colloids: the technique of dynamic light scattering (DLS).

The polydispersity (the standard deviation of particle size distribution divided by the mean size) of colloidal suspensions plays an important role in the diffusion process of the particle, and will influence the behaviour of colloidal phase transition [16][17]. Therefore, it is necessary to measure the polydispersity of the sample system. One of the techniques of measuring polydispersity is via the use of dynamic laser light scattering [18][19]. Since about 1970, analysis of the fluctuating intensity in a DLS experiment has usually been performed by the technique of "photon correlation spectroscopy" (PCS) [20][21]. Through the investigation of the diffusion process of colloidal particles, one can calculate the hydrodynamic radius of the particle if the sample system is extremely dilute. As a result, one can establish a technique to measure the polydispersity of the sample system in a more objective way.

In section 2.2, a methodical derivation of the Brownian dynamics of colloidal particles is discussed. Section 2.3 mainly describes how the correlation function of the scattered intensity is analysed. This section is quite mathematically oriented but helpful to explain the experimental results. In section 2.4, we present the light scattering experiment. The last section explains the results and describes some experimental difficulties. Additionally, suggestions for future work are offered.

2.2 Theory

2.2.1 Light scattering theory

Our interest in dynamic light scattering comes from the phenomenon observed in a simple light-scattering experiment that fluctuating speckle patterns can be seen if a screen is placed in the region around the forward laser beam which is previously passed through a dilute sample of colloidal suspension. Unlike Young's experiment in which the observed interference pattern is *stationary*, this simple experiment gives a *fluctuating* speckle pattern. If another sample consisting of only pure solvent replaces the dilute suspension, there will be no fluctuating pattern on the screen. Now we can make a conclusion that the fluctuating speckle patterns must be due to the constructive and destructive interference of scattered light by particles suspended in solvent. Therefore, to explain the fluctuating speckle patterns, it is necessary to understand the theory of light scattering by particles.

The classical theory of light scattering [22] describes that an incident electromagnetic field exerts a force, known as Lorentz force, on the charges in the scattering volume. The charges then accelerate and radiate light. Owing to the oscillation of electromagnetic field an instantaneous dipole moment induced by incident electric field will oscillate. Each dipole oscillator can be regarded as a scattering element. If many volume elements of equal size are considered, the scattered electric field is the superposition of the

scattered fields from each of them. If the scattering volumes are optically identical, there will be no scattered light. This is because the wavelet scattered from each volume element is identical. Each scattering volume is paired with another scattering volume whose scattered field is identical in amplitude but opposite in phase and thus scattered light will cancel, leaving no net scattered light. In practice, the scattering volumes are optically different due to the fluctuation of polarizability α of scattering volume. In a solution of polarizability different from that of the solvent, fluctuations in α will be caused by local concentration fluctuations. This induces the fluctuation theory of light scattering. One of the examples is the light scattered by solvent in a light scattering experiment in which a laser beam is sent to pass through a sample of pure solvent. The scattered light, which is very weak and usually can be ignored in our light scattering experiments, is just due to inhomogeneities in the polarizability of solvent.

A theory different from fluctuation theory is the particle scattering theory that each particle in suspension medium is considered to be a scattering entity, with scattering amplitude f_j. Consider the scattering of light from a collection of identical spherical particles at positions $\{\mathbf{r}_j(t)\}$. We assume that the scattering by each particle is weak, which will be the case if the Rayleigh-Gans-Debye (RGD) [18][22] condition is satisfied:

$$RGD \equiv (4\pi/\lambda_o)\bar{R}\triangle n \ll 1 \tag{2.1}$$

where $\triangle n = n - n_o$, n the refractive index of the particle, n_o the refractive index of solvent, $\bar{R}$ the particle mean radius, λ_o the wavelength of the incident light in vacuum. RGD criterion indicates that the phase shift $\triangle\phi$ in the particle is approximated to zero if the incident light passes through an extremely-low potential barrier particle. The RGD criterion, a classical approximation, is equivalent to the first Born approximation in quantum mechanics [23]. If the refractive index of scatterer is very close to that of solvent, the potential barrier of scatterer is relatively very small in comparison

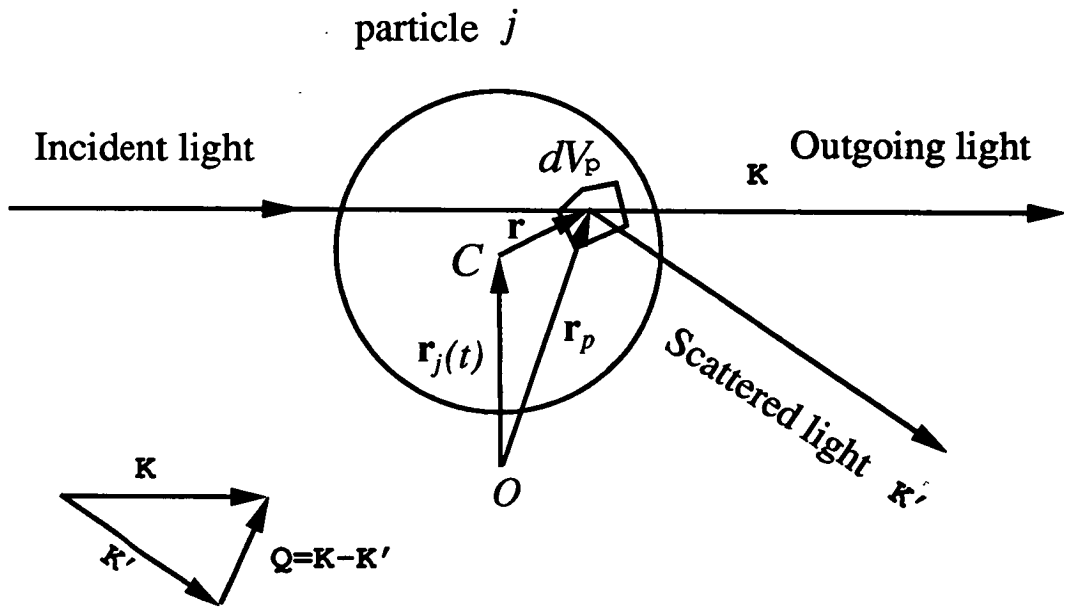

Figure 2.1. Typical scattering geometry

with the energy of incident light in solvent. The first-order Born amplitude can then approximately describe the scattered electric field amplitude by particle j which is only one-step process of scattering in scatterer. The electric field scattered by particle j at scattering vector $\mathbf{Q}$ (see figure 2.1) is given by

$$E_j(Q) \propto \int_{V_j} dV_p \triangle n(r_p) \exp(i\mathbf{Q} \cdot \mathbf{r}_p)$$

$$= \exp i\,[\mathbf{Q} \cdot \mathbf{r}_j(t)] \int_{V_j} dV_p \triangle n(r_p) \exp(i\mathbf{Q} \cdot \mathbf{r}) \qquad (2.2)$$

where r_p is the distance from a scattering element dV_p to the origin O, C the central position of the particle, $\mathbf{r}_p = \mathbf{r}_j(t) + \mathbf{r}$, $\exp(i\mathbf{Q} \cdot \mathbf{r}_p)$ the phase factor, $\triangle n(r_p)$ the difference of refractive index between scattering element dV_p and solvent, and $\mathbf{Q}$ the

scattering vector whose magnitude is given by

$$Q = \frac{4\pi}{\lambda} \sin \frac{\theta}{2} \tag{2.3}$$

λ the wavelength of incident light in solvent, θ the scattering angle (see figure 2.1). Assume the spatial density distribution of scattering material inside the particle, a homogeneous hard sphere, is uniform so as to simplify the calculation, then $\Delta n(r_p) = n - n_o$ is a constant. Hence, the amplitude of the E-field scattered by a single particle can be mathematically evaluated. We can set

$$f_j(Q) = \int_{V_j} dV_p e^{i\mathbf{Q}\cdot\mathbf{r}}, \tag{2.4}$$

omitting constants of proportionality. This equation, which reflects intraparticle interference, describes the internal structure of a particle because every scattering element in the particle contributes. In our model system the particle is a hard sphere. Accordingly, equation (2.4) becomes

$$f_j(Q) = \int_{r=0}^{R} \int_{\theta=-\pi}^{\pi} \int_{\phi=0}^{2\pi} r^2 dr \sin\theta d\theta d\phi e^{i\mathbf{Q}\cdot\mathbf{r}} \tag{2.5}$$

where R is the radius of the particle. By reference to spherical co-ordinates, and $\mathbf{Q}\cdot\mathbf{r} = Qr\cos\theta$, then equation (2.5) can be evaluated further to give

$$\begin{aligned} f_j(Q) &= 4\pi \int_0^R dr\, r^2 \frac{\sin Qr}{Qr} \\ &= \frac{3}{Q^3}(\sin QR - QR\cos QR) \end{aligned} \tag{2.6}$$

Traditionally, we write $P(QR) = f^2(Q)/f^2(0)$, defining the single particle form factor (normalised to one at $Q = 0$):

$$P(QR) = \frac{9}{(QR)^6}(\sin QR - QR\cos QR)^2. \tag{2.7}$$

Note that $f(0) = R^3$. So far the scattering amplitude f_j by particle j has been obtained. The next step is to understand fluctuating speckle patterns. In a light scattering experiment the speckle patterns come from the constructive and destructive interference of scattered light by different particles and is randomly fluctuated due to the random thermal motion of Brownian particles (see section 2.2.3). This intensity fluctuation implies the process of particle diffusion. Thus, we can investigate the dynamics of the particles by studying the fluctuating speckle patterns. The reason why the fluctuating speckle patterns disclose the dynamics of the Brownian particles can be explained as follows:

In a dilute enough and monodisperse system, consider the position $\mathbf{r}_j(t)$ of a particle j at one time t and its next position $\mathbf{r}_j(t+\tau)$ at next time $t+\tau$ due to the random thermal motion induced by random force which is from the heat reservoir (solvent). The random displacement $\triangle\mathbf{r}_j(\tau) = \mathbf{r}_j(t+\tau) - \mathbf{r}_j(t)$ of particle j in a time τ is independent of its original position. At the observation point the scattered electric field is the superposition of that contributed by all the particles in the scattering region. Thus, at one time t the complex amplitude of the scattered light is [equations (2.2) and (2.5)]

$$E(Q,t) = \sum_j f_j \exp i[\mathbf{Q}\cdot\mathbf{r}_j(t)] \tag{2.8}$$

and at the next time $t+\tau$ the amplitude of the scattered light is

$$E(Q,t+\tau) = \sum_j f_j \exp i[\mathbf{Q}\cdot\mathbf{r}_j(t+\tau)]. \tag{2.9}$$

Eq. (2.8) and (2.9) tell us that the amplitude and phase of the total scattered electric field change with time due to the random thermal motion of the particles. In the next section we will study this motion further by forming the electric field correlation function.

2.2.2 Correlation function

Generally speaking, correlation functions provide a concise method for expressing the degree to which two dynamical or fluctuating properties are correlated over a period of time. Thus, we can understand when and how a bright speckle fades by studying the scattered electric field autocorrelation function $\langle E(t)E^*(t+\tau)\rangle$ [25]. The ensemble average is here taken in the equilibrium situation where the distribution of systems in the ensemble is independent of the absolute value of the time. Hence, this average is independent of the time t and depends only on the time difference τ. For simplicity, only dilute and monodisperse cases are considered. Using equations (2.8) and (2.9), we can write down the correlation function

$$\langle E(t)E^*(t+\tau)\rangle = \left\langle \sum_i \sum_j f_i f_j \exp i\mathbf{Q}\cdot[\mathbf{r}_j(t) - \mathbf{r}_j(t+\tau)] \right\rangle$$

When the random displacement probed by the scattering experiment is about the "wavelength" of the scattering vector, $2\pi/Q$, the correlation function can be changed significantly at that scattering angle. It means we can observe that the bright speckle becomes dark. However, if we want to obtain some quantitative information about the dynamics of particles studied, we have to deal with the ensemble-averaged correlation function. We make an assumption that the amount of the scatterers in scattering volume is large enough, however it is a dilute system, then the behaviour of the random walk performed by these scatterers is Gaussian. This ensemble average can then be

evaluated (see appendix A for details) to be

$$\left\langle \sum_i \sum_j f_i f_j \exp i\mathbf{Q} \cdot [\mathbf{r}_i(t) - \mathbf{r}_j(t+\tau)] \right\rangle = \left\langle \sum_j f_j^2 \right\rangle e^{-Q^2 \langle \Delta r(\tau)^2 \rangle / 6} \tag{2.10}$$

Note that the cross term in equation (2.10) is taken to be zero because in the case of a very dilute system there is no correlation between particles. The rest of the work is to analyse this mean-square random displacement, $\left\langle \Delta r(\tau)^2 \right\rangle$. Here we should consider the velocity of a particle which is also a fluctuating function induced by the random force mentioned above. This random displacement $\Delta \mathbf{r}_j(\tau)$ is the time integration of the velocity $\mathbf{v}_j(t)$ of the particle, that is,

$$\Delta \mathbf{r}_j(\tau) = \int_0^\tau dt \mathbf{v}_j(t) \tag{2.11}$$

In appendix B we show that the mean square displacement is related to the velocity autocorrelation function:

$$\left\langle \Delta r^2(\tau) \right\rangle = 2\tau \int_0^\infty dt \, \langle v(0)v(t) \rangle \tag{2.12}$$

In order to evaluate velocity autocorrelation function we need to understand the motion of colloidal particles which can be described by Langevin equation [21][22][24].

2.2.3 Langevin equation

The fact that small particles of about a micron perpetually move about in a random manner was first observed by Brown, a botanist, in the last century. The phenomenon is therefore called "Brownian motion". It was explained theoretically by Einstein in 1905 on the basis of the intrinsic thermal fluctuations resulting from the interaction of the small particle with the heat bath, i.e., from the random collisions of the particle with the molecules of the liquid. This phenomenon reveals very clearly the statistical fluctuations which occur in a system in thermal equilibrium.

In order to describe the motion of a colloidal particle, Newton's second law of motion is still applicable by considering the interaction of colloidal particle with the molecules of the suspension medium [24]. Its equation of motion can then be written in the form

$$m\frac{dv}{dt} = f(t) + F(t) \tag{2.13}$$

where $f(t)$ is the external force, $F(t)$ the fluctuating force from the interaction of a colloidal particle with the molecules of the suspension medium. Indeed, the interaction with the environment expressed by $F(t)$ must be such that it always tends to restore the particle to the equilibrium situation. Thus, the interaction force $F(t)$ can be written as

$$F(t) = \bar{F}(t) + F'(t) \tag{2.14}$$

where $\bar{F}(t)$, a slowly varying part, tends to restore the particle to equilibrium, and $F'(t)$, the rapidly fluctuating part of F is due to the random collisions of the particle with the molecules of the liquid. The slowly varying part $\bar{F}$ is a function of v. If v is not too large, $\bar{F}$ is linear in v. Thus, $\bar{F}$ must have the general form

$$\bar{F} = -\xi v \tag{2.15}$$

where ξ is the friction constant. Eq.(2.13) can then be written

$$m\frac{dv}{dt} = f(t) - \xi v + F'(t) \tag{2.16}$$

which is called "Langevin equation". In the absence of external forces eq. (2.16) becomes

$$m\frac{dv}{dt} = -\xi v + F'(t) \tag{2.17}$$

which can adequately describe the Brownian motion of a particle and illustrate how it can be applied to the calculation of quantities of physical interest [24].

The functional form of $v_j(t)$ can then be decided through Langevin equation. Langevin equation, a linear first order equation, can be solved formally to give

$$v(t) = v(0)\exp\left[-\left(\frac{\xi}{m}\right)\right] + \int_0^t dt' \exp\left[-\left(\frac{\xi}{m}\right)(t-t')F'(t')\right] \tag{2.18}$$

Therefore, $\langle v_j(t)v_j(t+\tau)\rangle$ can be evaluated (refer to appendix B). Equation (2.18) is then used to calculate (2.12) and the result is

$$\left\langle \triangle r^2 \right\rangle = 2\tau \times \frac{3kT}{\xi} = \frac{6kT}{\xi}\tau$$

where $\langle v^2(0)\rangle = 3kT/M$ from the energy equipartition theorem (see appendix B), kT is the thermal energy, η the solvent viscosity, R the radius of the particle. Here we ignore the second term of right-hand side of (2.18) because the random force $F'(t')$ is uncorrelated with the initial velocity $v(0)$. Consider Stokes' law [24] $\xi = 6\pi\eta R$, where η is the viscosity of solvent, R the radius of the particle, the coefficient $\frac{kT}{6\pi\eta R}$ then defines the diffusion coefficient D. This is the so-called Stokes-Einstein relation:

$$D = \frac{kT}{6\pi\eta R}. \tag{2.19}$$

Finally, the normalised scattered electric field correlation function is a single exponential form, that is,

$$\frac{\langle E(Q,0)E^*(Q,\tau)\rangle}{\langle I(Q)\rangle} = \exp(-Q^2D\tau). \tag{2.20}$$

If we can measure the decay rate of this correlation function, the diffusion coefficient then can be obtained. The method of measuring the decay rate will be presented in the next section.

2.3 Materials and methods

2.3.1 Data collection and analysis

In a dynamic light scattering (DLS) experiment, the intensity correlation function can be formed by sampling the signal through a correlator for set periods T which is the sample time. In a DLS experiment, the measured quantity is the scattered electric field correlation function [20].

Consider a scattering from a volume V containing N particles. The complex amplitude $E(Q,t)$ of the field scattered by the N particles is [equation (2.8)]

$$E(Q,t) = \sum_{i=1}^{N} f_i \exp i[\mathbf{Q} \cdot \mathbf{r}_i(t)] \tag{2.21}$$

where f_i is the field amplitude, $\mathbf{r}_i(t)$ the position of the center of particle i at time t. The average scattered intensity is thus

$$\langle I(Q,t)\rangle \equiv \left\langle |E(Q,t)|^2 \right\rangle = \left\langle \sum_i \sum_j f_i f_j \exp i\mathbf{Q} \cdot [\mathbf{r}_i(t) - \mathbf{r}_j(t)] \right\rangle \tag{2.22}$$

For large N, dynamic light scattering provides an experimental estimate of $g^{(1)}(Q,\tau)$, the normalised autocorrelation function of the field amplitude [1][20]:

$$g^{(1)}(Q,\tau) = \frac{\langle E(Q,t)E^*(Q,t+\tau)\rangle}{\left\langle |E(Q,t)|^2 \right\rangle} = \frac{F^M(Q,\tau)}{S^M(Q)} \tag{2.23}$$

Here, the measured dynamic structure factor (or intermediate scattering function) $F^M(Q,\tau)$ is given by

$$F^M(Q,\tau) = \left[N\overline{f^2}\right]^{-1} \left\langle \sum_i \sum_j f_i f_j \exp i\mathbf{Q} \cdot [\mathbf{r}_i(0) - \mathbf{r}_j(\tau)] \right\rangle \tag{2.24}$$

where $N\overline{f^2} = \langle \sum_i f_i^2 \rangle$ is to normalise $F^M(Q,\tau)$. The measured static structure factor $S^M(Q)$ is simply

$$S^M(Q) = F^M(Q,0). \tag{2.25}$$

In a dilute enough suspension there is no correlation between particles and interparticle interaction can be ignored [1], hence $S^M(Q) = 1$ (See chapter 3 for further discussions.). We can write

$$g^{(1)}(\tau) = F^M(Q,\tau) \tag{2.26}$$

If a monodisperse case is also considered, the field autocorrelation function $g^{(1)}(\tau)$ will be a form of single exponential, as discussed in section 2.2.2. The decay rate at certain scattering angle quantitatively indicates the diffusion coefficient D. For a set of known parameters η, T, and D obtained in a DLS experiment we can calculate R by using the Stokes-Einstein relation [22] $D = kT/6\pi\eta R$. In practice, monodisperse system is not an ordinary case. For polydisperse solutions, eq. (2.20) must be generalised to a sum of exponentials by reference to eq. (2.23) and (2.24):

$$g^{(1)}(\tau) = \frac{\left\langle \sum_{j=1}^{N} {f_j}^2 \exp i\left[D_j Q^2 \tau\right] \right\rangle}{\left\langle \sum_{j=1}^{N} f_j^2 \right\rangle} \tag{2.27}$$

in the case of a very dilute system. Therefore, we have to find a way to analyse this complicated result. Here we will refer to the statistical cumulant generating function that can be applied to a DLS experiment which yields a sum or distribution of exponentials.

2.3.2 The method of cumulants

We can set $\Gamma = Q^2 D$ which is the decay rate of the correlation function, and assume there exists a continuous distribution $G(\Gamma)$ in eq. (2.27) [20]. Then eq. (2.27) can be

rewritten to give

$$g^{(1)}(\tau) = \int_0^\infty G(\Gamma)\exp(-\Gamma\tau)d\Gamma. \tag{2.28}$$

With a simple fit of the experimental estimates of $\ln g^{(1)}(\tau)$ to a polynomial (ln is the natural log), we can characterise $G(\Gamma)$ with a calculation of its moments or cumulants [26]. Its moment generating function is

$$\mathsf{M}(-\tau;\Gamma) \equiv \langle\exp(-\Gamma\tau)\rangle_{Av} = g^{(1)}(\tau). \tag{2.29}$$

Here $\langle\exp(-\Gamma\tau)\rangle_{Av}$ represents an average over Γ, weighted by the distribution $G(\Gamma)$. The moments of the distribution are related to the derivatives of $\mathsf{M}(-\tau;\Gamma)$ with respect to $(-\tau)$. Similarly, we can define the cumulant generating function as the natural logarithm of the moment generating function:

$$\mathsf{K}(-\tau;\Gamma) \equiv \ln\mathsf{M}(-\tau;\Gamma) = \ln g^{(1)}(\tau). \tag{2.30}$$

The mth cumulant of Γ, $\kappa_m(\Gamma)$, is the coefficient in the expansion of $\mathsf{K}(-\tau;\Gamma)$, which takes the form of a power series in τ. In a DLS experiment the ALV-5000 software can fit experimental data to a polynomial in powers of τ:

$$\ln g^{(1)}(\tau) = -\kappa_1\tau + \kappa_2\frac{1}{2!}\tau^2 + \kappa_3\frac{(-1)}{3!}\tau^3 + \kappa_4\frac{1}{4!}\tau^4 + \ldots \tag{2.31}$$

These cumulants, which can be obtained directly in a DLS experiment, are the data we have to record. Normally, the first and the second cumulants are more important (see section 2.3.4). However, to analyse these data, it is required to explain the meaning of the cumulants obtained in a DLS experiment (see section 2.3.4 for further discussions).

2.3.3 Form factor in the RGD approximation

In a light scattering experiment we demand the sample studied be approximately index matched (it means the particles suspended in a medium whose refractive index is chosen to nearly match that of particles) so as to satisfy the RGD criterion. Therefore the scattered light is Rayleigh scattering. We can theoretically predict the behaviour of the scattered light in order to analyse and interpret the experimental results.

For a Rayleigh scattering, equation (2.22), (2.24), and (2.25) can lead to

$$\langle I(Q)\rangle = \sum_{i=1}^{N} f_i^2(Q) S^M(Q) \tag{2.32}$$

where $S^M(Q)$ is the measured static structure factor discussed in section 2.3.1. Precisely, a polydisperse system can be characterised as a continuously normalised distribution of particle radius, $G(R)$. As mentioned in section 2.3.1, for a very dilute system $S^M(Q) = 1$. Thus the scattered light intensity can be sufficiently described by form factor [18][19] [refer to eq. (2.7)]:

$$I(Q) \propto \sum_{i=1}^{N} [f_i(Q)]^2 = \int_0^\infty R^6 P(QR) G(R) dR \tag{2.33}$$

Figure 2.2 illustrates the scattered light intensity by adopting Schulz particle size distribution (see appendix C.). The reduction of scattered light intensity is due to the destructive interference of the scattered light by the scattering elements of the particle. When $Q\bar{R}$ is about 4.49, form factor goes to its first minimum. Accordingly, the bigger the particle, the smaller the scattering vector Q, that is, the earlier the first minimum of its form factor appears. This phenomenon implies the possibility of characterising a polydisperse system by the DLS experiment [18]. The experimentally measured scattered light intensity can be obtained by the use of static light scattering presented in the next chapter. We worked out the theory so as to find out the feature of single

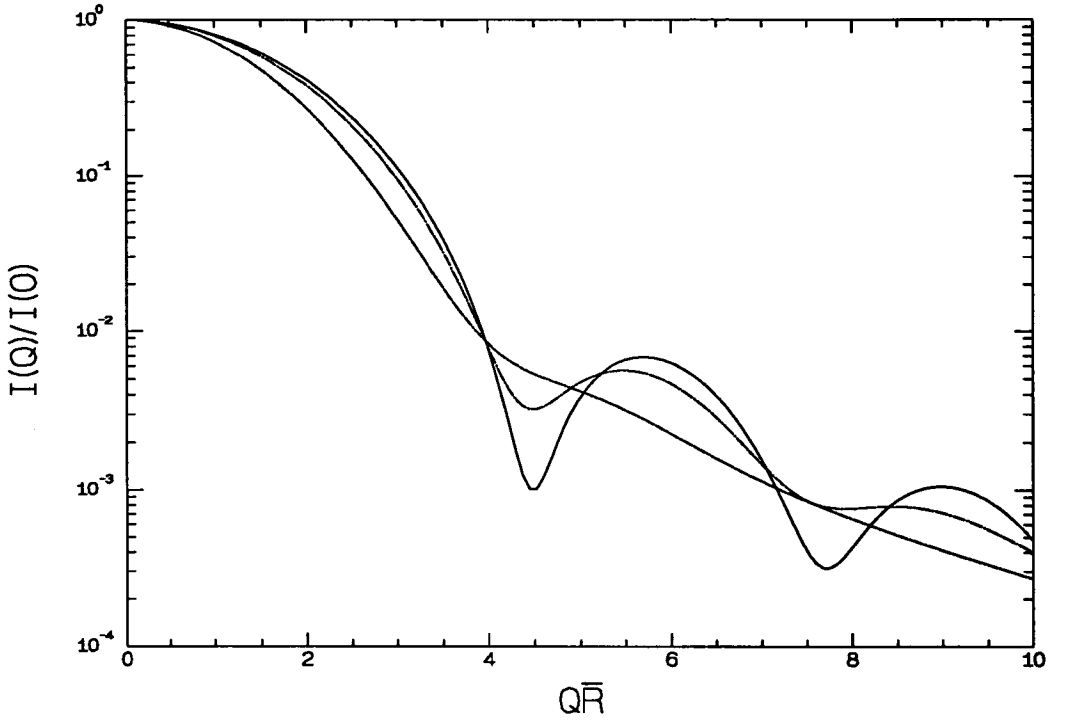

Figure 2.2. The scattered light intensity distorted by polydispersity σ is characterised by selecting Schulz particle size distribution $G(R)$ to calculate eq. (2.33). Solid line is for $\sigma = 0.05$, dash-dot line for $\sigma = 0.10$, short dashed line for $\sigma = 0.20$. $\overline{R}$ is the mean radius.

particle form factor. As a result, we make an attempt to establish a model to analyse the measured quantity, diffusion coefficient.

2.3.4 Effective diffusion coefficient

In section 2.3.2 we have presented the measured quantity, κ_1, in a DLS experiment. Theoretically, if we take the first order derivative of equation (2.31) and set $\tau \to 0$, κ_1 can be obtained:

$$\kappa_1 = -\lim_{\tau \to 0} \frac{d}{d\tau} \ln g^{(1)}(\tau) \tag{2.34}$$

which is the minus of the initial slope of the logarithm of the first order correlation function (refer to figure 2.3). Here, "$\tau \to 0$" has to be seriously discussed. At first the

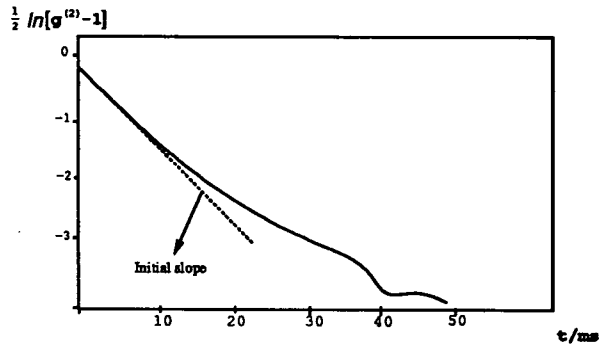

Figure 2.3. A schematic plot of the first order correlation function. Here $\frac{1}{2}\ln[g^{(2)}-1] = \ln g^{(1)}$.

time-scales of interest should be explored in detail.

The following clarification [27] will also concretely present the quantity in the practical case, $R \simeq 250nm$, $m \simeq 6 \times 10^{-17}kg$, $\eta \simeq 3.4cp$ for cis-decalin, $T = 293^oK$, $D_0 \simeq 2 \times 10^{-13}m^2/s$, and $\lambda = 647.1nm$:

•τ_B, the inertial relaxation time $\sim \frac{m}{6\pi\eta R} \sim 10^{-9}s$, can be taken as the fluctuation time of the particle velocities in response to the solvent forces.

•τ_R, is the time taken for a particle to diffuse across its own diameter $\sim \frac{R^2}{D_0} \sim 10^{-1}s$, where D_0 is free particle diffusion coefficient.

•$\tau_Q \sim \frac{1}{D_0Q^2}$, the time taken for a particle to diffuse over the wavelength of the scattering vector Q, is experimentally important.

•$\tau_\phi \sim \frac{R^2\phi^{-\frac{2}{3}}}{D_0}$ is the time taken for a particle to diffuse across a typical particle separation distance $\sim R\phi^{-\frac{1}{3}}$, where ϕ is the colloidal volume fraction.

Strictly speaking, for the calculation of the initial decay rate of equation (2.32), even though $\tau \to 0$, we still concentrate on $\tau \gg \tau_B$ microscopically because the positions of non-interacting particles in suspension change by significant fractions of their radii only in times much greater than $\tau_B(\tau \gg \tau_B)$ in which their Brownian velocities have

undergone many fluctuations and their motions are effectively diffusive [27].

In appendix C we consider the case of a polydisperse system and derive the important result, as shown below:

$$\ln g^{(1)}(\tau) = -(\bar{D}Q^2)\tau + \left(\frac{\overline{D^2} - \overline{D}^2}{2}\right) Q^4\tau^2 + ..., \tag{2.35}$$

where

$$\overline{D^n} = \frac{\int_0^\infty R^6 P(QR) D^n G(R) dR}{\int_0^\infty R^6 P(QR) G(R) dR}. \tag{2.36}$$

In section 2.3.2 we presented the work of data analysis by ALV-5000 software in a DLS experiment and described the important parameters (cumulants), as shown in eq. (2.31). Now it is possible to interpret the physical meaning of cumulants in a DLS experiment by reference to eq. (2.31) and (2.35). The first cumulant κ_1 is just the mean decay rate $\bar{\Gamma} = Q^2\bar{D}$ that we want to measure in a DLS experiment. The second cumulant, κ_2, suitably normalised by $(\kappa_1)^2$, is a good measure of the relative width of the distribution (see appendix C). Similarly, κ_3 and κ_4 are measures of the skewness or asymmetry, and the kurtosis, the peakedness or flatness of the distribution. The effective diffusion coefficient is then defined as [refer to eq. (2.34)]

$$D_e(Q) \equiv -\frac{1}{Q^2} \lim_{\tau \to 0} \frac{d}{d\tau} \ln g^{(1)}(\tau) \tag{2.37}$$

The initial slope of the logarithm of the first order correlation function is frequently used to analyse the DLS data. Some physical properties of colloidal suspensions can be disclosed by using this data analysis, such as the swing phenomenon of D against scattering vector Q discussed in section 2.3.3, and hydrodynamic factor of concentrated suspensions, not discussed here. In figure 2.4 we plot $R_e(Q)/R_e(0)$, as a function of $Q\bar{R}$. Here the apparent radius $R_e(Q)$ is defined as $kT/6\pi\eta D_e(Q)$ by reference to

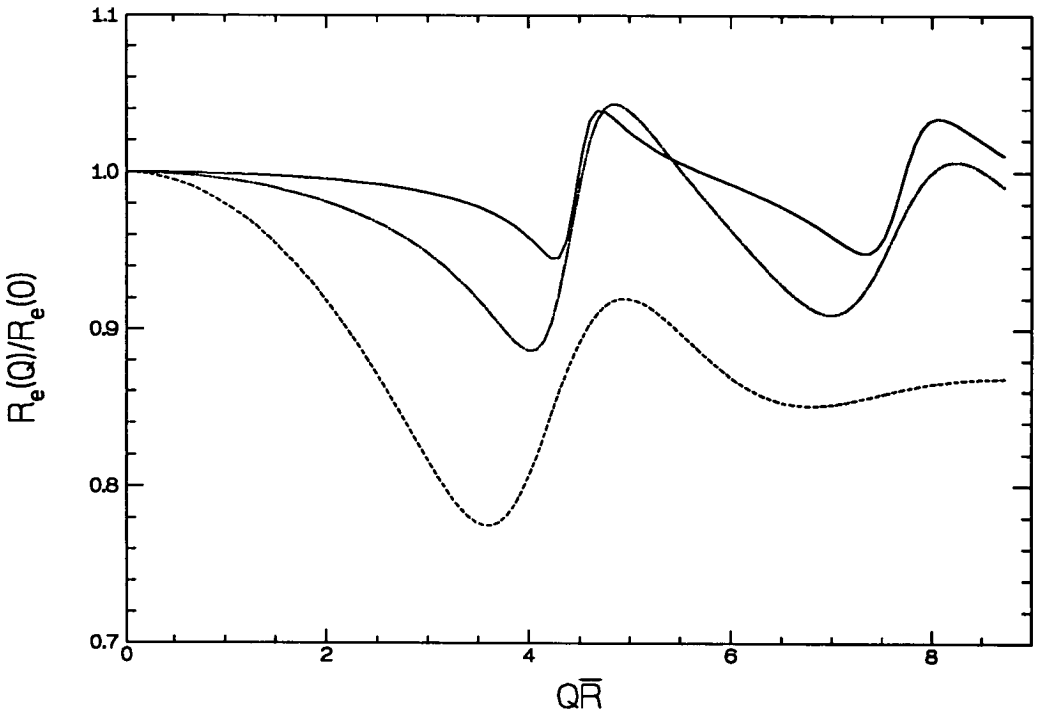

Figure 2.4. The normalised particle radius as a function of Q can be secured by choosing the Schulz particle size distribution $G(R)$ to calculate eq. (2.36) at $n = 1$ and then calculating Stokes-Einstein relation eq. (2.19). Solid line is for $\sigma = 0.05$, dash-dot line for $\sigma = 0.10$, dashed line for $\sigma = 0.20$. See reference [18] for details.

Stokes-Einstein relation [eq. (2.19)]. In reference [18] Pusey and van Megen testify that for a sample system of small polydispersity the difference between the extrema of $R_e(Q)/R_e(0)$ at the first intensity minimum shown in figure 2.2 and 2.4 is about 2σ. This provides a very simple way to approximately estimate the polydispersity if the polydispersity of the sample system is not high ($\lesssim 10\%$). If the polydispersity of a sample system is considerably high , say $> 10\%$, this method will underestimate the predicted value by theory [18]. As described in section 2.3.3, the scattered intensity by the big particle goes to the first minimum earlier than the small one does. Therefore, in a polydisperse system the scattered intensity by small particle will dominate when the scattered intensity by the big particle gets the first minimum, and vice versa [18]. This results in the swing phenomenon shown in figure 2.4 and provides a good way to

characterise a polydisperse system.

2.4 Experimental

2.4.1 Instrument

The equipment is shown in Figure 2.5. All the instruments were set up on a floating steel-table to avoid the effect of vibration. The light source is laser beam which is focused in the sample studied to increase the scattered light intensity. A pin hole, about $600\mu m$, was put in front of the photomultiplier tube (PMT). If necessary, a filter could be used to decrease too high intensity. Generally, the count rate can not exceed $100kHz$, or the PMT cannot work normally. The ALV-5000 multiple tau digital correlator was adopted to deal with received signal by particles. Between PMT and correlator is the pulse amplifier-discriminator (PAD). The further detail about the physical principles involved in this laser fluctuation spectroscopy is available in reference [28]. The water in

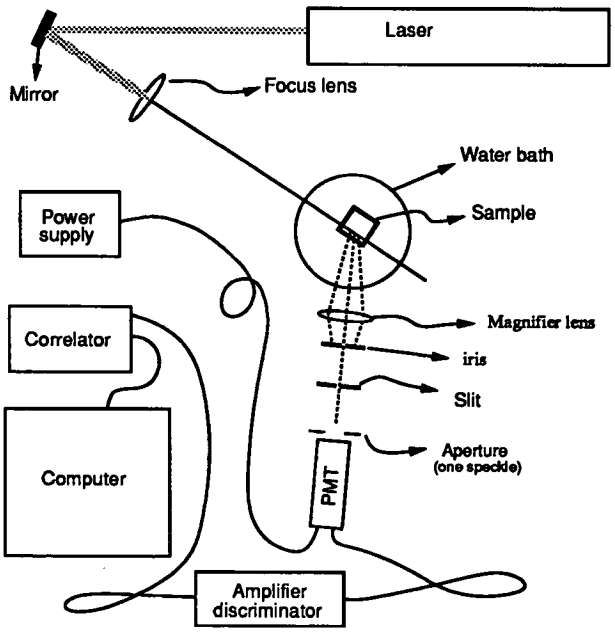

Figure 2.5. The block diagram of DLS equipment

the bath was filtered by circulating it through a filter to decrease the unusual scattered light by dust in water.

2.4.2 Procedures and conditions

The measurements were made on the next day after shaking the sample to allow the dust in sample cell to settle first. The light source was a krypton ion laser operated on wavelength $\lambda = 647.1nm$ or argon laser operated on $\lambda = 514.5nm$. Sample cell has to be tilted in the water bath to deviate reflected light from the rear window of sample cell.

Scattering was observed at angles $30^0 \lesssim \theta \lesssim 145^0$ through the side face of a cell of square cross section contained in a water bath thermostated to about 20^0C. This can decrease the effect of multiple scattering especially around the first minimum of scattered light intensity. Combining these scattering angles and laser wavelength provided a reasonably wide range of scattering vector. The logarithm of this correlation function was fitted by ALV-5000 software to a quadratic function of correlation delay time. The coefficients of this fit provided the first, second, and third cumulants, κ_1, κ_2 and κ_3.

2.4.3 Sizing particle

The main object of this simple experiment is to check the technique of sizing particle by DLS. In this DLS experiment, the sample cell is made out of a rectangular glass tube. The colloidal particles are colloidal polystyrene (system 1) and PMMA (system 2). For system 1, a dilute suspension of polystyrene, in distilled water, can be approximated as hard spheres. At each angle one made 3 measurements of duration 120 seconds. This set of data procured by analysing the initial slope of the logarithm of the first order correlation function, first cumulant, and then using equation (2.19) and (2.37) to calculate $R_e(Q)$ shows essentially no angular dependence. The plot of the apparent radius is shown in Figure 2.6. The average radius is $44 \pm 1nm$.

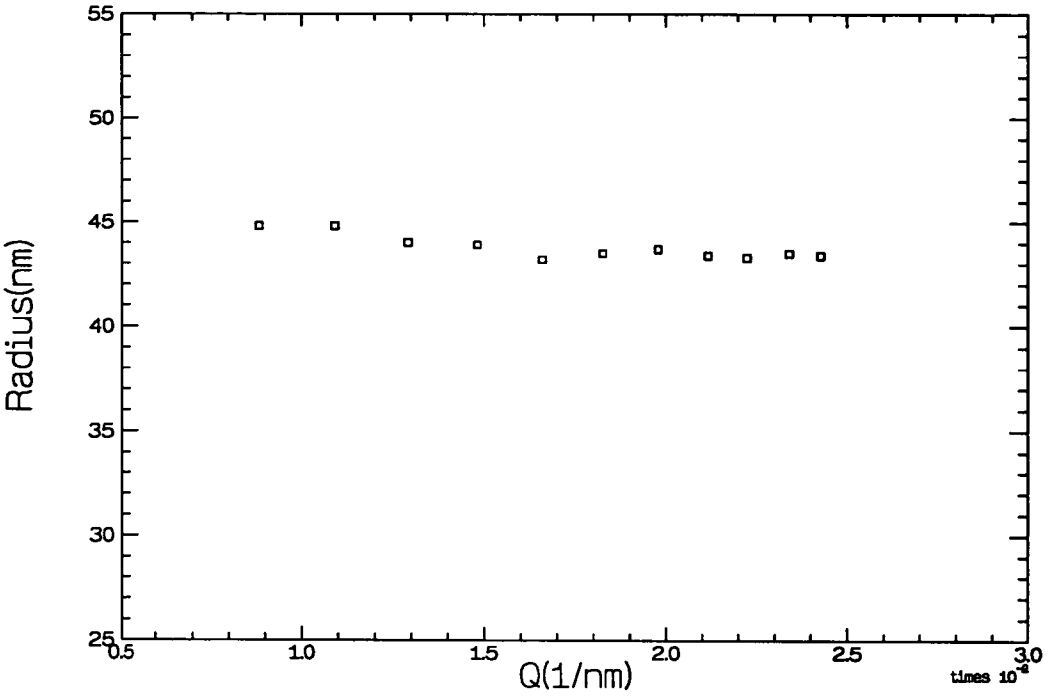

Figure 2.6. Data for polystyrene latex spheres of apparent radius as a function of scattering vector Q. The average radius is $44 \pm 1nm$.

Obviously, the plot of apparent radius of polystyrene latex sphere shows no angular dependence. To explain this result, we have to refer to single particle form factor indicated in section 2.3.3. Only around the minimum of scattered light intensity where $Q\bar{R} \simeq 4.49$ shown in figure 2.2 the determination of calculating polydispersity by DLS is applicable. This implies that this approach (DLS techniques) cannot determine the polydispersity if the reduction of the scattered light by particles is beyond the range of the detection angle of a DLS measurement. By checking the highest angle we can go in this DLS experiment and calculating the product of $Q_{max}\bar{R} \simeq 1$ which is much smaller than 4.49, we conclude that the "flat" result in figure 2.6 is reasonable by reference to the early part of figure 2.4. Here, Q_{max} is associated with the highest scattering angle we can go in this experiment.

2.4.4 Polydisperse system

Owing to the success of the technique of sizing small, relatively monodisperse particles by DLS, the next stage is to attempt to characterise a polydisperse system. For system 2, there are two dilute samples of different polydispersity. One (Lot NO. DMM7) has polydispersity of around 3-5%, the other (Lot No. SP) around 35%. The suspension medium is cis-decalin. The difference of refractive index between the water in bath and the solvent in sample cell has to be considered because the square sample cell was used in a DLS experiment. Consequently, the "scattering angle" has to be corrected for refraction. t each angle we made 5 measurements of duration 200 sec. Data for DMM7 of the apparent radius as a function of scattering vector Q are shown in figure 2.7. The

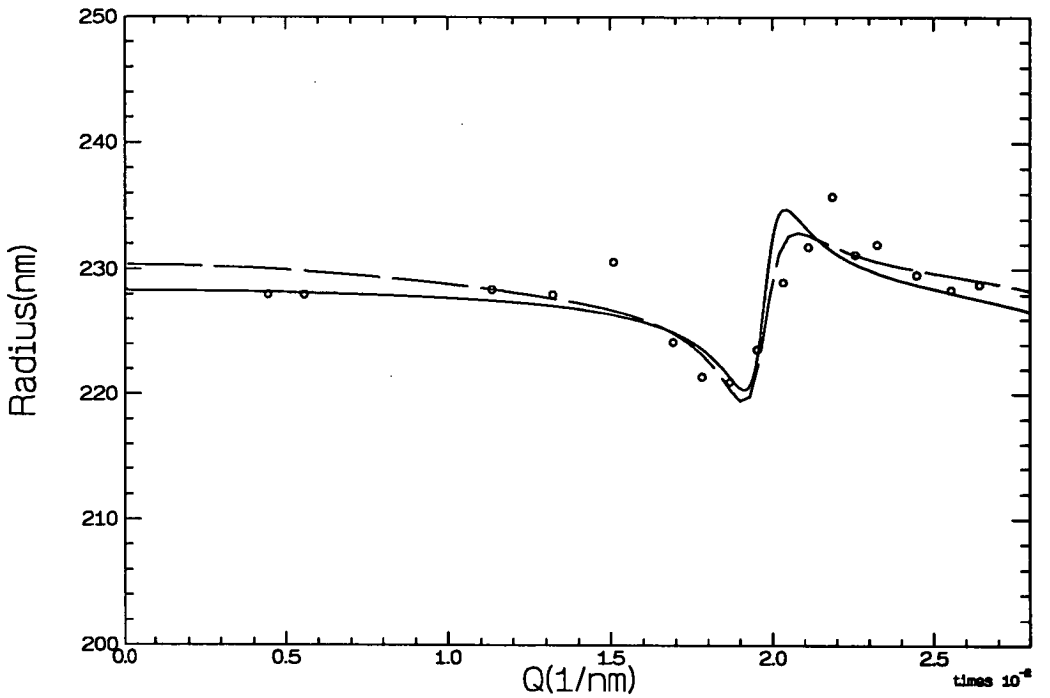

Figure 2.7. Data for DMM7 of the apparent radius as a function of scattering vector Q, o: measured data point, solid line is the fitting curve by selecting Schulz distribution with $\bar{R} = 227.11nm$, $\sigma \simeq 0.030$ to calculate eq (2.36) and (2.19), dashed line is the fitting curve by selecting the size distribution modelled by delta functions with $\bar{R} = 227.79nm$, $\sigma \simeq 0.045$, skewness $\simeq 0.38$.

method of data analysis is evaluated by fitting it to a "model". The parameters of this model come from the theory developed by Pusey and van Megen [18]. Here two approaches are compared. One is to use Schulz particle size distribution (see appendix C) to characterise the sample system. We use eq. (2.36) and set $n = 1$, and then select Schulz particle size distribution to evaluate eq. (2.36). The final form, which can be found in reference [18], is adopted in the least square minimisation fitting program. The other is a distribution modelled by a set of delta functions (a simulation for multi-component mixture of particles). We can use a p-component system (p delta functions) to model a distribution [$G(R_i)$ where $i = 1, ..., p$] to replace Schulz distribution so as to simplify the calculation of eq. (2.36). These two approaches used in the least square minimisation fitting program are considerably consistent with each other. The only difference comes from the skewness (see appendix C) of particle size distribution.

The results shown in figure 2.7 and 2.8 are quite comprehensible by calculating the product of Q_s at which the swing happens and $\bar{R}$, the mean radius of the particles. For DMM7, $Q_s\bar{R} \simeq 4.5$, and for SP, $Q_s\bar{R} \simeq 4.2$. Again, around this region when light scattered by the big particle goes to minimum, the light scattered by the small particle dominates. Accordingly, at that angle in the DLS experiment the received signal will only reflect small particle diffusion. The experimental results are very consistent with theoretical prediction discussed in section 2.3.4. If we make a rough measurement that $[R_e(Q)_{max} - R_e(Q)_{min}]/\bar{R} \simeq \frac{15}{227} = 0.066 = 2\sigma$, then the polydispersity can be estimated to be about 0.033 which is between 0.030 obtained from delta function model and 0.045 from Schulz distribution model. This supports Pusey and van Megen's argument (refer to section 2.3.4 and [18]).

Data for SP are more complicated due to the broad distribution and skewness. Obviously, the model of Schulz distribution can not be used to analyse the data owing to considerably non-symmetric shape of particle size distribution. Figure 2.8 illustrates

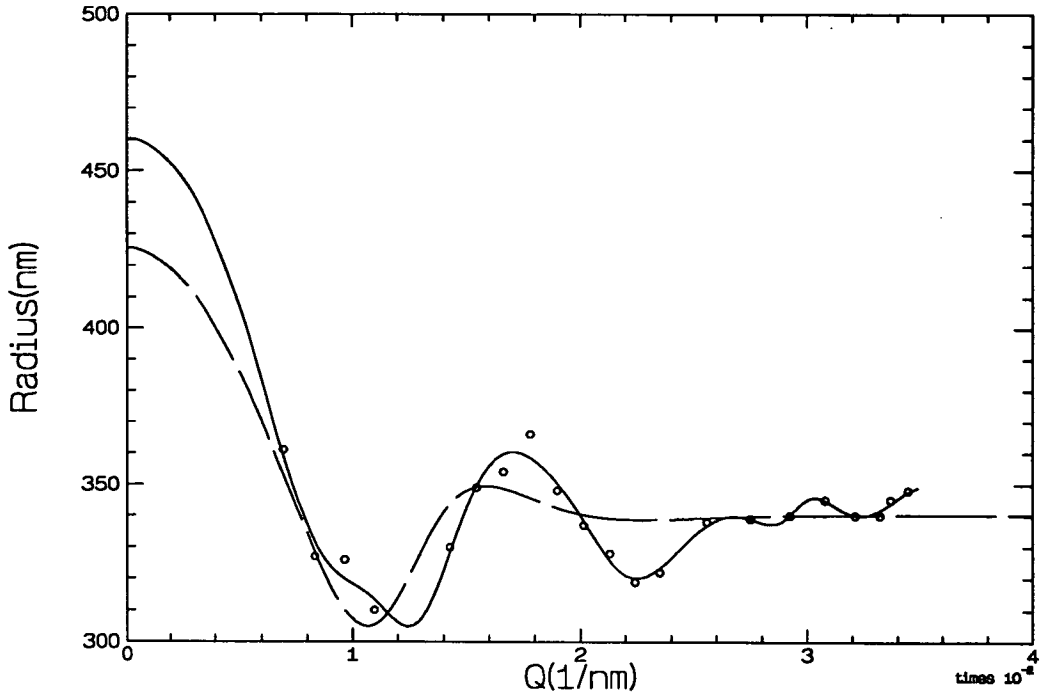

Figure 2.8. Data for SP of apparent radius as a function of scattering vector Q, measured at $\lambda = 647.1nm$, solid line is the fitting curve by selecting a distribution modelled by a set of delta functions with $\bar{R} = 303.18nm$, $\sigma \simeq 0.358$, skewness $\simeq 0.34$, dashed line is the fitting curve by selecting Schulz distribution which is obviously poor in dealing with such broad and skew particle size distribution.

this fact. It also shows that the results obtained from delta function approach still work very well. Note that at high Q the small variation shown in figure 2.8 probably is due to the effect of multiple scattering and the data in that region is not reliable. However, if only considering the big swing at the first intensity minimum, one can definitely say that the polydispersity of sample SP is higher than 0.20 by reference to figure 2.5.

Here we have presented the method of characterising samples. The goal is to develop an approach to objectively and effectively measure the polydispersity of the sample system studied. If the model of particle size distribution can characterise the polydisperse system well, then it is possible to design an experiment to fractionate a polydisperse system [29].

2.4.5 An attempt of fractionating a polydisperse system

The idea of fractionation of polydisperse colloids by polymer induced crystallisation comes from the understanding of the phase behaviour of colloid plus polymer mixtures. The experimental and theoretical work of colloid-polymer mixtures have been comprehensively studied [30-35]. An attempt was made to fractionate sample SP whose polydispersity is estimated to be about 35% (See section 2.4.4.). A stock solution of random coil polystyrene molecules whose mean gyration radius is $18nm$ was prepared. By reference to the phase diagram of colloid plus polymer mixtures [34], we found the fluid-solid phase boundary is very sensitive to the ratio by radius of polymer to colloid. In chapter 1 we described the phase diagram of a pure hard-sphere colloidal system, showing $\phi_f = 0.494$ and $\phi_m = 0.545$ (refer to figure 1.4). If random-coil polystyrene molecules are added in the pure system, then ϕ_f will get smaller and ϕ_m greater as the polymer concentration increases. Inspection of the phase diagram (polymer concentration against colloid volume fraction) of the mixture system shows the phase boundary; between the left and the right wings is the coexistence of fluid and solid [30-35]. If the mean gyration radius of polymer is kept equal, then in the phase diagram the boundary will drop down as the radius of the colloid increases. We estimated the mean radius of sample SP, found to be about $300nm$ through the previous experiment. We, therefore, added a little amount of polymer solution to sample SP to give a polymer concentration (cp) about $0.004g\text{-}cm^{-3}$, and observed the phenomenon of phase separation 3 days later. Then, we moved the fluid phase to the other cell, fluid phase labelled SP-L and solid phase labelled SP-O. Afterwards, the two samples were "washed" 3 times by centrifuging the particles in cells down, removing the supernatant, and then adding cis-decalin to remove polymer. The same procedures were then applied to samples SP-L and SP-O. Note that the colloid volume fraction of pure colloid stock solutions was controlled to be about 0.16 in this experiment. After two steps of fractionation, a set of different average particle sizes were definitely obtained. Unfortunately, the

particle size distribution is still very broad [36]. Although Bibette declared the success of purification for polydisperse emulsions [29], to our knowledge, the fractionation of polydisperse sterically-stabilised colloids is not proved to be successful yet.

In section 2.1 we described the effect of polydispersity on the phase transition of colloidal particles. There is no doubt that investigating monodisperse suspensions can reduce the discrepancy between colloidal particles and simple atomic materials. Therefore, for the future plan, it is really worth attempting to design a fractionation experiment for polydisperse dispersions.

2.5 Discussion

The technique of sizing particle by a DLS experiment is proved to be successful. Although there are some limitations for the DLS experiment to detect the polydispersity of the sample system studied, such as multiple scattering, this technique is still very practical. As mentioned in section 2.3.4, particle diffusion, a very important topic, can be studied via the use of a DLS experiment. To improve the performance of a dynamic light scattering equipment, the new-developed two colour dynamic light scattering instrument is in test. The latest test by Segrè *et al.* [37] verified that multiple scattering does not affect the measurement of two colour dynamic light scattering.

As for the fractionation experiment, there are some difficulties in making samples, such as the determination of colloid volume fraction. We can not precisely estimate the concentration of a pure colloid system due to polydispersity. If the polydispersity of the sample system is higher than 10% [17], crystallisation can not be observed. As a result, our samples can not be calibrated. We estimated that the second decimal place of colloid volume fraction is not reliable in the fractionation experiment. In addition, it should be emphasised that the effect of gravitational settling of very polydisperse suspensions makes the measurement difficult. Therefore, it might be helpful to investigate

the sedimentation of colloidal particles in a polydisperse system first.

At high Q multiple scattering, which always makes the DLS results complicated, will distort the scattered light. Similarly, around the minimum of form factor the measured hydrodynamic radius is not very reliable. Therefore, it is necessary to make sure that the sample studied is extremely dilute and to reduce the effect of multiple scattering as much as possible. For the future study, two colour dynamic laser light scattering instrument could be used to check the polydispersity of the sample obtained from the fractionation experiment so as to reduce the experimental difficulties, for example, multiple scattering.

Chapter 3

Static light scattering

3.1 Introduction

Static laser light scattering permits an accurate description of the average spatial distribution of colloidal particles suspended in organic solvent. Since the wavelength of the visible laser beam is comparable with the interparticle spacing of colloidal systems, the study of the structure factor of colloids can be experimentally achieved by the use of static laser light scattering.

As mentioned in chapter 1, the ultimately small size and short relaxation time prevent the experimental study of kinetics and mechanism of crystallisation for atomic systems. Colloidal crystals offer an alternative approach for studying the kinetics of the freezing transition. During a disorder-order transition the pressure and temperature of the colloidal system do not change. However, there is a change of entropy. As a result, the latent heat L released from colloidal fluid is absorbed by suspension medium. The latent heat is defined as the heat transferred during a phase transition, that is, $L \equiv T(S^{(f)} - S^{(i)})$ [38]. (The different phases are indicated by superscripts) Williams *et al.* have estimated the latent heat released in the colloidal fluid-solid transition by investigating the melting of crystalline suspensions of charged polystyrene spheres [39].

The result implies that the colloidal crystallisation transition is practically isothermal because the suspension medium acts as a huge heat bath. Therefore, the study of kinetics and mechanism of crystallisation by using the model of colloidal suspensions avoids some experimental difficulties occurring in atomic systems [40], such as the change of the crystal growth features due to the latent heat.

In this chapter the structure of colloidal suspensions is investigated, such as concentrated colloidal fluid and colloidal crystals. Experimental results are presented here in detail, theoretical conjectures are discussed as well. Generally speaking, the theoretical work becomes arduous when the sample system goes into the high concentrated realm.

3.2 Theory

3.2.1 The determination of structure by light scattering

Colloidal suspensions which we study consist of a very large number of hard-sphere particles whose positions cannot be determined at any given moment. Experimentally, what is measured is average scattered intensity. This provides some information about the statistical distribution of particles in the sample studied. In the case of a very dilute sample, as discussed in chapter 2, there is no correlation between particles. It reflects that particles' positions are completely random and independent. At higher suspension concentrations, a particle will be caged by its neighbours in a local volume due to "excluded-volume" effect. Therefore, short-ranged positional correlations appear. However, the long-range disorder still corresponds to the fact that there does not exist long-ranged positional correlations because the "caging effect" becomes insignificant when we concentrate on the contribution by the other distant particles. As for crystals, all the particle positions are regular, and not only short-range but also long-range order appear.

In chapter 2, equation (2.22), the average scattered intensity by particles is presented.

To find out the structure of colloidal suspensions by studying the average scattered intensity, the formation of scattered intensity has to be determined. The particle's positional correlation term is implied in the measured static structure factor $S^M(Q)$ defined in chapter 2. As discussed above, in infinitely dilute case, there are no positional correlations of particles and $S^M(Q) = 1$. Here we will start from statistical standpoint to reveal the physics of the structure factor [41].

Consider a particle situated at the origin O which is at the centre of a group of particles. The question is how to find a way to determine the structures for samples of different concentration. Here we define a probability $p(\mathbf{r})$ of finding the centre of a second particle in the small volume δv situated at the end of the vector $\mathbf{r}$ whose origin is at O. Assume in a large volume V there are N particles. We define an average volume shared by one particle, that is, $v = \frac{V}{N}$. If the particle distribution of the system is completely random and independent, $p(\mathbf{r}) = \frac{\delta v}{v} = p_o$ is constant and reflects that particles can freely move to everywhere without any difficulty like ideal gases. This is the case of an extremely dilute colloidal system. Note that the average number density is defined as $\rho_o = \frac{N}{V}$. Thus, $p_o = \rho_o \delta v$ and $\sum_{\delta v} p_o = 1$ or $\int_v \rho_o dv = 1$.

At higher concentrations, the positional correlations between particles due to the "caging effect" have to be considered. Therefore, $p(\mathbf{r})$ is not simply $\frac{\delta v}{v}$. It means the particle distribution is disordered but their positions are correlated, that is, the particle moves with difficulty due to its neighbours' caging. We also attempt this expression:

$$p(\mathbf{r}) = g(\mathbf{r}) p_o \tag{3.1}$$

where a radial distribution function, $g(\mathbf{r})$, is introduced to deal with the positional correlation phenomenon [42]. The more familiar expression is

$$\rho(\mathbf{r}) = g(\mathbf{r})\rho_o \tag{3.2}$$

which is physically identical to eq. (3.1). $g(\mathbf{r})$ defines the statistical configuration of the particles. In addition, $4\pi r^2 dr g(r)\rho_o$ gives the number of particles whose central positions can be found in the shell, $4\pi r^2 dr$, if the system is homogeneous and isotropic. Let us consider the case that the particles are ordered in space as in a perfect crystal. $g(\mathbf{r})$ is zero for all points in space except when $\mathbf{r}$ is one of the vectors of the crystal lattice. The periodicity is very obvious. If the particle distribution is random, $g(r)$ is more complicated. At least we can say that $g(r) = 0$ for $r < 2R$, where R is the radius of the particle under the consideration of the impenetrable hard sphere case. We also expect that even at high concentrations the "caging effect" only can cover a few particle diameters. Far exceeding this region there will be no positional correlations between particles. Then, in a large scale of the distance between two particles the condition is similar to the one of dilute case. Briefly speaking, $g(r)$ goes towards 1 for $r \gg 2R$. This expresses the structure of liquids that each particle establishes a partially ordered arrangement of its neighbours and a liquid possesses no long-range order as a crystal does.

Now let us concentrate on the average scattered intensity from a homogeneous and isotropic system:

$$\langle I \rangle = \left\langle \sum_i \sum_j f_i f_j \exp i\mathbf{Q} \cdot \mathbf{r}_{ij} \right\rangle$$

where $\mathbf{r}_{ij} = \mathbf{r}_i - \mathbf{r}_j$. Consider the simplest case that all the particles studied are identical, then

$$\langle I \rangle = f^2 \left\langle \sum_i \sum_j \exp i\mathbf{Q} \cdot \mathbf{r}_{ij} \right\rangle = Nf^2 \left[1 + \frac{1}{N} \left\langle \sum_{i \neq j} \exp i\mathbf{Q} \cdot \mathbf{r}_{ij} \right\rangle \right] \tag{3.3}$$

The sum in square bracket in eq. (3.3) indicates interparticle interference. As mentioned above, because $\rho(r)$ is the distribution of particles at distance r from a reference particle, equation (3.3) can be written as [42]

$$\langle I \rangle = Nf^2 \left[1 + \int_0^\infty dr 4\pi r^2 \rho(r) \exp i\mathbf{Q} \cdot \mathbf{r} \right] \tag{3.4}$$

under the assumption of a very large scattering volume. As for an extremely dilute case, $\rho(r) = \rho_0$, and then the integration in equation (3.4) is a delta function $\delta(Q)$ which corresponds to the scattering from a uniform concentration system. This is the contribution by the forward scattering [42] that we normally exclude, and rewrite equation (3.4) as

$$\langle I \rangle = Nf^2 \left[1 + \rho_0 \int_0^\infty dr 4\pi r^2 [g(r) - 1] \exp i\mathbf{Q} \cdot \mathbf{r} \right] \tag{3.5}$$

By comparison with equation (2.32) we can find

$$S(Q) = 1 + \rho_0 \int_0^\infty dr 4\pi r^2 [g(r) - 1] \exp i\mathbf{Q} \cdot \mathbf{r} \tag{3.6}$$

Hence the static structure factor can be obtained by a light scattering experiment. Afterwards, $g(r)$ can be in principle derived via a spatial Fourier transform.

3.2.2 The measured static structure factor $S^M(Q)$

In theory, it is impossible to measure $S(Q)$ directly by a light scattering experiment. However, a circuitous and accurate approach is available [1] to measure $S(Q)$. The

idea stems from the infinite dilute case in which there are no positional correlations between particles and $g(r) = 1$ for $r > 2R$. If $S^M(Q)$ is unit, the average scattered intensity will simply be $N\overline{f^2}$ which is dominated by a single particle form factor (see section 2.3.3 for details). This is the quantity that has to be separated from the average intensity scattered by high concentrated suspensions to give the structure factor. Unfortunately, the numbers of particles in the scattering volume in the dilute and concentrated experiments cannot be kept equal, so that $S(Q) \propto \frac{<I_C>}{<I_D>}$. The subscript C stands for concentrated suspensions and D stands for very dilute ones. If the sample system is not monodisperse, then eq. (3.3) has to be corrected because f_i is coupled with the ith particle's position. Therefore, the result is more complicated than eq. (3.3). Rigorously speaking, in any case the measured static structure factor is defined as [1]

$$S^M(Q) \equiv \frac{\sum_{i=1}^{N_C}\sum_{j=1}^{N_C}\langle f_i(Q)f_j(Q)\exp[i\mathbf{Q}\cdot(\mathbf{r}_i-\mathbf{r}_j)]\rangle}{\sum_{i=1}^{N_D} f_i^2(Q)} \tag{3.7}$$

where N_C = the number of particles in scattering volume for "C" and N_D = the number of particles in scattering volume for "D". This definition covers polydisperse systems. The theoretical study of $S^M(Q)$ will be presented in section 3.3.1.

3.2.3 Close-packed structures

To start this section, we have to ask a question of what type of structure the colloidal particles will adopt when crystallisation begins to occur. In atomic systems, the properties of interatomic force or binding are crucial in determining the crystal structure.

As mentioned in chapter 1, the colloidal model system used here is similar to that of simple atomic matter, such as a rare gas. Actually, the type of binding of a rare gas is weak binding which is mainly caused by van der Waals force. As a result, in solid phase

rare gas atoms pack together as closely as possible. In our (nearly) hard-sphere colloidal systems the interparticle interaction is considered to be zero except at touching. In addition, it also has been known that "free-volume entropy" favours hard-sphere solid phase (See chapter 1 for details.). Qualitatively these reflect that in our sample system the nearest-neighbour effects are relatively more important and will favour the formation of a close-packed structure. Therefore it seems reasonable that the structure of a hard-sphere colloidal crystal should be close-packed.

There are a large number of ways of arranging identical spheres in a regular array that maximises the packing fraction, the maximum proportion of the available volume that can be filled with hard spheres. One is the face-centred cubic structure (fcc); another is the hexagonal close-packed structure (hcp). The fraction of the total volume occupied by the hard spheres which is $\frac{\sqrt{2}}{6}\pi \simeq 0.74$ for all possible close-packed structures can be derived from the definition: $(n \times \frac{4}{3}\pi R^3)/V_{cell}$, where n is the number of lattice points per conventional unit cell, R the radius of hard sphere, and V_{cell} the volume of conventional unit cell.

Spheres are arranged in a single closest-packed layer A by placing each sphere in contact with 6 others [43]. This layer may serve as either the basal (001) plane of an hcp structure or the (111) plane of the fcc structure. A second identical layer B may be added by placing each sphere B in contact with three spheres of the bottom layer. A third identical layer may be added in two ways. The fcc structure is obtained if the spheres of the third layer are added over the holes in the first layer that are not occupied by B. We label such a layer C. The hcp structure can be obtained when the spheres in the third layer are placed directly over the centres of the spheres in the first layer. In other words, the sequence $...ABABAB...$ gives a hcp structure, whereas $...ABCABC...$ corresponds to fcc. Figure 3.1 illustrates the relative positions of the three layers A, B, C for a close-packed structure. If we set type A to be the reference

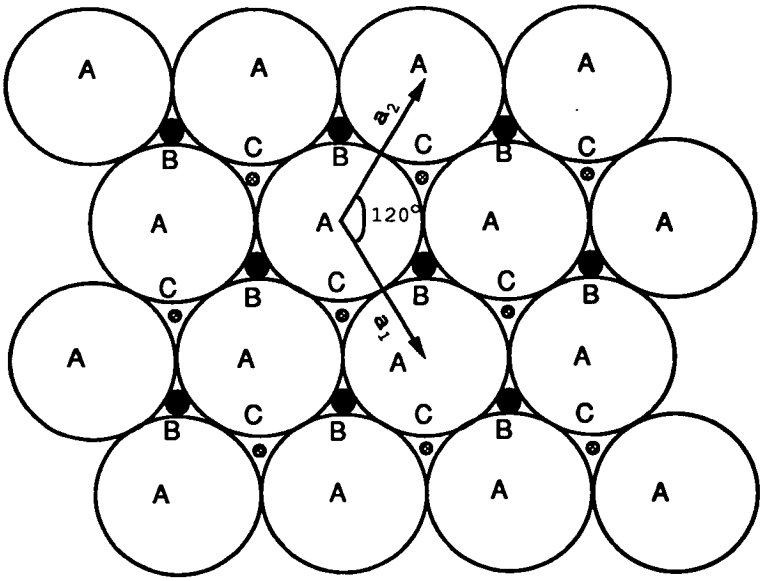

Figure 3.1. The close-packed structure of hard spheres

position, the layer of type B will displace $\frac{1}{3}(2\mathbf{a}_1 + \mathbf{a}_2)$ or $\frac{1}{3}(-\mathbf{a}_1 + \mathbf{a}_2)$ or $\frac{1}{3}(-\mathbf{a}_1 - 2\mathbf{a}_2)$ relative to A; here $\mathbf{a}_1$ and $\mathbf{a}_2$ are the lattice vectors in a hexagonal representation. However, these three possible displacements for type B are structurally identical because they cause the same change in phase angle in scattering [44] (see section 3.3.2 for discussion). Similarly, the layer of type C displaces $\frac{1}{3}(\mathbf{a}_1 + 2\mathbf{a}_2)$ or $\frac{1}{3}(\mathbf{a}_1 - \mathbf{a}_2)$ or $\frac{1}{3}(-2\mathbf{a}_1 - \mathbf{a}_2)$ relative to A. Again, they are structurally identical.

The *fcc* and *hcp* structures are made up of close-packed planes of spheres. The structures which differ in the stacking sequence of planes, *fcc* and *hcp*, are known as random stacking.

As discussed in section 1.5, for hard sphere cases, the "free volume entropy" plays a crucial role in favouring crystallisation. In table 3.1 the numbers of neighbours and distances in *fcc* and *hcp* are listed [45]. The numbers of the first and the second nearest-neighbour in *fcc* are the same as those in *hcp*. Therefore, the difference in free

The nth neighbour	♯ in *fcc*	♯ in *hcp*	x_n/R
1st	12	12	2
2nd	6	6	$\sqrt{\frac{24}{3}}$
3rd	0	2	$\sqrt{\frac{32}{3}}$
4th	24	18	$\sqrt{\frac{36}{3}}$
5th	0	12	$\sqrt{\frac{44}{3}}$
6th	12	6	$\sqrt{\frac{48}{3}}$
7th	24	12	$\sqrt{\frac{60}{3}}$
8th	0	12	$\sqrt{\frac{68}{3}}$
9th	8	6	$\sqrt{\frac{72}{3}}$

Table 3.1. Numbers of the nth nearest neighbour in *fcc* and *hcp* are listed. x_n is the distance from the centre of the reference particle to that of the nth nearest neighbour, and R the radius of the particle.

energies between *fcc* and *hcp* structures is extremely small. Colot and Baus [45] have studied structural ($fcc - hcp$) phase transition via density functional theory. However, their calculations indicated that the free energy differences between the *fcc* and *hcp* solids are too small to be differentiated. Iglói [46] claimed that the *fcc* structure is slightly more stable than the *hcp* one; however, the difference in the grand potentials is comparable with the error of the calculation. It is therefore possible for a compact lattice to contain faults, a layer A being substituted for a layer B or C. For example, in the hexagonal series

$$...ABAB\underline{ABC}BCBCBC...$$

there is one fault because there is one group of three consecutive layers which is of the cubic type while all the others are of the hexagonal type. In the same way, the cubic arrangement

$$...ABCABC\underline{AB\overline{A}C\overline{A}}BCABCABCA...$$

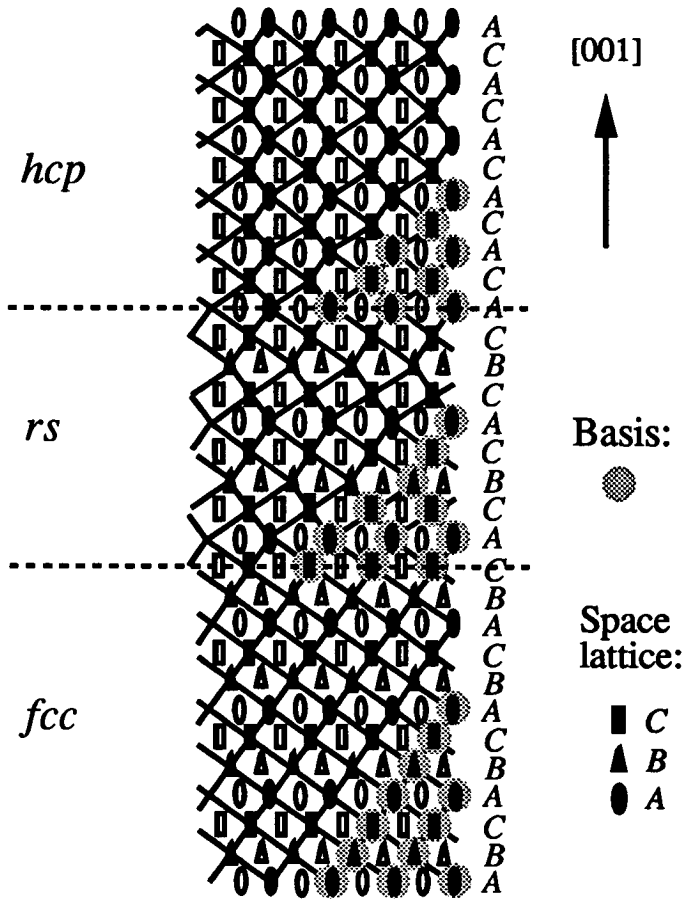

Figure 3.2. The top part shows the perfect *hcp* structure. The middle part shows a random-stacked structure (*rs*). The bottom part shows the perfect *fcc* structure. Plane of main drawing is (100) of the *hcp* structure.

contains two hexagonal triplets, and therefore two faults. In figure 3.2, filled signs represent particles in the plane of the drawing, open signs those in the plane immediately above or below. It is quite obvious that for perfect *fcc* and *hcp* structure, the lattice is very regular. The random-stacked part shows the mixture of *fcc* and *hcp*. Dashed line can be considered as the boundary of different ways of packing. Note that the crystal structure is formed by the addition of the basis to every lattice point of the space lattice.

With respect to atomic materials, X-ray analysis has shown that stacking faults are formed, for example, in cobalt. It has long been known that the structure of cobalt is a hexagonally close-packed random-stacked structure with a low degree of randomness, the frequency of faults in the specimen investigated by Edwards *et al.* is found to be, on the average, about one in every ten planes [47][48].

Random stacking of colloidal spheres was also found in gem opals which are composed of spherical particles of amorphous silica. Gem opals were examined in an optical diffractometer by Sanders and found to consist of particles arranged hexagonally in layers which are usually stacked randomly [49]. However, Sanders was not able to quantitatively characterise the structure of opals.

In 1941 A.J.C. Wilson [50][51] first developed a theory to interpret the diffraction pattern of cobalt crystal. Because this treatment successfully explains the diffraction pattern, we will adopt his theory to discuss how the stacking faults distort the reciprocal space. The mathematical treatment of close-packed random-stacked structure will also be elucidated in the next section.

3.3 Materials and methods

3.3.1 The effect of polydispersity on $S^M(Q)$ for fluid state

In this section, Vrij's treatment is adopted to calculate $S^M(Q)$, considering the case of polydisperse hard spheres. Owing to the complicated process of derivation, the equations are not reproduced here. It can be found in Ref. [52][53]. Here we also adopt Schulz particle size distribution modelled by a set of delta functions to study the effect of polydispersity on $S^M(Q)$ although van Beurten and Vrij have studied this subject before [54]. However, they slightly misused Schulz particle size distribution (See appendix C.).

Briefly speaking, the process of deriving the scattered light intensity by Vrij is as follows:

1. Start from the fluctuation theory of light scattering for multicomponent system of hard spheres to calculate normalised scattering intensity (or called Rayleigh ratio).

2. Formulate an equation for light scattering from spherically symmetrical particles in terms of direct correlation functions.

3. These direct correlation functions can be defined by the multicomponent Ornstein-Zernike relation, formulated by matrix equations.

4. These matrix equations can then be evaluated further by Baxter's Q function. Therefore, $< I >$ can be solved exactly.

In chapter 2, equation (2.32) shows the Rayleigh scattering which can be normalised to give [53]

$$< I(Q) >= \rho\gamma\overline{R^6}\bar{P}(QR)S^M(Q) \tag{3.8}$$

where $\rho = \phi/(\frac{4}{3}\pi\overline{R^3})$ is the number density, ϕ is colloidal volume fraction, $\gamma = \sqrt{2}\pi n\lambda_o^{-2}(\pi/6)(\frac{dn}{d\phi})$, n is the refractive index of the colloidal dispersion, λ_0 the wavelength of the incident light in vacuum. The structure factor $S^M(Q)$ then can be calculated [54].

To evaluate $\bar{P}(QR)$ for polydisperse hard spheres, one of the simplest approaches is to assume the scattering material inside particles is uniform. The result is shown in figure 2.2. Again, for extremely dilute case, $S^M(Q) = 1$. Here the normalised scattering intensity can be computed via Vrij's treatment. According to equation (3.7), $S^M(Q)$ can be calculated if $\bar{P}(QR)$ is known. Note that the scattering density distribution inside the particle is crucial in determining the shape of the single particle form factor [54]. It is, therefore, important to study the effect of polydispersity on $S^M(Q)$. Figure 3.3 shows the result at colloid volume fraction $\phi = 0.35$ for different polydispersities, considering the uniform distribution of scattering material inside the particle. It is found

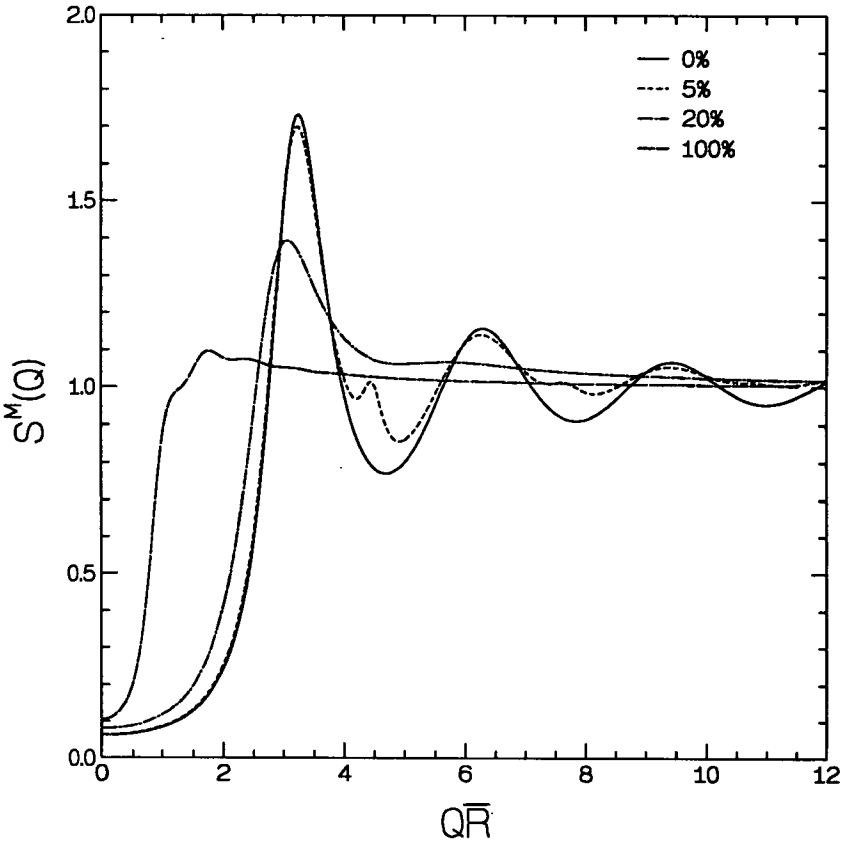

Figure 3.3. Structure factor $S^M(Q)$ at colloidal volume fraction $\phi = 0.35$ for samples of different polydispersity labelled on the right top under the consideration of homogeneous hard spheres.

that the position of the first maximum shifts to the left as polydispersity σ increases. This phenomenon results from the contribution by the larger particles. Additionally, at $Q\bar{R} \simeq 4.5$ the hump is very obvious for $\sigma = 5\%$ but gradually washed out as σ increases. The positions of the humps are about the minima in $\bar{P}(QR)$ (See figure 2.2.).

van Beurten and Vrij [54] also considered an extreme case that the spatial density

distribution of scattering material inside the particle is a Gaussian form. This gives

$$P(QR) = \exp\left(-\frac{1}{5}Q^2R^2\right) \tag{3.9}$$

that the expressions (2.7) and (3.9) give the same initial slope when expanded in Q^2, which implies identical radii of gyration. By calculating $S^M(Q)$ what they found is there shows no hump even at small polydispersity. In addition, the form factor of hard spheres for this case is very different from that for homogeneous hard spheres. (See reference [54].)

3.3.2 Close-packed random-stacked crystal

In section 3.2.3 we have presented the concept of stacking faults in close-packed structures. These types of imperfections have been observed in many crystals and it is therefore important to understand their effects on diffraction patterns.

First let us consider the hexagonal closed-packed arrangement: after AB or AC we should have A. This means the type of a certain layer should be the same as that of the one before its previous layer. We also have to assume that there exists a probability α of making a mistake. This implies that after pair AB it is possible to have C. Here we have to emphasise that $...ABABAB...$, $...ACACAC...$, $...BCBCBC...$ are identical.

To calculate diffraction pattern from close-packed random-stacked crystals, assume the type of the jth layer, which is the reference layer, is A, and define the probability for the $(j+m)$th layer having the same type as that of the jth layer is P_m. The calculation of P_m requires the knowledge of the combination of three consecutive layers, the $(j+m)$th, $(j+m-1)$th, and $(j+m-2)$th layers. In table 3.2 all the possible combinations of those three consecutive layers are listed. (Because m may be positive or negative integer, this discussion sufficiently characterises the properties of close-packed random-stacked structure.)


EX BIBL UNIV. EDINBURGEN.

layer	1	2	3	4	5	6
.	.	.	.	.	.	.
.	.	.	.	.	.	.
.	.	.	.	.	.	.
$j+m$	A or C	A or B	B or C	B or C	A or B	A or C
$j+m-1$	B	C	A	A	C	B
$j+m-2$	A	A	B	C	B	C
.	.	.	.	.	.	.
.	.	.	.	.	.	.
.	.	.	.	.	.	.
j	A					

Table 3.2. The possible combinations of a close-packed random-stacked structure along [001] direction of *hcp* structure. Assume the plane type of the jth layer is A.

If the type of the $(j+m-2)$th layer is A (column 1 and 2), we know that the $(j+m-1)$th layer absolutely will not adopt type A, but will be B or C. Therefore, after pair AB or AC we hope to have A, that is, ABA or ACA. However, a mistake could happen to the choice of the $(j+m)$th layer, that is, after pair AB and AC we got C and B respectively. This faulty stacking probability, happening to the $(j+m)$th layer, is α. Hence, $P_m = P_{m-2} \times (1-\alpha)$. This means the probability P_m of the $(j+m)$th layer having the same type as that of the jth layer is dependent not only on the probability P_{m-2} of the $(j+m-2)$th layer having the same type as that of the jth layer but also on $(1-\alpha)$, the chance of adopting A by the $(j+m)$th layer, that is to say the chance that a mistake is not made for the $(j+m)$th layer has to be taken into account.

If the type of the $(j+m-1)$th layer is A (column 3 and 4), the probability for the $(j+m)$th layer to choose type A is zero. Therefore, $P_m = 0$.

In the case of column 5 and 6, the $(j+m-1)$th and $(j+m-2)$th layers do not have type A. The probability for this kind of combination, BC or CB, is $(1-P_{m-1}-P_{m-2})$. Note that the probability for the $(j+m-2)$th layer to choose the plane type which is not type A is $1-P_{m-2}$, and the probability for the $(j+m-1)$ layer to choose the plane

type which is not type A is $1 - P_{m-1}$. However, they are not completely independent events because the type of the $(j+m-1)$th layer should be different from that of the $(j+m-2)$th layer. Therefore, the probability for the combination BC or CB is not simply $(1-P_{m-1}) \times (1-P_{m-2})$. Again, after pair BC and CB we hope to have B and C, respectively, to give *hcp*. But the chance of the $(j+m)$th layer making a mistake, choosing type A, is α. This gives $P_m = (1 - P_{m-1} - P_{m-2}) \times \alpha$.

We have now discussed all the possible combinations shown in table 3.2. Combining all the conclusions discussed above, we get

$$P_m = P_{m-2} \times (1-\alpha) + P_{m-1} \times 0 + (1 - P_{m-1} - P_{m-2}) \times \alpha \tag{3.10}$$

In order to solve this equation we have to consider the boundary conditions: $P_0 = 1$ and $P_1 = 0$, and assume m is positive, then equation (3.10) is solvable (see appendix D). The solution of this equation is

$$P_m = \frac{1}{3} + Q_e {\rho_e}^m + Q_o {\rho_o}^m \tag{3.11}$$

where $\rho_e = [-\alpha + \sqrt{4 - 8\alpha + \alpha^2}]/2$, $\rho_o = -[\alpha + \sqrt{4 - 8\alpha + \alpha^2}]/2$, and Q_e, Q_o are chosen to satisfy the boundary conditions. The values are found to be

$$Q_e = \frac{1}{3}\left[1 - \frac{1-\alpha}{\sqrt{4 - 8\alpha + \alpha^2}}\right]$$
$$Q_o = \frac{1}{3}\left[1 + \frac{1-\alpha}{\sqrt{4 - 8\alpha + \alpha^2}}\right]$$

Note that $\rho_{'s}$ and $Q_{'s}$ could be complex (see appendix E for further discussion). Because equation (3.10) can be solved only for m positive, we also have to consider what happens for m negative. We surmise that the chance of the $(j+m)$th layer being like the jth must be the same as that of the jth layer being like the $(j+m)$th, i.e. $P_{-m} = P_m$. If $\alpha = 0$ which corresponds perfect *hcp* structure, then $P_m = \frac{1}{2} + \frac{1}{2} \times (-1)^m$. If $\alpha = 1$

which corresponds to perfect fcc structure, then $P_m = \frac{1}{3}\left[1 + 2 \times (-1)^m \cos(\frac{m\pi}{3})\right]$ (see appendix E for details). Now let us go back to check the combinations in table 3.2. Assume the structure is perfect fcc, $\alpha = 1$. Then put any integer m to the result shown above. P_m will exactly indicate the fcc sequence by reference to the type of the jth layer.

So far we have found P_m. The next stage is to understand how the P_m distorts the scattered intensity for the close-packed random-stacked structure. For convenience, let us consider each unit cell to be a scatterer and $\mathbf{R}_t$ is the position of the t-th unit cell relative to an origin O. According to the theory of diffraction from crystals, the scattering amplitude by the t-th unit cell is

$$F_t = \sum_{u=1}^{s} f_{tu} \exp i\mathbf{Q} \cdot \mathbf{r}_u \tag{3.12}$$

where u runs over the s particles of the t-th unit cell, f_{tu} is the scattering amplitude by the uth particle whose position is $\mathbf{r}_u$ in the t-th unit cell. Then the intensity of scattered light by the crystal is

$$< I >= \left\langle \sum_v \sum_t F_t F_v^* \exp i\mathbf{Q} \cdot (\mathbf{R}_t - \mathbf{R}_v) \right\rangle \tag{3.13}$$

A unit cell can be defined by a set of crystal axes, $\mathbf{a}_1$, $\mathbf{a}_2$, $\mathbf{a}_3$. We select hexagonal axes in the reference plane, and set in the layer A. The length c is equal to the distance between two neighbouring layers; then $c = \sqrt{\frac{2}{3}}a$. The conventional unit cell has $a_1 = a_2 = a$ with an included angle of 120°. The $\mathbf{a}_3$ axis is normal to the plane of $\mathbf{a}_1$ and $\mathbf{a}_2$ (see figure 3.1). However, the hexagonal unit cell chosen here contains one particle only because we set $\mathbf{c} = \frac{1}{2}\mathbf{a}_3$. Therefore,

$$\mathbf{R}_t = j_1\mathbf{a}_1 + j_2\mathbf{a}_2 + j_3\mathbf{c}$$

$$\mathbf{R}_v = m_1\mathbf{a}_1 + m_2\mathbf{a}_2 + m_3\mathbf{c}$$

where $j's$ and $m's$ are integers. Note that the unit cell chosen here is different from the conventional *hcp* unit cell which contains 2 lattice points. One has to realise that the indices (hkl) used here equals the conventional (hkl') where $l' = 2l$, for example, (001) used here means the conventional (002). Calculation using equation (3.13) requires the knowledge of F_t and F_v which are the scattered amplitude by the t-th and v-th unit cell respectively. Let us consider first a structure without stacking faults, such as a *fcc* or *hcp* structure. It is known that the scattered amplitude by each unit cell is equal. Thus, the factor FF^* can be moved out of the summation term and only phase factors left. Now let us turn back to the case of the random-stacked structure. As mentioned before, the stacking faults only occur along $[001]_{hcp}$. Therefore, the scattered amplitude by each unit cell whose basal $(001)_{hcp}$ plane is in the same layer is equal. Equation (3.13) then can be rewritten to give

$$< I >= \left\langle \sum_{j_1}\sum_{j_2}\sum_{j_3} e^{i(j_1\mathbf{Q}\cdot\mathbf{a}_1)} e^{i(j_2\mathbf{Q}\cdot\mathbf{a}_2)} e^{i(j_3\mathbf{Q}\cdot\mathbf{c})} F_{j_3} \times \right.$$

$$\left. \sum_{m_1}\sum_{m_2}\sum_{m_3} e^{-i(m_1\mathbf{Q}\cdot\mathbf{a}_1)} e^{-i(m_2\mathbf{Q}\cdot\mathbf{a}_2)} e^{-i(m_3\mathbf{Q}\cdot\mathbf{c})} F^*_{m_3} \right\rangle \qquad (3.14)$$

We also can set $j_3 = j$ and $m_3 = j + m$. The problem turns out to be simple. What we need to do is to calculate the average value of $F_j F^*_{j+m}$.

The argument discussed above is concentrated on the assumption that the type of the jth layer which is the reference plane is A. In fact, there is no necessity for the jth layer to be in plane A. The others, B and C, are adopted with equal. Therefore,

$$F_j = \frac{1}{3}(F_A + F_B + F_C) \qquad (3.15)$$

Note that the adjacent layers are displaced relative to each other by $\frac{1}{3}(\mathbf{a}_1 + 2\mathbf{a}_2)$ or $\frac{1}{3}(2\mathbf{a}_1 + \mathbf{a}_2)$ shown in figure 3.1. According to (3.12) and the hexagonal unit cell chosen here (See figure 3.1.), we can write

$$
\begin{aligned}
F_A &= f \exp 0 = f \\
F_B &= f \exp i\mathbf{Q} \cdot \left[\frac{1}{3}(2\mathbf{a}_1 + \mathbf{a}_2)\right] \equiv f \exp i\mathbf{Q} \cdot \left[\frac{1}{3}(-\mathbf{a}_1 + \mathbf{a}_2)\right] \\
F_C &= f \exp i\mathbf{Q} \cdot \left[\frac{1}{3}(\mathbf{a}_1 + 2\mathbf{a}_2)\right] \equiv f \exp i\mathbf{Q} \cdot \left[\frac{1}{3}(\mathbf{a}_1 - \mathbf{a}_2)\right]
\end{aligned}
$$

The sign "$\equiv$" used above represents the concept of structural identity (see section 3.2.3). Here we assume the particles in the system are identical and f is the scattered amplitude by the particles in a unit cell. As for F_{j+m}, the probability for the $(j+m)$th layer to be in plane A is P_m and to be in plane B or C is $\frac{1}{2}(1 - P_m)$ equally (If the reference layer adopted here is B or C, the argument is the same, giving only a permutation of symbols.). Therefore,

$$
F_{j+m} = P_m F_A + \frac{1}{2}(1 - P_m)(F_B + F_C) \tag{3.16}
$$

The calculation of $F_j F^*_{j+m}$ is feasible now by reference to equation (3.11), (3.15), and (3.16). The result is quite simple:

$$
F_j F^*_{j+m} = f^2 \left[\frac{1 + 2K}{3} + (1 - K)\left(Q_e {\rho_e}^m + Q_o {\rho_o}^m\right)\right] \tag{3.17}
$$

where $K = \cos(2\pi \frac{h-k}{3})$, and $\mathbf{Q} \cdot \mathbf{a}_1 = 2\pi h$, $\mathbf{Q} \cdot \mathbf{a}_2 = 2\pi k$, $\mathbf{Q} \cdot \mathbf{c} = 2\pi l$ (refer to section 3.3.4). Assume the numbers of unit cells in direction $\mathbf{a}_1$, $\mathbf{a}_2$, and $\mathbf{c}$ are n_1, n_2, and n_3, respectively. Equation (3.14) can then be rewritten to give

$$
I = \frac{\sin^2(\pi n_1 h)}{\sin^2(\pi h)} \frac{\sin^2(\pi n_2 k)}{\sin^2(\pi k)} \sum_{j=1}^{n_3} \sum_{m_3=1}^{n_3} F_j F^*_{m_3} e^{i(j-m_3)\mathbf{Q}\cdot\mathbf{c}} \tag{3.18}
$$

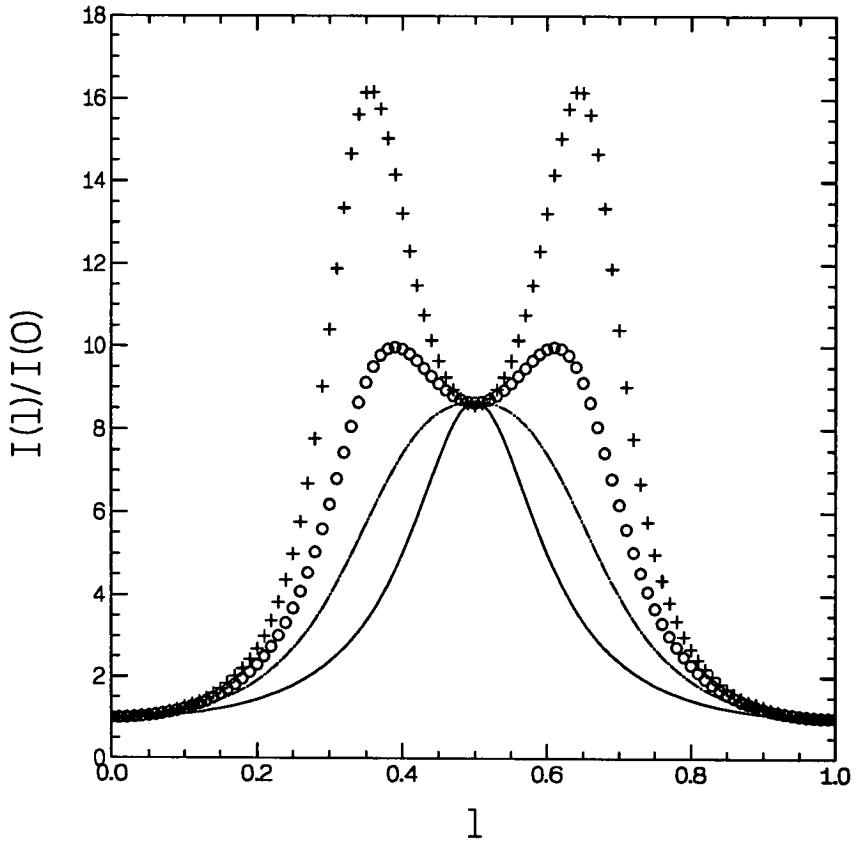

Figure 3.4. The normalised diffuse scattering intensity along $10l$ line in reciprocal space. Solid line is for $\alpha = 0.50$, dashed line for $\alpha = 0.57$, circle for $\alpha = 0.63$, plus sign for $\alpha = 0.70$. See text for details.

The faulty stacking probability appears only in the summation term, as we should expect. The calculation of (3.18) is not easy. However, let us put (3.17) in (3.18) first and see what the resulting form looks like. The result is quite intriguing:

$$I = f^2 \frac{\sin^2(\pi n_1 h)}{\sin^2(\pi h)} \frac{\sin^2(\pi n_2 k)}{\sin^2(\pi k)} \left[\left(\frac{1+2K}{3} \right) \frac{\sin^2(\pi n_3 l)}{\sin^2(\pi l)} + \right.$$

$$\left. (1-K) \sum_{m=-(n_3-1)}^{n_3-1} (n_3 - |m|) \left(Q_e \rho_e{}^{|m|} + Q_o \rho_o{}^{|m|} \right) e^{-im\mathbf{Q}\cdot\mathbf{c}} \right] \qquad (3.19)$$

This expression clearly indicates that, with respect to rows having indices hk such that

$(h-k)/3$ is integral, that is to say that $K = 1$, the summation term in square bracket is zero. It implies that, in reciprocal space of the *hcp* structure along *hkl* rows whose value of $(h-k)/3$ is integral, the scattered intensity will not be distorted by the faulty stacking probability but appear as nodes which are common to both perfect *fcc* and *hcp* structures. It is obvious that the faulty stacking probability α only occurs in the summation term in square bracket. Here we use nodes rather than points in reciprocal space because the finite size of a real crystal broadens the points into nodes (and lines into rods) [41].

When $(h-k)$ is not divisible by three, the expression in square bracket in equation (3.19) depends on α in a very complicated way. Figure 3.4 shows the diffuse scattering distribution along $10l$ line. It is clear that the split peaks in figure 3.4 will move towards $(10\frac{1}{3})$ and $(10\frac{2}{3})$ which correspond to perfect *fcc* structure when α increases. This implies that stacking faults not only broaden regular crystal reflections but also shift the Bragg peak. The very complicated resulting form of eq. (3.19) can be found in reference [50].

3.3.3 Thermal diffuse scattering

The term "diffuse scattering" is especially used to describe the effects of perturbations, resulting from imperfect crystals, in the crystal lattice on the diffraction pattern.

With respect to an imperfect crystal, a strong diffraction peak caused by the average ideal lattice still can be obtained, but in other directions the light scattered by particles sitting on the faulty lattice site does not cancel perfectly by interference because cancellation is the direct consequence of the perfect periodicity of the diffracting medium. Therefore, there is no doubt that the imperfect structure will broaden the diffraction line. Similarly, the finite size of crystal also broadens the diffraction line due to the incomplete cancellation in other directions near Bragg reflection even if the periodicity

of the crystal lattice is perfect [41].

Particles will also undergo the thermal vibration about their equilibrium positions on the lattice sites in a crystal. Does this random thermal displacement of the particles broaden the diffraction line? Let the random thermal displacement of the ith particle at mean position $\bar{r}_i$ be Δr_i. The average intensity scattered by a crystal is

$$< I >= \sum_i \sum_j f_i f_j^* \left\langle e^{i\mathbf{Q}\cdot(\bar{\mathbf{r}}_i - \bar{\mathbf{r}}_j)} e^{i\mathbf{Q}\cdot(\Delta\mathbf{r}_i - \Delta\mathbf{r}_j)} \right\rangle \tag{3.20}$$

Assume particle's random displacement is uncorrelated with its position. Then we can decouple the two exponentials in bracket in equation (3.20). Now the aim is to deal with $\left\langle e^{i\mathbf{Q}\cdot(\Delta\mathbf{r}_i - \Delta\mathbf{r}_j)} \right\rangle$. If the random displacement of the particles is very small, We can adopt an approximate approach:

$$\begin{aligned} \left\langle e^{i\mathbf{Q}\cdot(\Delta\mathbf{r}_i - \Delta\mathbf{r}_j)} \right\rangle &= \left\langle 1 + i\mathbf{Q}\cdot(\Delta\mathbf{r}_i - \Delta\mathbf{r}_j) - \frac{1}{2}Q^2(\Delta\mathbf{r}_i - \Delta\mathbf{r}_j)^2\cos^2\theta + \ldots \right\rangle \\ &= 1 - \frac{1}{3}Q^2(\Delta r^2 - \langle \Delta\mathbf{r}_i \cdot \Delta\mathbf{r}_j \rangle) + \ldots \\ &\simeq e^{-\frac{1}{3}Q^2\Delta r^2} e^{\frac{1}{3}Q^2\langle \Delta\mathbf{r}_i \cdot \Delta\mathbf{r}_j \rangle} \end{aligned} \tag{3.21}$$

where the mean-square displacement $\langle \Delta r_i^2 \rangle = \Delta r^2$, and θ the angle between $\mathbf{Q}$ and $\Delta\mathbf{r}_i - \Delta\mathbf{r}_j$. Note that $\langle \cos^2\theta \rangle = \frac{1}{4\pi}\int \cos^2\theta d\Omega = \frac{1}{3}$, where Ω is the solid angle. If we suppose each particle fluctuates independently about its own equilibrium position, known as the Einstein model of a solid, the term $\langle \Delta\mathbf{r}_i \cdot \Delta\mathbf{r}_j \rangle = 0$ for $i \neq j$. Then equation (3.20) can be written to give

$$< I >= f^2 e^{-\frac{1}{3}Q^2\Delta r^2} \sum_i \sum_j \left\langle e^{i\mathbf{Q}\cdot(\bar{\mathbf{r}}_i - \bar{\mathbf{r}}_j)} \right\rangle + N f^2 (1 - e^{-\frac{1}{3}Q^2\Delta r^2}) \tag{3.22}$$

In equation (3.22) the second term of the right-hand side produces a scattering background in all directions, and the exponential factor, the so-called Debye-Waller factor,

attenuates the crystal reflection shown in the first term. In atomic systems, this model works very well at high temperatures. Note that from this result thermal motion does *not* broaden, but simply attenuates the reflection by a crystal.

Strictly speaking, the random thermal vibration of the particles is not independent [55][56]. This leads to an attempt to relate the cross term to the mean-square displacement by means of an interaction coefficient, that is, $\langle \Delta \mathbf{r}_i \cdot \Delta \mathbf{r}_j \rangle = \xi_{ij} \Delta r^2$. The interaction coefficient $\xi_{ii} = 1$ corresponds to self-correlation. For $i \neq j$, $\xi_{ij} \neq 0$. This indicates that the collective motion of the particles is significant and can not be neglected. Equation (3.20) can then be rewritten as

$$< I >= N f^2 + \sum_{i \neq j} f^2 \left\langle e^{i\mathbf{Q}\cdot(\bar{\mathbf{r}}_i - \bar{\mathbf{r}}_j)} \right\rangle e^{-\frac{1}{3}Q^2\Delta r^2} e^{\frac{1}{3}Q^2\Delta r^2 \xi_{ij}} \tag{3.23}$$

For a coupled system, the interaction coefficient, ξ_{ij}, implies the degree to which $\Delta \mathbf{r}_i$ and $\Delta \mathbf{r}_j$ are correlated. Therefore, $\xi_{ij} < 1$ for $i \neq j$. This elucidates that the degree to which two discrete particles are coupled is always smaller than that of self-correlation. Accordingly, the approximation is justifiable: $e^{\frac{1}{3}Q^2\Delta r^2 \xi_{ij}} \simeq 1 + \frac{1}{3}Q^2 \Delta r^2 \xi_{ij}$. Finally, equation (3.23) can be written to give

$$\begin{aligned} < I > &= N f^2 + f^2 e^{-\frac{1}{3}Q^2\Delta r^2} \sum_{i \neq j} \left\langle e^{i\mathbf{Q}\cdot(\bar{\mathbf{r}}_i - \bar{\mathbf{r}}_j)} \right\rangle + \frac{1}{3} Q^2 \Delta r^2 e^{-\frac{1}{3}Q^2\Delta r^2} f^2 \sum_{i \neq j} \left\langle \xi_{ij} e^{i\mathbf{Q}\cdot(\bar{\mathbf{r}}_i - \bar{\mathbf{r}}_j)} \right\rangle \\ &= f^2 e^{-\frac{1}{3}Q^2\Delta r^2} \sum_i \sum_j \left\langle e^{i\mathbf{Q}\cdot(\bar{\mathbf{r}}_i - \bar{\mathbf{r}}_j)} \right\rangle \\ &\quad + f^2 \left(1 - e^{-\frac{1}{3}Q^2\Delta r^2}\right) \sum_i \sum_j \left\langle \xi_{ij} e^{i\mathbf{Q}\cdot(\bar{\mathbf{r}}_i - \bar{\mathbf{r}}_j)} \right\rangle \end{aligned} \tag{3.24}$$

using the form $x e^{-x} \simeq (e^x - 1)e^{-x} = 1 - e^{-x}$ for very small x. Briefly, this result can be expressed as

$$< I >= e^{-\frac{1}{3}Q^2\Delta r^2} < I >_{CR} + < I >_{TDS} \tag{3.25}$$

where the first term of the right-hand side is the contribution by regular crystal reflection attenuated by the temperature factor, and the second term of the right-hand side is the contribution by so-called thermal diffuse scattering (TDS). It is clear from the expression of equation (3.25) that $< I >_{TDS}$ is not a monotonically varying function when including interactions between the particles. If we take $\xi_{ij} = 1$ in $< I >_{TDS}$, the double sum is exactly the same as that in $< I >_{CR}$. So, it is evident that $< I >_{TDS}$ more or less coincides with the regular crystal reflection.

It is not easy to characterise ξ_{ij} if $i \neq j$. For simplicity, let us consider the normal coordinates of the lattice vibrations. In the case of a coupled system containing particles all of one kind, assume the elastic wave s whose amplitude with a polarization of mode p is $\mathbf{A}_{p,s}$ is harmonic. The vibrations of the lattice could be represented by a set of independent stationary modes of vibration [57]:

$$\triangle \mathbf{r}_i = \sum_p \sum_s \mathbf{A}_{p,s} \cos\left(\omega_{p,s} t - \mathbf{q}_s \cdot \bar{\mathbf{r}}_i\right) \tag{3.26}$$

where $\omega_{p,s}$ is the frequency of vibration with a polarization of mode p, $\mathbf{q}_s$ the propagation vector of elastic wave s. Notice that for each wavevector within the first Brillouin zone there are three modes, one of longitudinal polarization and two of transverse polarization ($p = 1, 2, 3$) [43]. The relation between the mean-square displacement and the mean-square amplitude can be obtained as below

$$< \triangle \mathbf{r}_i^2 >= \frac{1}{2} \sum_p \sum_s \left\langle A_{p,s}^2 \right\rangle = \triangle r^2 \tag{3.27}$$

and the cross term is

$$\begin{aligned} < \triangle \mathbf{r}_i \cdot \triangle \mathbf{r}_j > &= \sum_p \sum_s \left\langle A_{p,s}^2 \cos\left(\omega_{p,s} t - \mathbf{q}_s \cdot \bar{\mathbf{r}}_i\right) \cos(\omega_{p,s} t - \mathbf{q}_s \cdot \bar{\mathbf{r}}_j) \right\rangle \\ &= \frac{1}{2} \sum_p \sum_s \left\langle A_{p,s}^2 \cos\left[\mathbf{q}_s \cdot (\bar{\mathbf{r}}_i - \bar{\mathbf{r}}_j)\right] \right\rangle \end{aligned}$$

$$= \triangle r^2 \frac{\sum_p \sum_s \left\langle A_{p,s}^2 \left[e^{i\mathbf{q}_s \cdot (\bar{\mathbf{r}}_i - \bar{\mathbf{r}}_j)} + e^{-i\mathbf{q}_s \cdot (\bar{\mathbf{r}}_i - \bar{\mathbf{r}}_j)} \right] \right\rangle}{2 \sum_p \sum_s \left\langle A_{p,s}^2 \right\rangle}$$

by using $\cos A \cos B = \frac{1}{2}[\cos(A+B) + \cos(A-B)]$, and the ensemble average including time average $\langle \cos(2\omega_{p,s}t - \mathbf{q}_s \cdot (\bar{\mathbf{r}}_i + \bar{\mathbf{r}}_j)) \rangle = 0$. Thus, one can write

$$\xi_{ij} = \frac{1}{2} \frac{\sum_p \sum_s \left\langle A_{p,s}^2 \left[e^{i\mathbf{q}_s \cdot (\bar{\mathbf{r}}_i - \bar{\mathbf{r}}_j)} + e^{-i\mathbf{q}_s \cdot (\bar{\mathbf{r}}_i - \bar{\mathbf{r}}_j)} \right] \right\rangle}{\sum_p \sum_s \left\langle A_{p,s}^2 \right\rangle} \tag{3.28}$$

Note that each elastic wave s is associated with a specific wavelength λ_s. Each λ_s modifies wavevector $\mathbf{q}_s$, that is, $q_s = 2\pi/\lambda_s$. The minimum wavelength is twice the interparticle spacing, $2a$. The maximum wavelength depends on the size of the crystal. The physical interpretation of ξ_{ij} is now feasible: the vibration of particle i affects the vibration of particle j via q_s, a "phonon".

At high temperatures Einstein model can work very well [43]. Thus we attempt this expression: $\xi_{ij} = \delta_{ij}$, and the result of eq. (3.24) will be exactly the same as eq. (3.22). However, let us put eq. (3.28) to (3.24), and restore $1 - e^{-\frac{1}{3}Q^2\triangle r^2}$ to be $\frac{1}{3}Q^2\triangle r^2 e^{-\frac{1}{3}Q^2\triangle r^2}$. At first, concentrating on the double summation term:

$$\sum_i \sum_j \left\langle \xi_{ij} e^{i\mathbf{Q} \cdot (\bar{\mathbf{r}}_i - \bar{\mathbf{r}}_j)} \right\rangle = \frac{\sum_{i,j} \sum_{p,s} \left\langle A_{p,s}^2 \left[e^{i(\mathbf{Q}+\mathbf{q}_s) \cdot (\bar{\mathbf{r}}_i - \bar{\mathbf{r}}_j)} + e^{i(\mathbf{Q}-\mathbf{q}_s) \cdot (\bar{\mathbf{r}}_i - \bar{\mathbf{r}}_j)} \right] \right\rangle}{4\triangle r^2} \tag{3.29}$$

This function will have sharp maxima at positions $\mathbf{Q}$ in reciprocal space such that $\mathbf{Q} \pm \mathbf{q}_s = \mathbf{H}_B$, where $\mathbf{H}_B$ represents the reciprocal vector from the origin to a certain reciprocal-lattice point. Note that if $\mathbf{Q}$ is given, only one $\mathbf{q}_s$ can satisfy this wavevector selection rule, ignoring the effect of size broadening. Therefore, one can write

$$f^2 \sum_i \sum_j \left\langle e^{i\mathbf{H}_B \cdot (\bar{\mathbf{r}}_i - \bar{\mathbf{r}}_j)} \right\rangle = I_{Bragg} \tag{3.30}$$

The TDS term then can be represented as

$$< I >_{TDS} = e^{-\frac{1}{3}Q^2\Delta r^2}\frac{Q^2}{6}\sum_p\sum_s\left\langle A_{p,s}^2\right\rangle I(\mathbf{q}_s) \tag{3.31}$$

where $I(\mathbf{q}_s) = I_{Bragg}$ if $\mathbf{q}_s$ satisfies the wavevector selection rule, otherwise $I(\mathbf{q}_s) = 0$. Now the mean-square amplitude plays a crucial role in determining the intensity of TDS [58]. To study this, consider the mean kinetic energy of the system which is $\langle E_{kin}\rangle = \frac{m}{2}\sum_i \langle \triangle \dot{r}_i^2\rangle$. By reference to eq. (3.26), one can write

$$\langle E_{kin}\rangle = \frac{Nm}{4}\sum_p\sum_s\omega_{p,s}^2\left\langle A_{p,s}^2\right\rangle = \sum_p\sum_s\langle E_{p,s}\rangle \tag{3.32}$$

where N is the number of particles, and m the mass of a particle. According to the classical theory of harmonic oscillator, the mean kinetic energy of the oscillator [24] is $\langle E_{p,s}\rangle = \frac{3}{2}kT$. Therefore, the relation between the mean-square amplitude and temperature can be defined as:

$$\left\langle A_{p,s}^2\right\rangle = \frac{6kT}{Nm\omega_{p,s}^2} \tag{3.33}$$

Then, by (3.31) and (3.33),

$$< I >_{TDS} = e^{-\frac{1}{3}Q^2\Delta r^2}\frac{kT}{Nm}\sum_p\sum_s\left(\frac{Q}{\omega_{p,s}}\right)^2 I(\mathbf{q}_s) \tag{3.34}$$

If the dispersion relation [43] connecting $\omega_{p,s}$ and q_s is known, (3.34) can be calculated. An attempt was made to calculate the velocity of acoustic shear waves in colloidal crystals by Joanny [59]. By investigating the acoustic shear waves propagating in ordered suspensions of charged latex spheres, Joanny developed the dispersion relation and claimed that the viscous damping precludes the existence of short wavelength phonon and only low-frequency, long wavelength waves should propagate in colloidal crystals.

So far we have ignored any quantum effect because the sample system discussed in chapter 1 is far larger than atomic systems, so that the classical theory employed above is a very good approximation.

To summarise, we quote Max Born [60]:
"The effect of the thermal motion on an X-ray beam traversing the crystal has been compared with the effect of the agitated surface of the sea on the image of the setting sun. There is no sharp reflection, but a diffuse ribbon of light stretching towards the observer. This diffusion is obviously produced by the innumerable waves of various length and direction. In the same way a beam of X-rays passing through a crystal will be affected by the atomic waves which can be considered as the elements of the thermal motion. Each atomic wave modifies the direction, amplitude, frequency and phase of the reflected X ray."

3.3.4 Diffraction power by powder or polycrystallite

It can be found in lots of X-ray diffraction textbooks [58], [61] that there are six factors affecting the scattering intensity on diffraction patterns by powder method:

1. polarization factor

2. multiplicity factor

3. Lorentz factor

4. structure factor

5. temperature factor

6. absorption factor.

Here we do not reproduce the description of these factors. Additionally, the absorption factor is ignored in the later calculation.

It is quite helpful to interpret powder-diffraction pattern by reference to Ewald sphere construction in the reciprocal space. For polycrystalline materials, the small crystals

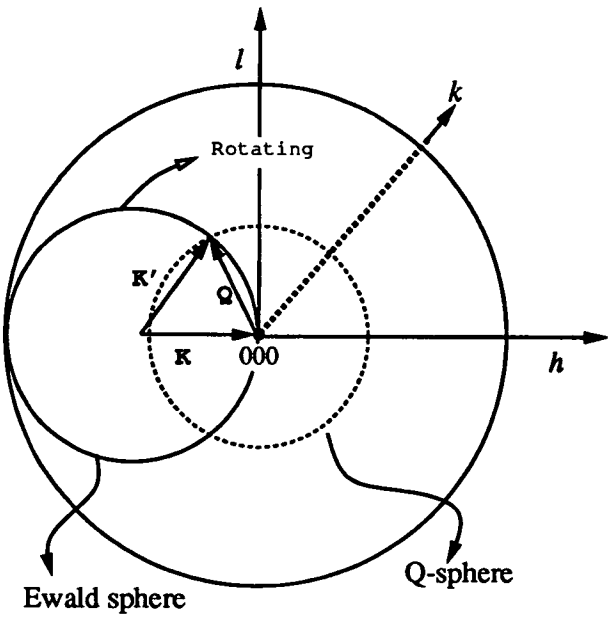

Figure 3.5. The procedure of orientational averaging. **K** is the propagation vector of incident light, **K**′ the propagation vector of scattered light, and **Q** the scattering vector. The "Q-sphere" is generated by rotating the Ewald sphere through all orientations around (000).

or grains are orientationally random. Therefore, to calculate the powder-diffraction pattern, the Ewald sphere has to take on all possible orientations around (000) in reciprocal space. This is the procedure of orientational averaging. The orientational averaging can be achieved by rotating the Ewald sphere through all orientations, as shown in figure 3.5. The generated "Q-sphere" is the result of orientational averaging. To study the "Q-sphere", the direction of scattered beams has to be clarified. Normally, $Q = \frac{4\pi}{\lambda}\sin\frac{\theta}{2}$, where θ is the scattering angle. However, for scattering vector **Q**, we need to define the direction. In the case of *hcp* structure, the lengths of three crystal axes are known as $a_1 = a_2 = a$, and $c = \sqrt{\frac{2}{3}}a$, where a is the nearest-neighbour distance. Therefore, in reciprocal space of *hcp* structure (refer to appendix F)

$$\mathbf{Q} = \frac{4\pi}{\sqrt{3}a}\left(h\mathbf{b}_1 + k\mathbf{b}_2 + l\sqrt{\frac{9}{8}}\mathbf{b}_3\right) \tag{3.35}$$

and

$$Q = |\mathbf{Q}| = \frac{4\pi}{\sqrt{3}a}\sqrt{\left(h^2 + k^2 + hk + \frac{9}{8}l^2\right)} \tag{3.36}$$

because $\mathbf{b}_1 \cdot \mathbf{b}_2 = \cos 60^o$. Here $\mathbf{b}_1$, $\mathbf{b}_2$, $\mathbf{b}_3$ are unit vectors reciprocal to $\mathbf{a}_1$, $\mathbf{a}_2$, $\mathbf{c}$. To calculate $I(Q)$ at a given value of Q, we have to consider all the contributions by $I(\mathbf{Q})$ on the surface of the "Q-sphere" in a reciprocal space. Therefore, one can write

$$I(Q) = \frac{1 + \cos^2\theta}{\sin^2\frac{\theta}{2}\cos\frac{\theta}{2}} \int_{\Omega} I(\mathbf{Q}) d\Omega \tag{3.37}$$

where Ω is the solid angle and θ the scattering angle, taking account of Lorentz-polarization factor. In order to make the numerical calculation feasible, the surface of the "Q-sphere" is divided into a finite number of elements $\triangle A$. Then, (3.37) can be approximately represented as

$$I(Q) \simeq \frac{1 + \cos^2\theta}{\sin^2\frac{\theta}{2}\cos\frac{\theta}{2}} \sum_{\triangle A} I(\mathbf{Q}) \tag{3.38}$$

where the sum runs over all the elements on the surface of the "Q-sphere". According to this procedure, a model written in FORTRAN 77 program can be established to characterise the scattered pattern by close-packed random-stacked crystals by adopting (3.18), (3.22), and (3.38). The adjustable parameters are the number of unit cells in all crystal axes, the interparticle spacing, the faulty stacking probability, and the thermal displacement if only considering the Einstein model.

According to Wilson's theory discussed in section 3.3.2, the structure of a close-packed random-stacked crystal can be characterised. In figure 3.6 the hexagonal reciprocal space of a random-stacked structure with $\alpha = 0.5$ is built. The scattering density distribution along $10l$ is also illustrated by reference to figure 3.4. On the top of both $10l$ and $20l$ rods show the scattering-density distribution across the rod. The shape of

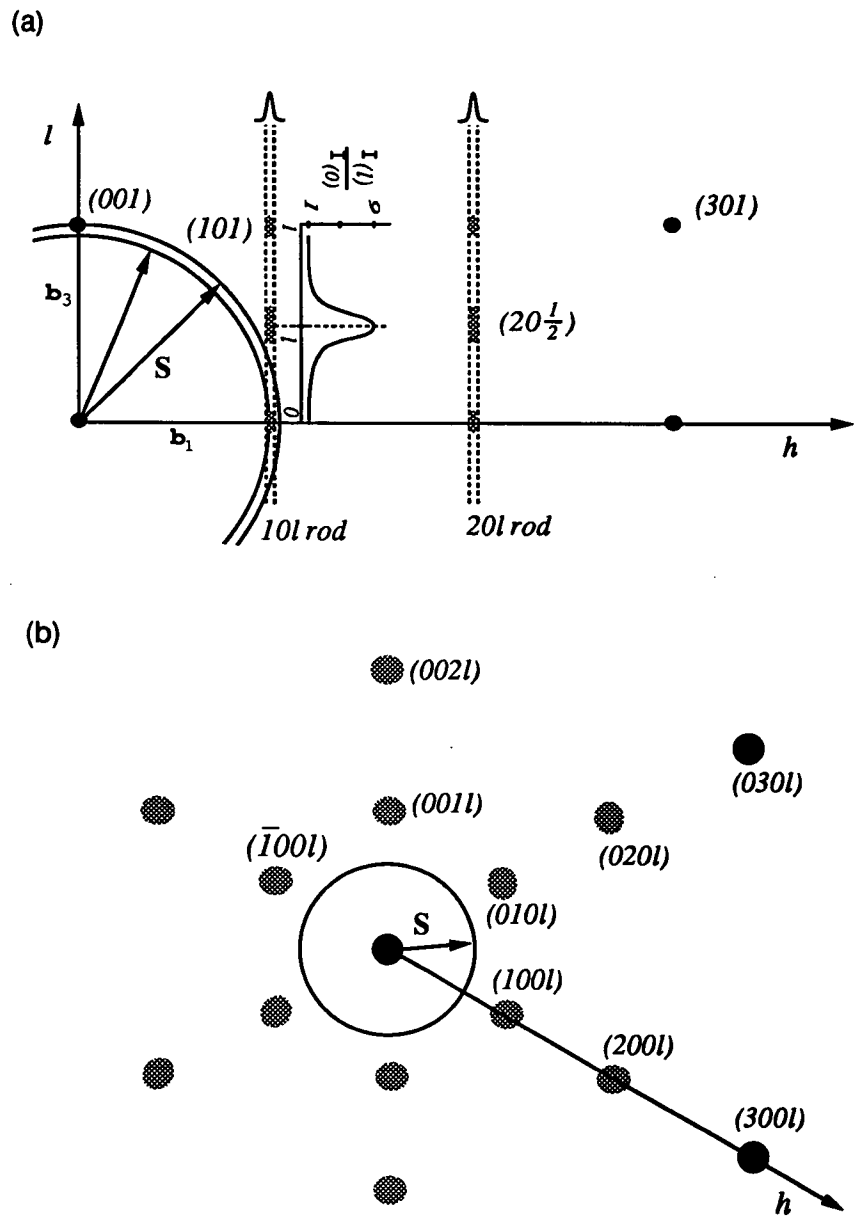

Figure 3.6. The reciprocal space of the close-packed random-stacked structure whose faulty stacking probability is 0.5 (a) 2-D $h-l$ space. (b) $h-k-i$ space. The "Q-sphere" construction is illustrated to interpret the scattered pattern in that $\mathbf{S} = \frac{\mathbf{Q}}{2\pi}$.

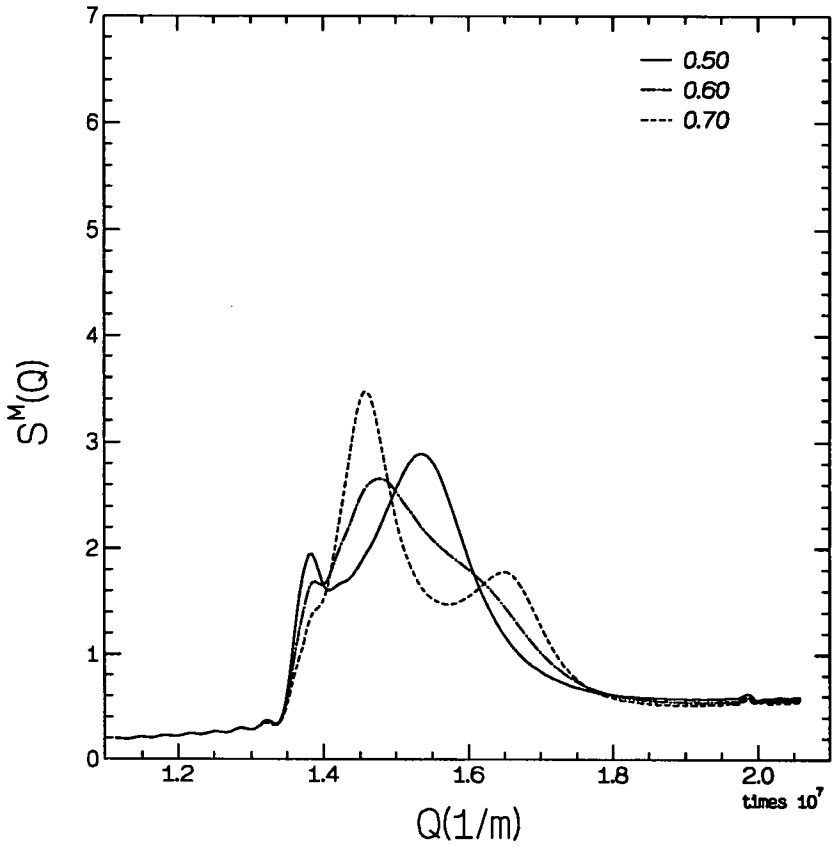

Figure 3.7. Diffuse scattering due to stacking faults of close-packed structure. Solid line is for $\alpha = 0.50$, dash-dot line for $\alpha = 0.60$, dashed line for $\alpha = 0.70$.

the scattering-density distribution depends on the one of the crystal [62][63].

To save computer time, the calculation is done in 2-D (see figure 3.6 (a)) and the scan of **Q** spans about left and right sides of $10l$ rod plus the contribution by (001) node, sidesteping the void region without any intensity density distribution. Then, multiplicity factor has to be considered. In eq. (3.38) the sum turns out to run over all segments on the "Q-circle". The segment is kept equal, set to be $S\triangle\theta$ where $\triangle\theta = 8 \times 10^5/S$, even if S increases. So far we ignored the factor Nf^2. Therefore, the calculation, in practice, reflects the measured structure factor, $S^M(Q)$. The results are shown in figure 3.7, ignoring the contribution by (001) node. The adjustable parameters

are chosen to be as follows:

1. The number of unit cells in all crystal axes: $40 \times 40 \times 35$.

2. The interparticle spacing: $530nm$.

3. The thermal displacement: $70nm$ (about 13% of the mean interparticle spacing [64]).

4. The faulty stacking probability α: 0.50, 0.60, and 0.70 for three independent runs.

In figure 3.7 the calculation indicates the "prepeak", at $Q \sim 1.4 \times 10^7 m^{-1}$, results from the large area of the intersection of Q-sphere with $10l$ rod shown in figure 3.6. Additionally, α decides the distribution of scattering intensity along $10l$ rod shown in figure 3.4. Therefore, at higher Q, not only the intersection area of Q-sphere with $10l$ rod but also the distribution of scattering intensity along $10l$ rod decide the shape of diffuse scattering.

To justify 2-D calculation, we select the adjustable parameters to be $\alpha = 0.5$, the numbers of unit cells in three crystal axes: 45-45-45, interparticle spacing: $530nm$, and random displacement: $70nm$, and then calculate the powder-diffraction pattern in 2-D and 3-D, respectively. The result is shown in figure 3.8. The only difference between 2-D and 3-D calculations is the "prepeak" that the peak at $Q \sim 1.38 \times 10^7 m^{-1}$ calculated in 2-D is slightly sharper than the one calculated in 3-D. The 3-D calculations are very time consuming and the shape of diffuse scattering calculated in 2-D and in 3-D is almost the same. Therefore, in the next section the 2-D calculations are done to analyse the experimental data. Note that in eq. (3.38) we declare the approach of approximation. This will cause to miss the precise value of $I(Q)$ calculated. Fortunately, this approximation does not affect the real shape of diffuse scattering.

Figure 3.9 shows a set of powder-diffraction patterns calculated in 2-D as a function of the faulty stacking probability α. The other parameters are chosen to be as follows:

1. The interparticle spacing: $530nm$.

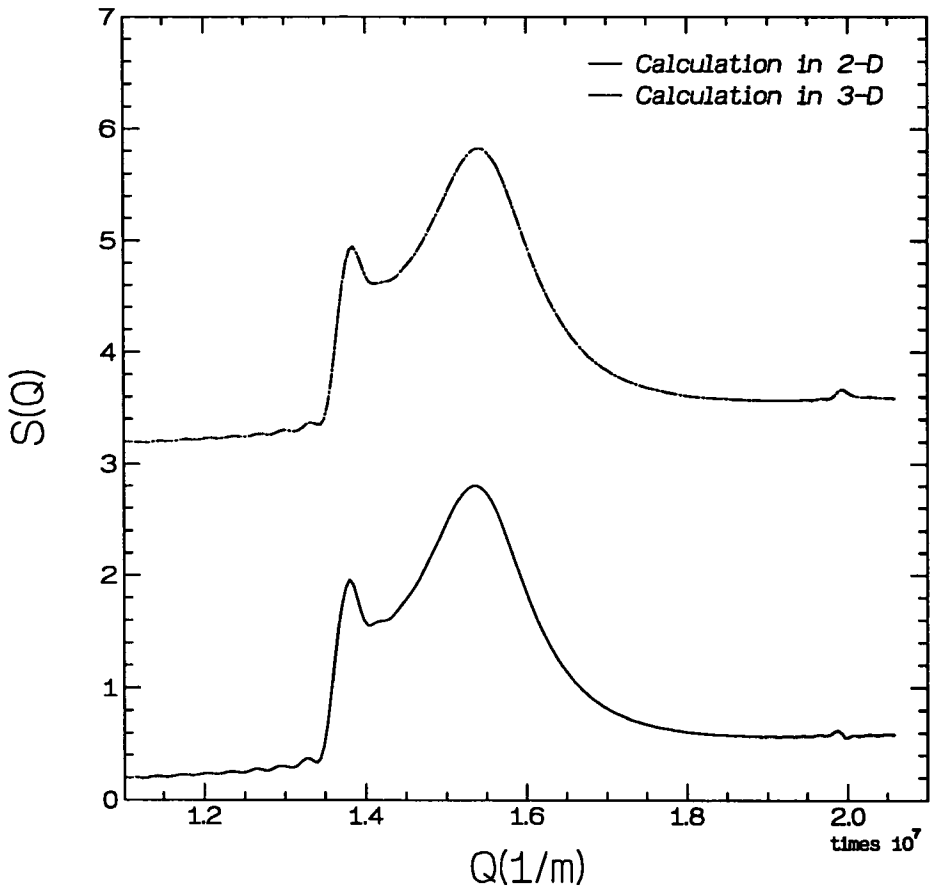

Figure 3.8. The numerical calculations are done in 2-D and in 3-D to check the shape of diffuse scattering in the case of $\alpha = 0.50$. Solid line is the calculation done in 2-D. Dash-dot line is the calculation done in 3-D.

2. The numbers of unit cells in all crystal axes: 45-45-45.

3. The random displacement: $70nm$.

Again, $\alpha = 0$ corresponds to pure *hcp* structure, and $\alpha = 1$ corresponds to pure *fcc* structure. All the calculated patterns shown in figure 3.9 were displaced a constant value, then one can clearly differentiate the differences between them. Note the peak broadening as α is varied between 0 and 1. For the diffraction pattern by perfect *hcp* structure ($\alpha = 0$), the peaks shown in figure 3.9 can be labelled as (100), (001), $(10\frac{1}{2})$, and (101) by reference to figure 3.6 [or conventional (100), (002), (101), and (102)] in

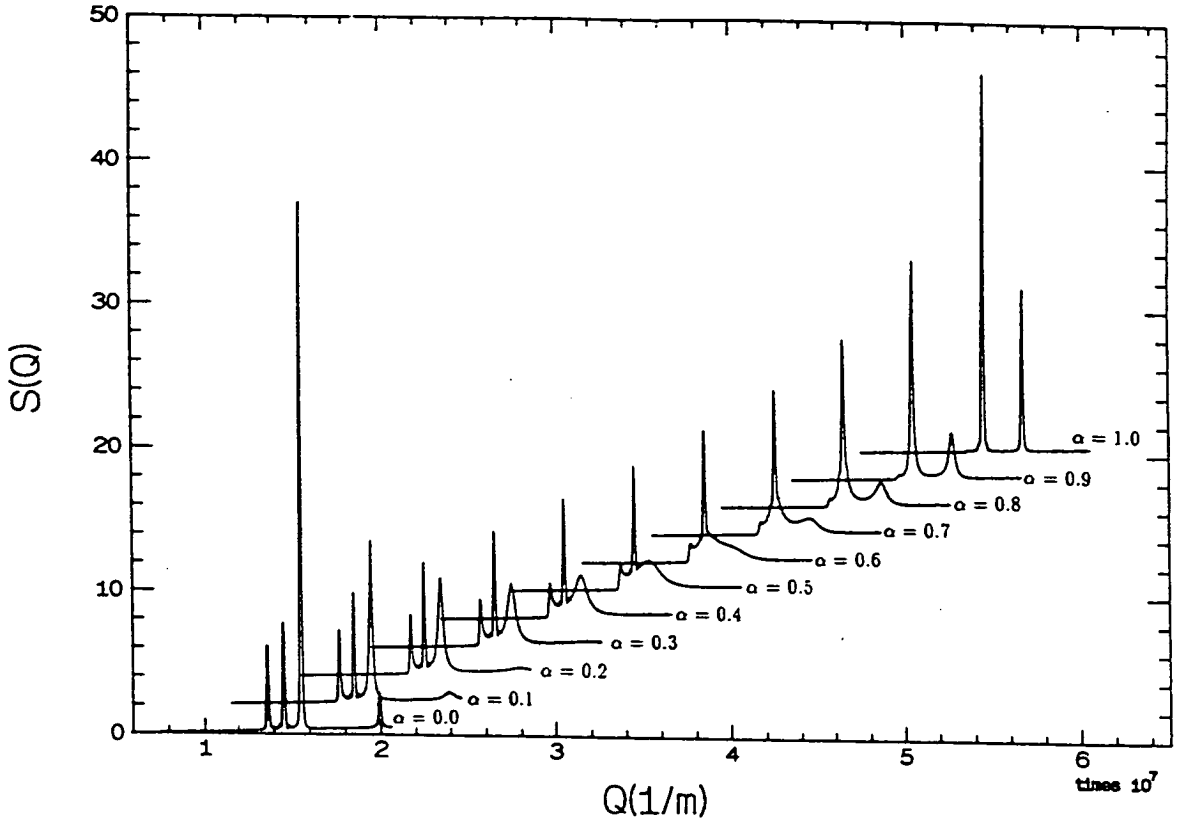

Figure 3.9. The powder-diffraction patterns are calculated in 2-D as a function of the faulty stacking probability α.

turn from left to right. Here one has to notice that the (100), $(10\frac{1}{2})$ and (101) [or conventional (100), (101) and (102)] reflection gradually disappear as α increases. This is so because the scattering intensity of (100) and (101) nodes drops down to zero and the one of $(10\frac{1}{2})$ node splits towards $(10\frac{1}{3})$ and $(10\frac{2}{3})$ as α increases (refer to figure 3.4). As a result, a new peak [$(10\frac{2}{3})$ reflection] which corresponds to $(200)_{fcc}$ reflection appears and $(111)_{fcc}$ reflection is contributed by both $(10\frac{1}{3})$ and (001) nodes. One also has to keep in mind that contributions to the real-space powder intensity are associated with the product of the intersection area of the Q-sphere with a feature in reciprocal space and the intensity of the feature [refer to figure 3.6 and equation (3.37)].

3.4 Experimental

3.4.1 Experimental background and arrangement

In reference [7] detailed experimental observation showed that an amorphous colloidal fluid starts to crystallise at freezing concentration, $\phi_F = 0.494$ and that colloidal crystals begin to melt at melting concentration, $\phi_M = 0.545$. For $\phi_F < \phi_E < \phi_M$, the equilibrium state is a coexistence of fluid ($\phi_E = 0.494$) and crystal ($\phi_E = 0.545$), and phase separated by a visible boundary due to gravitational settling of the crystallites. For $\phi_E > \phi_M$, fully small compact crystallites can be observed. If $\phi_E > 0.58$, amorphous or glassy phases and partially heterogeneous crystallisation region will appear (here ϕ_E represents the effective colloid volume fraction discussed in section 1.4). All the crystallites in the sample are orientationally random. Therefore, the light scattering experiment is designed to be analogous to powder diffraction crystallography [65].

Our high concentrated samples were made by weighing the stock solution (colloidal particles suspended in cis-decalin with $\phi_E \simeq 0.3$) in sample cells and centrifuging the particles down, then we removed weighed supernatant part (assume to be pure cis-decalin) and added an appropriate amount of weighed tetralin chosen to have the volume ratio of tetralin to solvent (cis-decalin + tetralin) about 30%. The near index-matched samples then can be obtained. We calculated the volume fraction of samples by weight and observed the phase behaviour of samples to measure the volume percentage of crystallites in sample cells. By reference to the phase diagram shown in figure 1.4 the effective colloid volume fraction can be calibrated (only suitable for samples showing a coexistence of fluid and crystal). For samples with full crystallites, the calculated concentrations by weight could not be calibrated. However, the concentrations are empirically estimated to have error of ± 0.003 by colloid volume fraction.

To study the polycrystalline phase, an expanded Kr^+-ion laser was passed through the $1 \times 1cm^2$ cross section sample cell. The square cell was immersed in a liquid bath in

which the refractive index of the liquid in the bath is closely matched to the approximately index-matched sample. Therefore, the parallel scattered light can be focused by the cylindrical bath which acts as a focus lens. A slit was placed around the focus point to effectively obstacle the unwanted scattered light. Behind the slit is the diffuser (a tracing paper) which acts to "average" the received scattered light. The detection optics was mounted on a computer-controlled arm which rotated through the operation of the step controller. Scans over scattering angle span from 40° to 90° in steps of 0.2°, taking about 10min. The block diagram of static laser light scattering instrument is shown in figure 3.10.

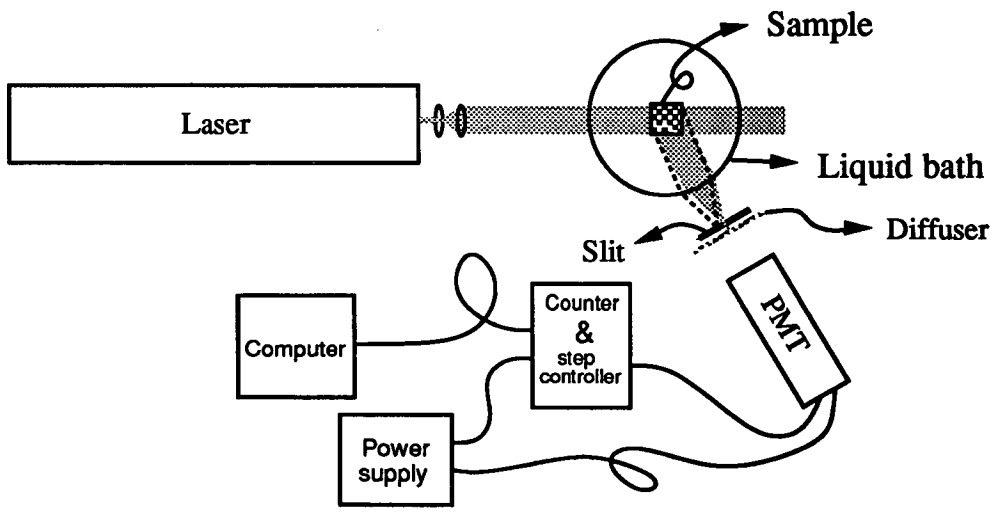

Figure 3.10. The block diagram of static laser light scattering equipment

For simplicity we assume that the scattering materials inside the particles are homogeneous and that the particles satisfy the Rayleigh-Debye condition (refer to chapter 2). Therefore, for monodisperse particles the scattering intensity $I(Q)$ can be written to give

$$I(Q) \propto P(Q)S(Q), \tag{3.39}$$

where Q is the scattering vector, $P(Q)$ is the single-particle form factor which can be determined by measurements of $I(Q)$ on dilute suspensions [for which $S(Q) = 1$], and $S(Q)$ is the structure factor. Structure factors can be obtained by measuring $I(Q)$ for the concentrated suspensions and then dividing by the proper form factors. The resulting structure factors are in arbitrary units because we do not attempt to determine the actual concentrations of the dilute supernatant suspensions. The solid sediment also can be melted by tumbling the sample. The reproducible metastable fluid (if the volume fraction of the sample is higher than the freezing concentration) will recrystallise. After dividing the measured scattered intensity by crystallites in the sample by the measured form factor data, the measured structure factor of the crystal can be obtained.

3.4.2 The structure of near hard-sphere colloidal fluid

The polydispersity of the sample system studied here is estimated to be about 5% by the use of dynamic light scattering shown in chapter 2. In section 3.2.1 we discussed the effect of polydispersity on $S^M(Q)$ and found that a hump at about $Q\bar{R} = 4.9$ can be detected if the hard-sphere colloidal particle is homogeneous and the polydispersity is small. In this experiment the aim is not only to study the structure of colloidal fluid but also to check the distribution of scattering material inside the particle.

A near index-matched sample whose colloid volume fraction is 0.514 was prepared. The mean radius and polydispersity of this sample are $239nm$ and 5%, respectively, by using the technique discussed in chapter 2. According to the procedure mentioned in the previous section, the form factor data and structure factor can be obtained. The results are shown in figure 3.11 and 3.12. In figure 3.12, to fit the experimental data, one considered the empirical correction suggested by Verlet and Weis [66]:

$$\phi' = \phi_E - \phi_E^2/16 \tag{3.40}$$

where ϕ_E is the effective colloid volume fraction. ϕ' is the volume fraction used in the calculation. This is so because the measured structure factor calculated in the Percus-Yevick approximation is overestimated at high particle concentrations.

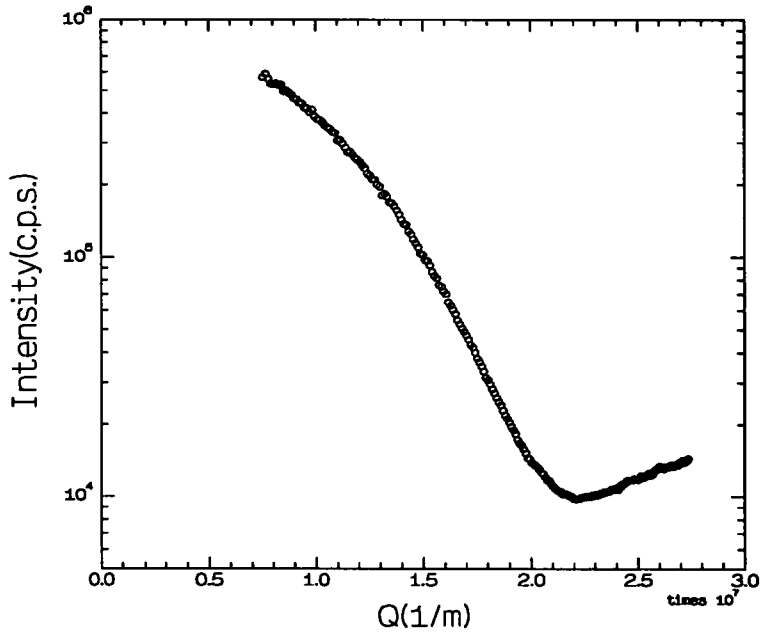

Figure 3.11. The form factor data measured from the extremely dilute supernatant part of the sample after centrifuging down the particles in the cell and then gently shaking the sample cell.

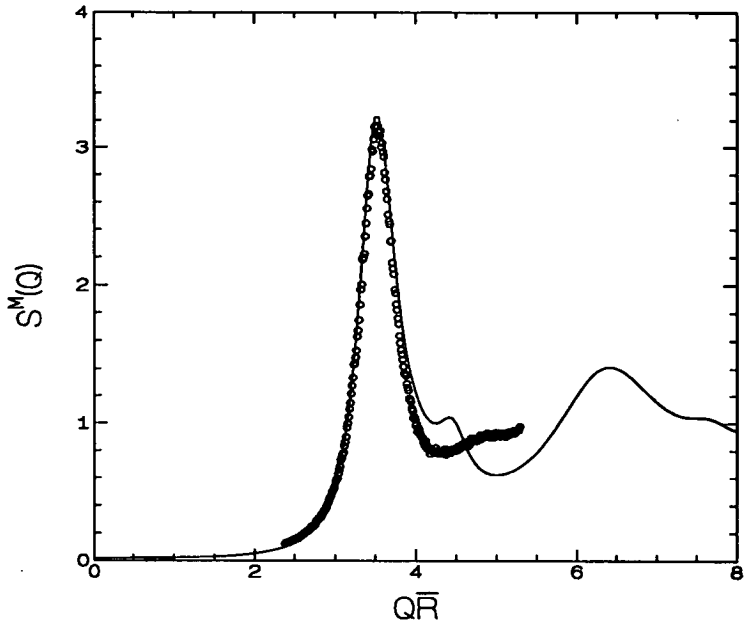

Figure 3.12. The measured structure factor of the metastable fluid with $\phi_E = 0.532$. Solid line is theory with $\phi' = 0.514$.

Unfortunately, the hump predicted by the theory discussed in section 3.2.1 is very close to the minimum of form factor in that the experimental data around the minimum of form factor is not reliable due to the too weak scattering. In addition, multiple scattering also affect the tail of the structure factor. That is the reason why one cannot make a further measurement at high Q. As discussed in chapter 1, our sample system consists of the hard-sphere PMMA "core" coated with PHSA "shell". Strictly speaking, the "shell" could scatter light. This will lead to a complicated scattering condition that the scattering material inside the "core" is different from that inside the "shell".

3.4.3 The structure of near hard-sphere colloidal crystals

To characterise the structure of near hard-sphere colloidal crystals, one has to work out the theory discussed in section 3.3.2. The theory indicates that the shape of diffuse scattering is quite sensitive to faulty stacking probability α. Therefore, we thought of the feasibility of making a comprehensive measurement to study the correlation between α and ϕ, colloid volume fraction, in which the correlation was first briefly uncovered by Pusey *et al.* [65] although they only studied 2 samples with different concentrations.

In this experiment, the sample C set is prepared (range of sample concentrations span from 0.506 to 0.568) and the PMMA particles are investigated to have mean radius about $239nm$ and polydispersity (standard deviation of the particle size distribution divided by the mean size) of $\lesssim 5\%$, characterised by dynamic laser light scattering [18] (or see chapter 2). The measurements were made at the early stage of crystallisation of colloidal suspensions (if the rate of crystallisation is slow, then there is no choice that one has to wait several hours or days for crystallites to form and to settle, such as sample C1 and C2 shown in table 3.3). To smooth the data, it is necessary to do at least two runs by rotating the sample cell between runs. The results of a series of measurement are shown from figure 3.13 to 3.20, and these data were fitted to the theory discussed in section 3.3.2.

To fit the experimental data to the theory, we have to refer to figure 3.9. From the shape of diffuse scattering measured we can estimate the possible interval of α first, and from the position of the $(001)_{hcp}$ reflection detected we can calculate the mean interparticle spacing by reference to eq. (3.36). Then, we also need to adjust the proportionality constant to make the shape of the measured structure factor coincide with the theory selected as closely as possible. Afterwards, the most likely value of α can be decided. Note that the accurate size of crystallite is impossible to be measured because the polycrystalline phase obtained is polydisperse. However, by sending white

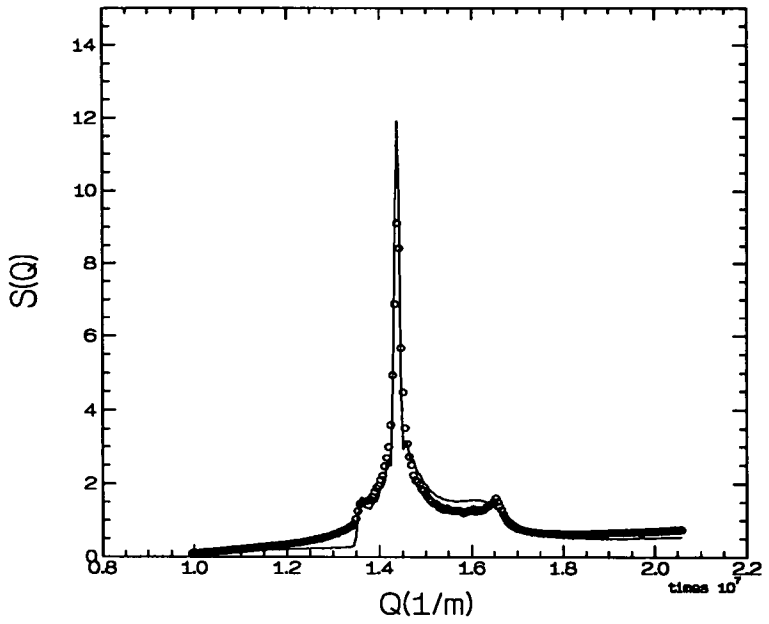

Figure 3.13. o: experimental data of ϕ=0.506 measured 3 days after shear-melting, solid line is theoretical curve. The faulty stacking probability α=0.65.

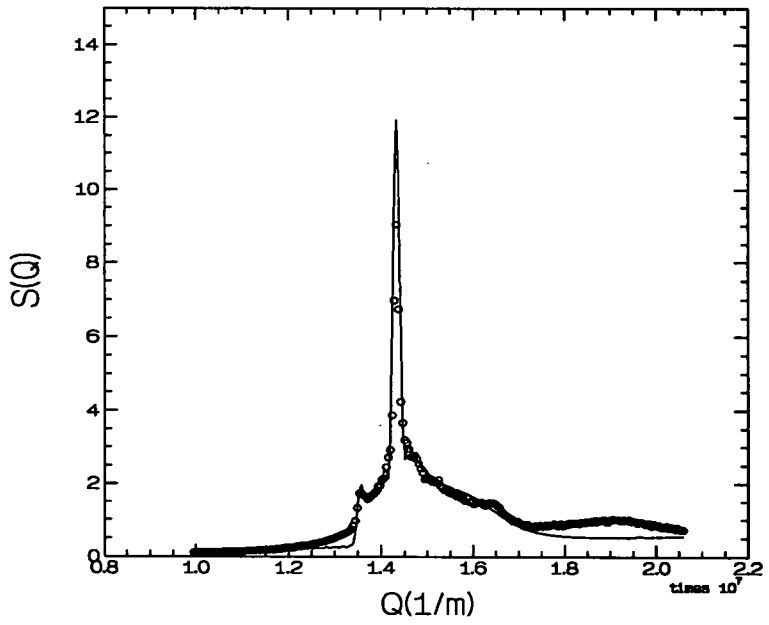

Figure 3.14. o: experimental data of ϕ=0.521 measured about 24 hours after shear-melting, solid line is theoretical curve. The faulty stacking probability α=0.60.

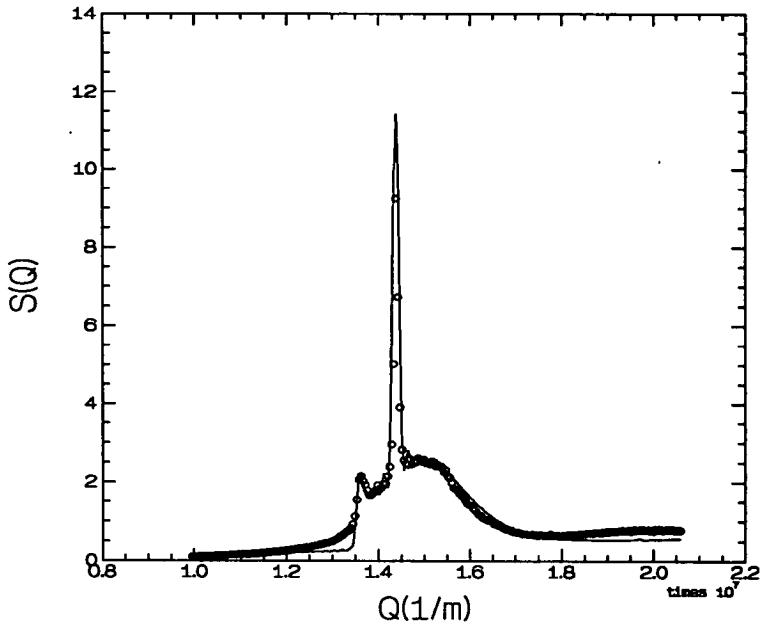

Figure 3.15. o: experimental data of ϕ=0.532 measured 4 hours after shear-melting, solid line is theoretical curve. The faulty stacking probability α=0.55.

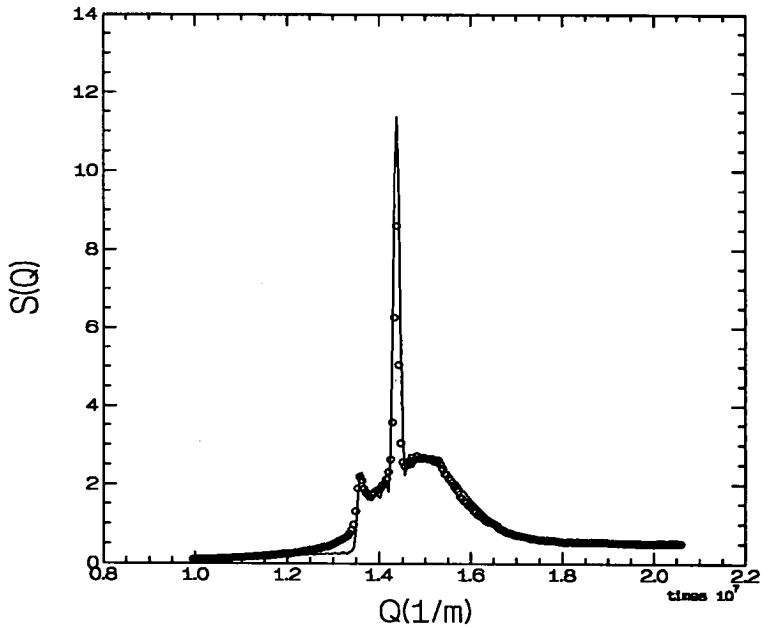

Figure 3.16. o: experimental data of ϕ=0.538 measured 4 hours after shear-melting, solid line is theoretical curve. The faulty stacking probability α=0.54.

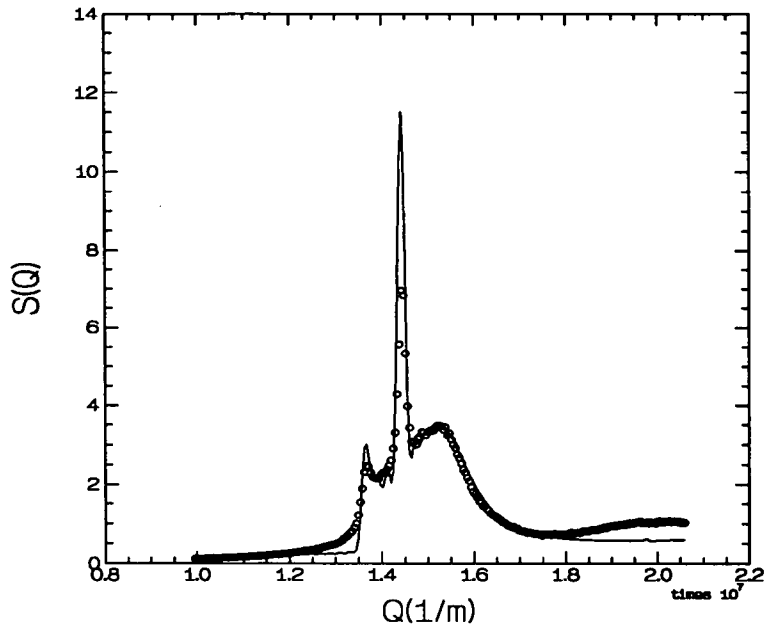

Figure 3.17. o: experimental data of ϕ=0.548 measured 1 hour after shear-melting, solid line is theoretical curve. The faulty stacking probability α=0.51.

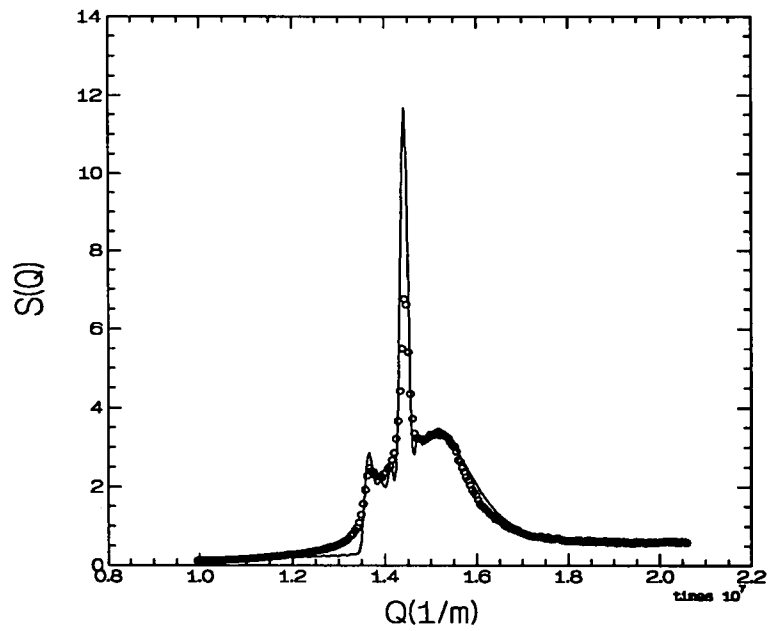

Figure 3.18. o: experimental data of ϕ=0.551 measured 1 hour after shear-melting, solid line is theoretical curve. The faulty stacking probability α=0.53.

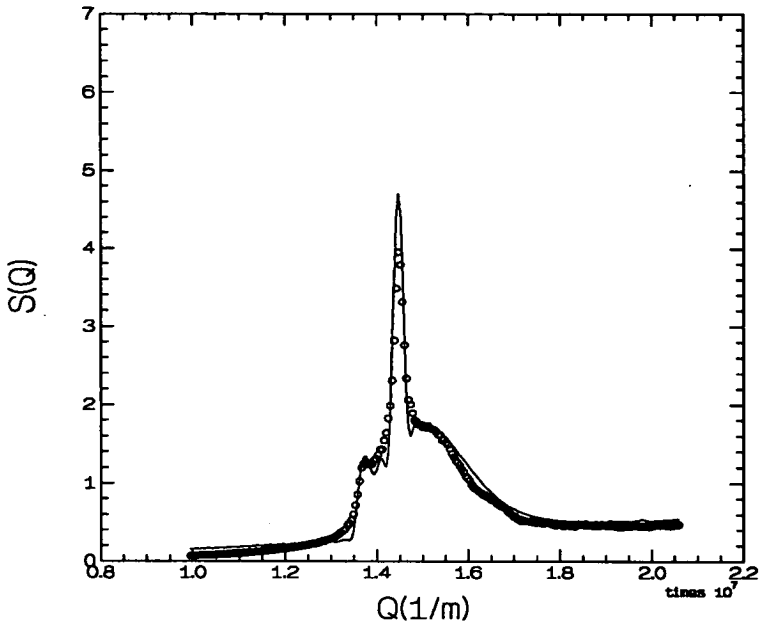

Figure 3.19. o: experimental data of ϕ=0.555 measured 2 hours after shear-melting, solid line is theoretical curve. The faulty stacking probability α=0.55.

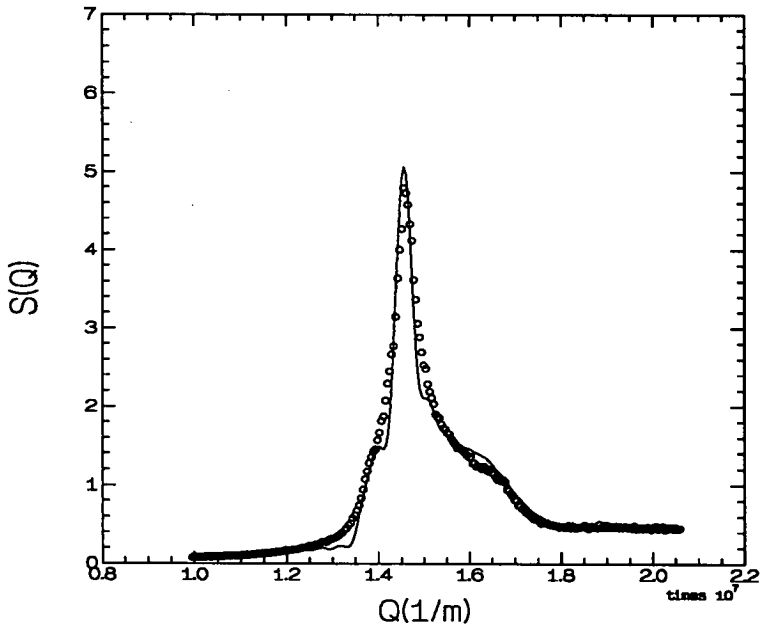

Figure 3.20. o: experimental data of ϕ=0.560 measured 3 hours after shear-melting, solid line is theoretical curve. The faulty stacking probability α=0.62.

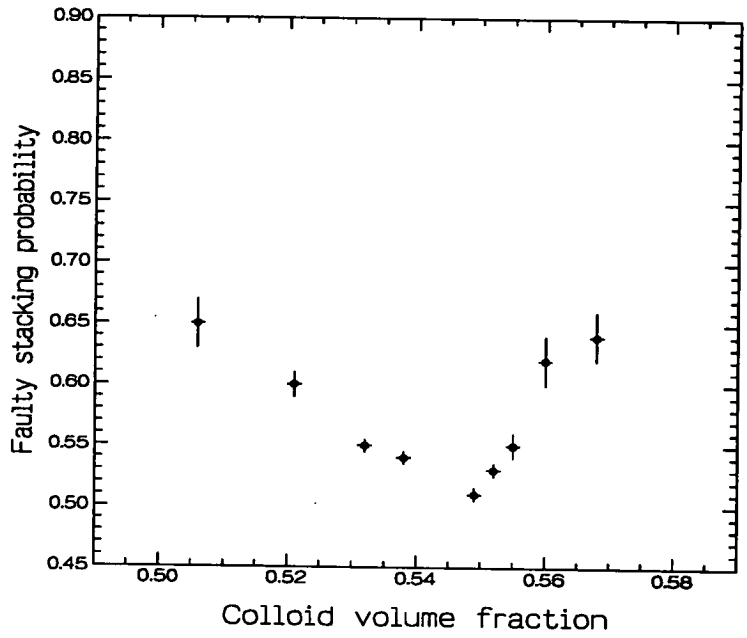

Figure 3.21. The faulty stacking probability α is found to be a function of ϕ. See text for explanation.

light to pass through the polycrystalline phase and then using microscope to video the crystallites the mean size of the crystallites can be estimated. In figure 3.19 and 3.20, the effect of size broadening of the $(001)_{hcp}$ reflection is quite obvious.

Figure 3.21 shows that at near melting point the structure of a near hard-sphere colloidal crystal is almost completely random, that is, $\alpha = 0.51 \pm 0.005$. Away from the melting point shows that the structure of colloidal crystals changes towards fcc whose α is 1 although the change is not very big. In table 3.3 we summarise the data and the adjustable parameters used in the theory. The parameter of random displacement of the particle was chosen to be $70nm$, which is about 13% of the mean interparticle spacing suggested by Young and Alder [64], in all the fitting curves. All these measurements were made at the same temperature, 22^oC. For sample C1, only about 20% of polycrystalline phase forms in the suspensions, taking about 3 days. Therefore, the number density of crystallites suitable for crystallography is decreased and makes the

Sample information			Adjustable parameters		
Sample	"Age"	$\phi \pm 0.003$	α	$n_1 - n_2 - n_3$	$d(nm)$
C1	3 days	0.506	0.650±0.020	55-55-50	535.2
C2	24 hours	0.521	0.600±0.010	45-45-40	535.2
C3	4 hours	0.532	0.550±0.005	45-45-40	535.2
C4	4 hours	0.538	0.540±0.005	45-45-40	535.2
C5	1 hour	0.548	0.510±0.005	40-40-35	533.6
C6	1 hour	0.551	0.530±0.005	40-40-35	533.6
C7	2 hours	0.555	0.550±0.010	27-27-25	531.9
C8	3 hours	0.560	0.620±0.020	18-18-18	528.7
C9	3 hours	0.568	0.640±0.020	—	525.5

Table 3.3. "Age" means the time elapsed after shear-melting the sample before the measurement is made. d represents the interparticle spacing. The adjustable parameters are discussed in section 3.3.4. See text for further details.

scattered pattern noisy. However, we did several runs by rotating the sample cell between runs and averaged the data to reduce the noise. The big error bar comes from the conjecture that in figure 3.13 the small peak at $Q \simeq 1.65 \times 10^7 m^{-1}$, known to be (200) reflection of *fcc* structure, interfered with the quantitative analysis. Normally, this unusual (200) reflection of *fcc* structure causes to overestimate the faulty stacking probability. This point will be discussed more in detail in the next section. For sample C8 and C9, the average size of the crystallites is too small. Therefore, the effect of size broadening [41] also interfered with the quantitative analysis. Note the faulty stacking probability of sample C9 claimed in table 3.3 is not obtained by fitting the data to the theory but evaluated by reference to the result of the second-stage measurement discussed in the next section.

3.4.4 Long-time observation of the structure of colloidal crystals

In section 3.4.3 we mentioned the unusual (200) reflection of *fcc* structure observed in sample C1. By examining the data shown in the previous section, we found that if the measurement is made within several hours after shear-melting the sample, there will be no (200) reflection, or at least it is too weak to be detected. The (200) reflection

used here to describe the unusual peak probably is not a correct description because in section 3.3.2 we discuss the peak shift due to stacking faults. Through numerical calculation we found that the shift of $(200)_{fcc}$ reflection is very small if α varied between 0.9 and 1. Unfortunately, this extremely small shift can not be differentiated due to the limit of the experimental resolution. Thus, we postulate that it is not necessary for the "unknown" structure to be a perfect *fcc*. However, we estimate that the α of this "unknown" structure must be larger than 0.85 by reference to the numerical calculation. This will be discussed more in detail in the next section. At the moment just let us call this unusual peak (200) reflection.

We designed an experiment to study whether the structure of near hard-sphere colloidal crystals will rearrange with time or not. We also would like to understand what the role of the "unknown" structure plays in the system. Sample R3 was made to be approximately index-matched, and the colloid volume fraction is 0.542. The average size of PMMA particles studied is estimated to be $228\pm5nm$ by the technique of DLS discussed in chapter 2, and the polydispersity found to be 5%. The first measurement was made one hour after shear-melting the sample, and then the sample was left undisturbed. The faulty stacking probability α is found to be 0.52 shown in figure 3.22 that the result is quite consistent with the measurement in the previous section. The second measurement was made about 18 hours after shear-melting, and the small hump at about the position of (200) reflection can be clearly detected, as shown in figure 3.23. Afterwards, we made a measurement every day. We found the hump grew up, the shape of diffuse scattering also changed, and the intensity of regular (001) reflection of *hcp* structure [or (111) reflection of *fcc* structure (See section 3.3.2.)] increased. Figure 3.24 shows the data measured 7 days after shear-melting in that the shape of diffuse scattering is quite consistent with the theory with $\alpha = 0.57$. Obviously, the theory does not predict the unusual (200) reflection. After going back to check the theory discussed in section 3.3.2, we can point out that the theory assumes the stacking faults are evenly

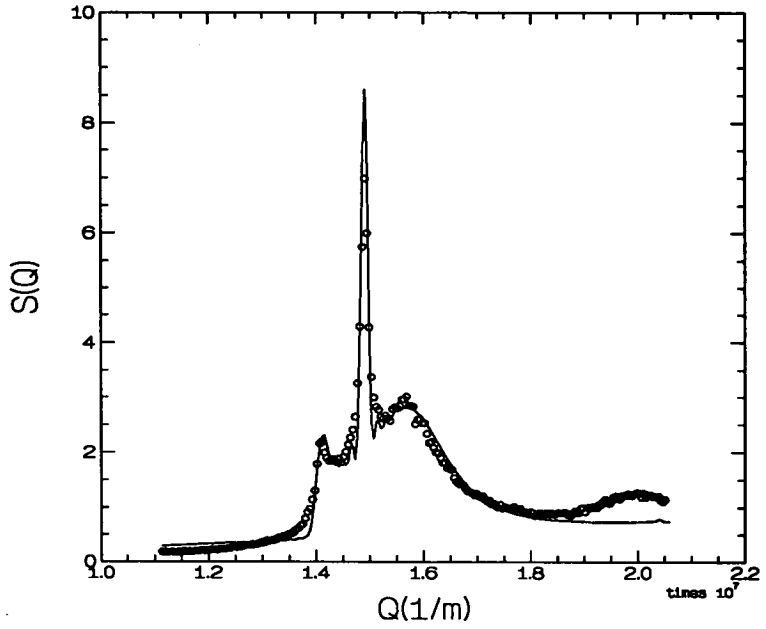

Figure 3.22. o: experimental data of R3 with $\phi = 0.542$ measured one hour after shear-melting, solid line is theoretical curve. The faulty stacking probability α=0.52. See text for details.

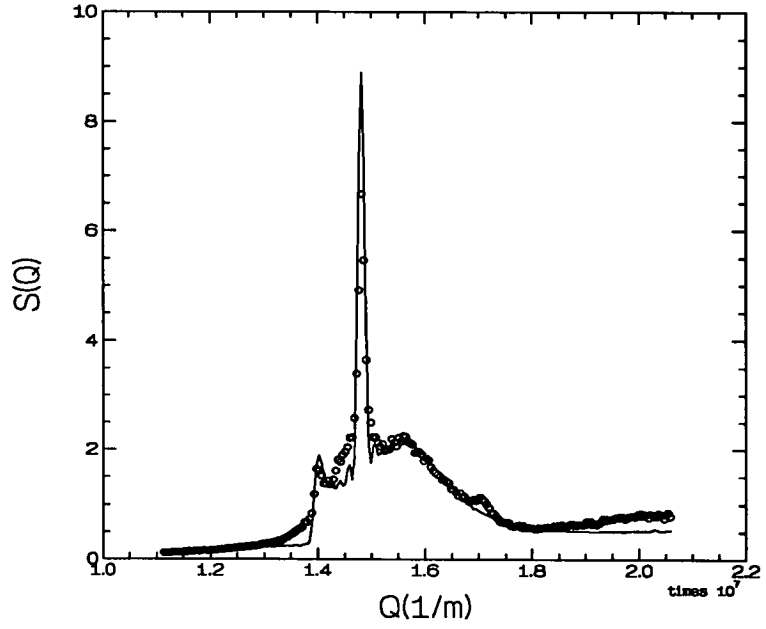

Figure 3.23. o: experimental data of R3 measured 18 hours after shear-melting, solid line is theoretical curve. The faulty stacking probability α=0.53. See text for details.

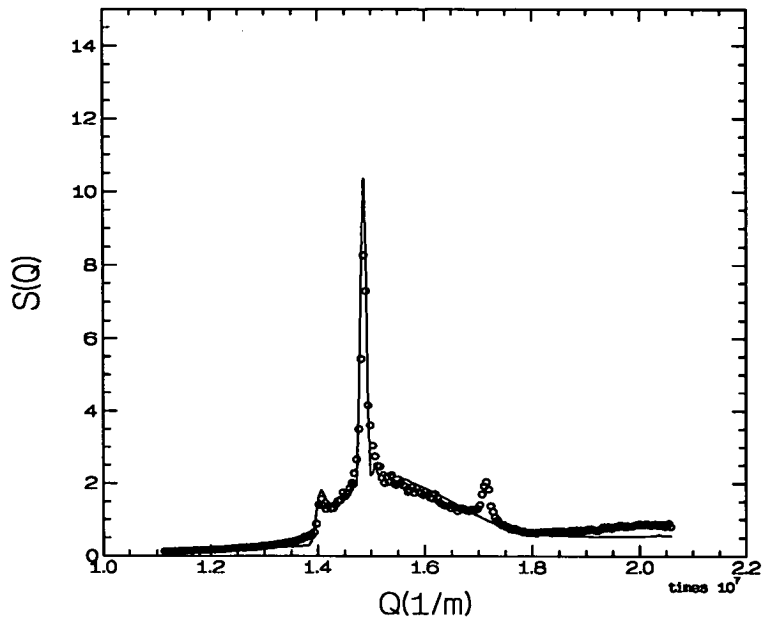

Figure 3.24. o: experimental data of R3 measured 7 days after shear-melting, solid line is theoretical curve. The faulty stacking probability α=0.57. See text for details.

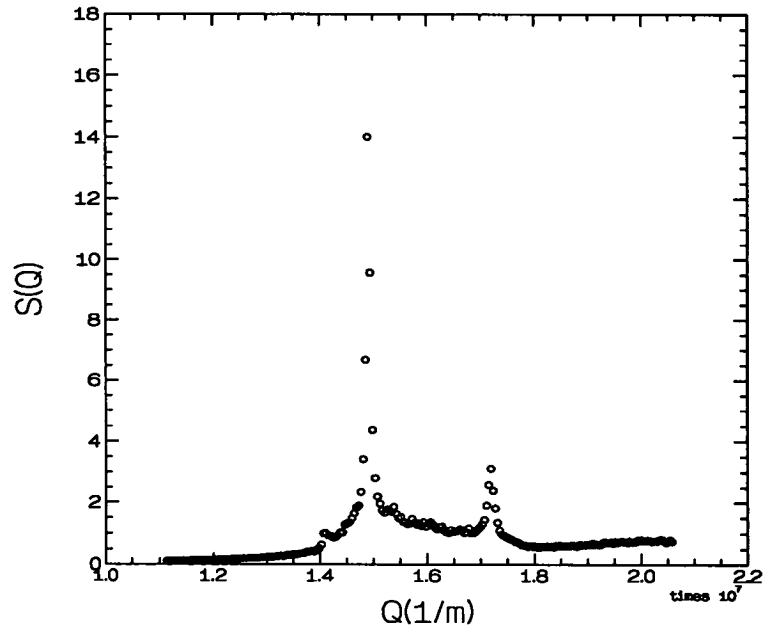

Figure 3.25. o: experimental data of R3 measured about 22 days after shear-melting.

distributed in the crystal and then the recursion relation shown in eq. (3.10) can be solved by considering the boundary conditions. The more surprising result is shown in figure 3.25 when the measurement was made about 22 days later. Although the diffuse scattering dropped down, it still clearly exists there. To explain this phenomenon, we have to propose a new model and to improve the theory. In the next section there is a detailed discussion about this point.

The other sample studied is C9 whose colloid volume fraction is 0.568. The data shown in figure 3.26 was measured 3 hours after shear-melting. Again, the effect of size broadening interfered with the quantitative analysis. Basically, this scattered pattern is quite similar to the one shown in figure 3.20. Here one did not fit the data. Figure 3.27 shows that the average size of crystallites of sample C9 increases in comparison with figure 3.26. This phenomenon indicates that there exists a size distribution of crystals because the growth of one part of the crystallites of sample C9 must be at the

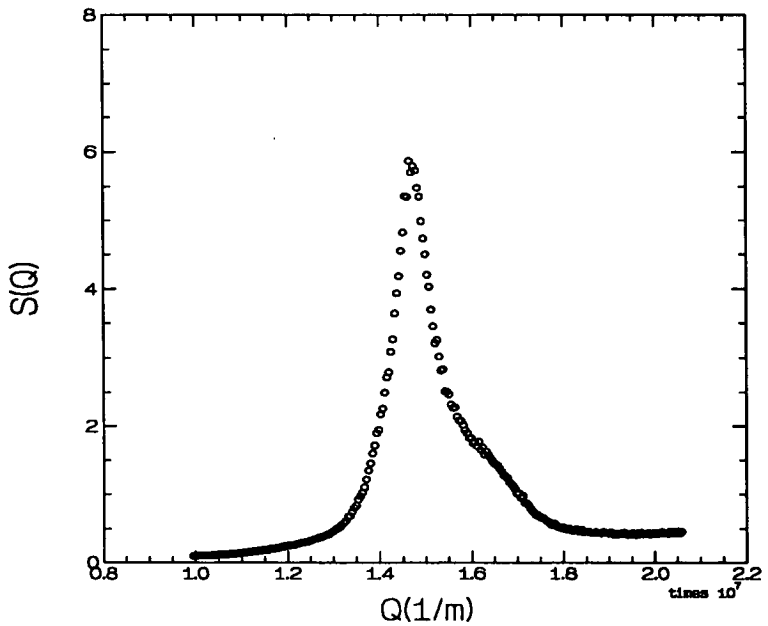

Figure 3.26. o: experimental data of C9 measured 3 hours after shear-melting.

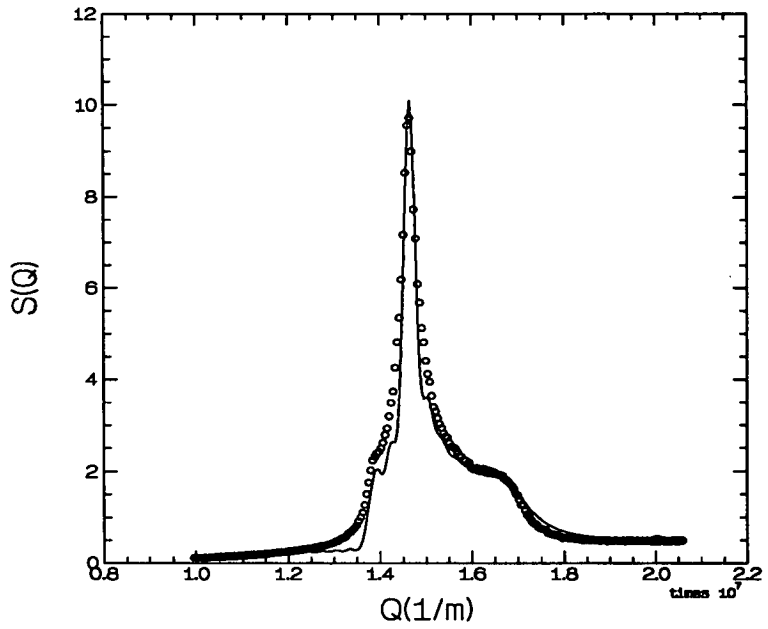

Figure 3.27. o: experimental data of C9 measured about 3 days after shear-melting. Solid line is theory with $\alpha = 0.64$.

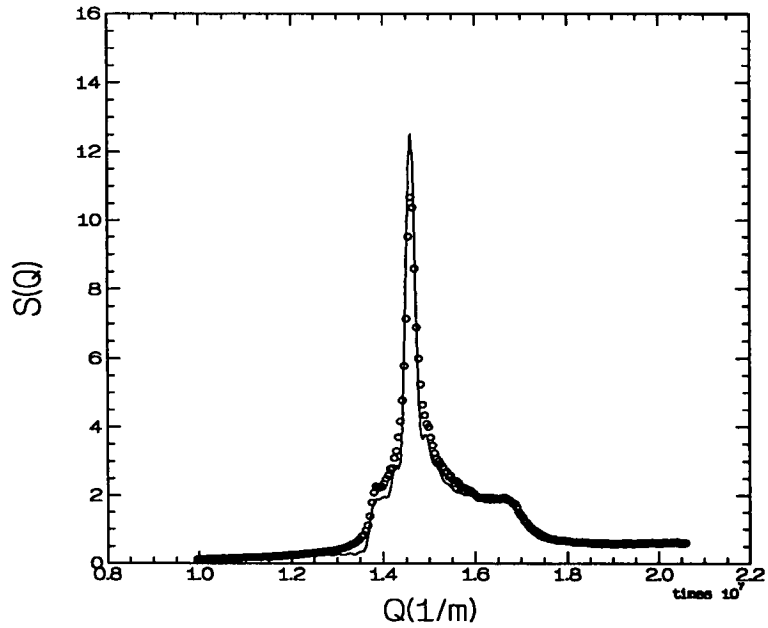

Figure 3.28. o: experimental data of C9 measured about 8 days after shear-melting. Solid line is theory with $\alpha = 0.65$.

expense of the other part of the crystallites. The small change can be found in figure 3.28. However, the crystal growth rate of sample C9 is much slower than that of sample R3.

3.4.5 The proposed new model and improved theory

The phenomenon that the growth of the bigger crystals is at the expense of the smaller ones can be explained by the theory, known as "Ostwald ripening" which can be dated back to the work by Gibbs [67]. The theory mainly described that "any system is unstable in the thermodynamic sense until its free energy has reached a minimum. Therefore a two-phase system consisting of a polydisperse precipitate within a parent phase is not stable, since the large interfacial area is a source of free energy and further stabilisation may be reached by decreasing this area" [67]. One might think about the process of crystallisation that once the small crystallites (nuclei) form all the crystallites start growing up with slightly different growth rate due to inevitable concentration fluctuation of the sample system. There also exists a critical radius of crystal which is an increasing function of time in the sample system [67]. The ripening process happens when the size of the smaller crystals is caught up by the critical radius. We surmise that the growth rate of the bigger crystals after ripening probably is different from that before ripening.

If the growth rate of a crystal is associated with the structure of the close-packed random-stacked crystal, one can surmise that each growth rate corresponds to a specific faulty stacking probability. Here one postulates, very roughly, that there exist two steps of growth of crystals. The first step of growth of a crystal corresponds to the inner layers of a crystal whose faulty stacking probability is α_1, and the second step of growth corresponds to the outer layers whose faulty stacking probability is α_2, as shown in figure 3.29. To deal with this structure, let us recall eq. (3.18) and concentrate on

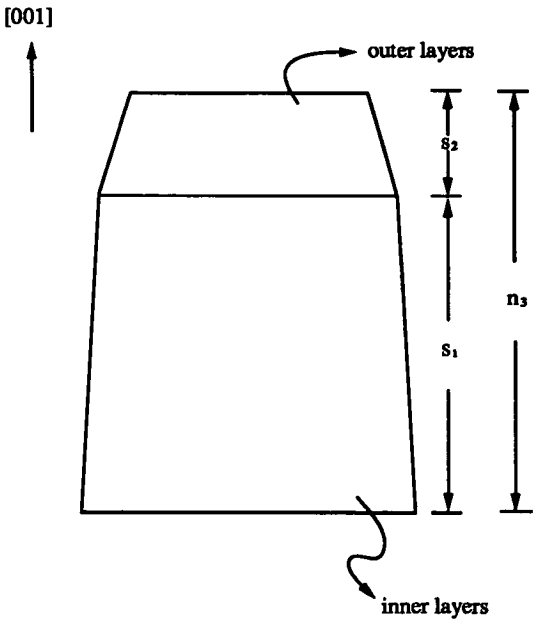

Figure 3.29. The new model is used to interpret the unusual (200) reflection found in the previous section. The inner layers are associated with the first step of growth of the crystal, and the outer layers are associated with the second step of growth. See text for details.

the double sum:

$$\sum_{j=1}^{n_3}\sum_{m_3=1}^{n_3} F_j F_{m_3}^* e^{i(j-m_3)\mathbf{Q}\cdot\mathbf{c}} = \left[\sum_{j=1}^{s_1} F_j e^{ij\mathbf{Q}\cdot\mathbf{c}} + \sum_{j=s_1+1}^{n_3} F_j e^{ij\mathbf{Q}\cdot\mathbf{c}}\right] \times \left[\sum_{m_3=1}^{s_1} F_{m_3}^* e^{-im_3\mathbf{Q}\cdot\mathbf{c}} + \sum_{m_3=s_1+1}^{n_3} F_{m_3}^* e^{-im_3\mathbf{Q}\cdot\mathbf{c}}\right] \tag{3.41}$$

Note that sum$(1 \rightarrow n_3)$ =sum$(1 \rightarrow s_1)$ + sum$[(s_1+1) \rightarrow n_3]$. The question turns out to be clear that the "cross term" obtained from eq. (3.41) has to be evaluated. The "cross term" reflects the interference between inner and outer layers, that is,

$$2\mathrm{Re}\sum_{j=1}^{s_1}\sum_{m_3=s_1+1}^{n_3} F_j F_{m_3}^* e^{i(j-m_3)\mathbf{Q}\cdot\mathbf{c}} \tag{3.42}$$

Therefore, the aim is to evaluate $F_j F^*_{m_3}$ which represents the interference between two scattering amplitudes by the unit cells located in different sorts of structure, as shown in figure 3.29. If one can visualise that the two different sorts of structure, α_1 and α_2, are disconnected, then F_j and F_{m_3} are completely uncorrelated. This can lead to a simple result that $F_j F^*_{m_3} = 0$. However, they are in the same crystal, just occupying different part of the crystal with the same orientation although they are seemed to be uncorrelated to each other. To check the product of F_j and $F^*_{m_3}$, let us consider an infinitely big crystal with stacking faults. Recall eq. (3.17) that is

$$F_j F^*_{j+m} = f^2 \left[\frac{1+2K}{3} + (1-K)\left(Q_e {\rho_e}^m + Q_o {\rho_o}^m\right) \right]$$

Basically, this equation indicates the correlation between any two (001) layers of a close-packed random-stacked crystal, separated by a distance mc. If the separated distance $mc \to \infty$, there will be no correlation between the two layers unlike a perfect-periodic crystal that the correlation still exists even in such a condition. Therefore, one attempts the approach:

$$\lim_{|m| \to \infty} F_j F^*_{j+m} = f^2 \left(\frac{1+2K}{3} \right) \tag{3.43}$$

under the consideration that α is not equal to 0 or 1. This result implies that the contribution to diffuse scattering by the interference of two layers separated by a long distance is approximately nil. However, they still normally contribute to the dot on the hkl rows whose value of $(h-k)/3$ is integral in the reciprocal space of *hcp* structure. This conclusion offers an idea to deal with eq. (3.42):

$$F_j F^*_{m_3} = \lim_{|m| \to \infty} F_j F^*_{j+m} = f^2 \left(\frac{1+2K}{3} \right) \tag{3.44}$$

because in a random-stacked crystal the interference by two mutually "lost-correlation" layers does not contribute to diffuse scattering but to the dot mentioned above. Thus,

one can write

$$\sum_{j=1}^{n_3}\sum_{m_3=1}^{n_3} F_j F_{m_3}^* e^{i(j-m_3)\mathbf{Q}\cdot\mathbf{c}} = \sum_{j=1}^{s_1}\sum_{m_3=1}^{s_1} F_j F_{m_3}^* e^{i(j-m_3)\mathbf{Q}\cdot\mathbf{c}} +$$
$$\sum_{j=s_1+1}^{n_3}\sum_{m_3=s_1+1}^{n_3} F_j F_{m_3}^* e^{i(j-m_3)\mathbf{Q}\cdot\mathbf{c}} + 2\left(\frac{1+2K}{3}\right)\sum_{j=1}^{s_1}\sum_{m_3=s_1+1}^{n_3} e^{i(j-m_3)\mathbf{Q}\cdot\mathbf{c}} \qquad (3.45)$$

In eq. (3.45) on the right-hand side the first double summation term characterises the structure of inner layers, the second one characterises the structure of outer layers, and the third one ascertains that the two different sorts of close-packed structure are attached to construct a whole crystal, as shown in figure 3.29.

3.5 Discussion

To explain the curve shown in figure 3.21, two strategies are adopted. One is to check the free energy differences between *fcc* and *hcp* structure. The other is to study the kinetics of crystallisation. As discussed in section 3.2.4, some computer simulations and numerical calculations indicate that the difference in free energies between *fcc* and *hcp* structures is extremely small. Generally speaking, the range of the faulty stacking probability can be measured from colloidal crystals spans from 0.5 to 0.7 which show high degree of randomness. This point supports the conclusions of those authors. If there is no external effect on the crystallisation of near hard-sphere colloidal suspensions, probably, this result implies that *fcc* structure is slightly more stable than *hcp* that this argument was proposed by Iglói [46] in 1986 via density functional theory.

To understand the curve shown in figure 3.21, we also studied colloidal crystal nucleation rate, as shown in figure 3.30. The experiment set-up is presented in figure 3.10 and is designed to make a continuous measurement back-and-forth around (001) reflection (or called (111) reflection of *fcc*) to monitor the peak. Initially, there only shows the peak of metastable fluid. Gradually, once the nuclei form in the illuminating

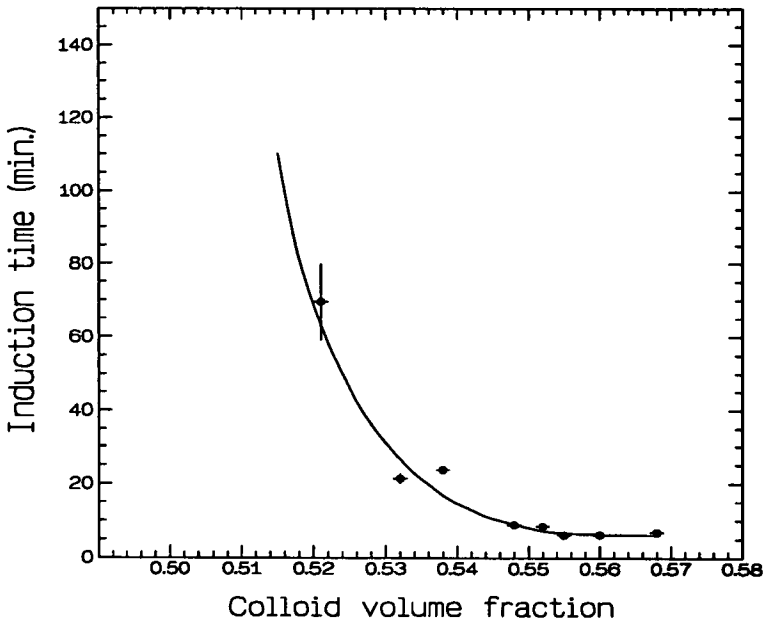

Figure 3.30. The nucleation induction time of colloidal crystals as a function of ϕ. Solid line is the best fit by eye.

region of the sample studied in the experiment, the small Bragg peak can be detected. We checked the intensity of the small Bragg peak which is about 5% higher than that of the background (liquid peak) and then recorded the time elapsed for us to find the peak, called induction time, and did several runs to check the reproducibility. The nucleation rate is roughly the inverse induction time. This result is quite consistent with the one obtained by Smits [68]. Again, the big error bar at low colloid volume fraction shown in figure 3.30 comes from the small number density of crystallites because only a fraction of crystals has the orientation suited to crystallography. The colloidal particle studied by Smits is TPM-silica stabilised with γ-methacryloxypropyltrimethoxysilane and slightly charged. Smits also studied the crystal growth rate of the TMP-silica particle. The result shows that at around melting point the crystal growth rate gets the maximum, away from the melting point it will decrease. This phenomenon is quite similar to what we experienced during our experiment discussed in the previous section.

If just concentrating on figure 3.30, intuitively, one might make a conclusion that the higher the nucleation rate, the more random the structure of colloidal crystals. This is so because the particle needs long enough time to find a correct lattice site. If the nuclei form too quickly, the structure of the nuclei will be completely random, say 50% *fcc* and 50% *hcp*. Unfortunately, we are not able to study the structure of nuclei of colloidal crystals because from the scattered pattern we can find that the small reflection by nuclei sits on the peak of the structure factor of metastable fluid shown in figure 3.12 for the sample in fluid-crystal coexisting phase region, or the peak by nuclei is too broad, almost like a peak of metastable fluid for the sample in full crystalline region. The diffuse scattering which is what we care about can not be detected at that moment. This makes us be not able to study the structure of nuclei of colloidal crystals. Therefore, the measurements made in section 3.4.3 are not related to colloidal crystal nucleation rate.

Colloidal crystal growth rate probably offers more information about the stacking faults of colloidal crystals. Again, as mentioned in section 3.4.4, the growth of the bigger crystals is at the expense of the smaller ones. Owing to inevitable statistical fluctuations, there is no necessity for the crystallites in our samples to be the same size. Thus, Ostwald ripening happens to the process of crystallisation of colloidal crystals. By observing sample C9 studied in section 3.4.4, the result supports this argument. As a result, in a light scattering experiment the scattered pattern is the contribution by polydisperse crystallites. This enhances the difficulty on studying colloidal crystal growth rate.

The model of layer-by-layer growth of a crystal [69] offers one approach for us to understand the phenomenon of stacking faults. As discussed before, the faulty layers only happen to (001) plane. If the speed for particles to join the first few layers is the same, then it can be understood that stacking faults will be evenly distributed in the

structure. If the speed for particles to join the outer layers changes for some reason, say it becomes slower, one might believe that the structure of outer layers obeys the other rule, P_m, to construct the sequence. In the previous section we postulated this problem and offered one of the possible solutions to deal with this complex structure.

The colloidal particles studied here are also big enough to be observed by microscope. Thermal vibrations of the particles can be clearly viewed. Rigorously speaking, the random thermal vibration of the particles is not independent. By comparing all the scattered patterns from PMMA colloidal crystals with the theory, the common point is that at low Q around the "prepeak" there exists a disagreement between experiment and theory. To interpret this difference, we check the model built by reference to Wilson's theory and adopting Einstein model. Because the shape of diffuse scattering described by the theory is very consistent with what we found in light scattering experiments, there is little doubt that the theory is correct. Does the polydispersity of the sample system cause this result? We refer to section 3.3.1 and 3.4.2 and conclude that the region which is most sensitive to polydispersity is around the first minimum of form factor. As a result, the region, from $Q \sim 2.0 \times 10^7 m^{-1}$ to $2.5 \times 10^7 m^{-1}$ in our cases, usually can not show a good scattered pattern due to too weak scattering intensity of form factor and multiple scattering. Figure 3.12 supports this point. Therefore, the most possible answer to the disagreement between experiment and theory at low Q should be that the model of independent oscillator (Einstein model) used here is not correct. If this view point is right, we can say that the disagreement reflects the system of colloidal crystals is coupled although colloidal particles are weakly bound. In section 3.3.3 we discussed the effect of thermal diffuse scattering on regular reflection. Again, if the dispersion relation of the sample system could be obtained, we can quantitatively analyse the thermal diffuse scattering. It is believed that this phenomenon offers some information about the mode of thermal vibration of the particles.

Chapter 4

Concluding remarks

In chapter 1 the motivations to study colloidal suspensions are described. The model used is a near hard-sphere colloidal system which is found to be a good model to mimic the behaviour of simple atomic systems. In addition, many fascinating phenomena are encountered in the study of colloidal suspensions by the use of light scattering experiments, for example, the diffusion of the particles, phase transitions, and the kinetics and mechanism of crystallisation.

The diffusion processes of colloidal particles is investigated by dynamic light scattering, as presented in chapter 2. The idea of studying particle diffusion is initially from the explanation for fluctuating speckle patterns which can be observed in a simple light scattering experiment (see section 2.2.1). The concept of electric field autocorrelation function is then introduced to interpret this phenomenon (fluctuating patterns). This leads to an attempt to formulate a theory about the scattered electric field amplitude. As a result, the feature of single particle form factor is found to imply the feasibility to characterise the sample system qualitatively, as described in section 2.2. The scattered electric field autocorrelation function is processed to analyse the data. In order to obtain quantitative results, we worked out the theory [18] based on a model shown in section 2.3.4. The experimental results therefore can be sufficiently (qualitatively

and quantitatively) explained. We also attempted to fractionate a polydisperse system. Unfortunately, this experiment was not successful. However, if there is a large amount of stock solution of polydisperse system, it is still worth doing the fractionation experiment.

The main contribution to this thesis is reported in chapter 3. The arduous part is to work out the theory developed by A. J. C. Wilson [50], taking about three months (the details are presented in section 3.3.2). This complicated theory gives a very simple and intriguing result, as presented in eq. (3.19). The aim of this theoretical study is to interpret the scattering pattern from close-packed random-stacked crystals formed in highly concentrated near hard-sphere colloidal suspensions. It is well known that the free energy differences between the *fcc* and *hcp* structures are extremely small [45][46]. To our knowledge, there is no calculation that can clearly find the differences in free energies between these two perfect close-packed structures. The experimental results, shown in section 3.4.3, suggest that the *fcc* structure is slightly more stable than the *hcp* one.

Near hard-sphere colloidal crystals are found to change their structures with time, as shown in section 3.4.4. We attempted to use ripening phenomenon of crystallites to interpret these results. Due to inevitable statistical fluctuations, it is believed that the crystallites formed are polydisperse. As a result, the growth of the bigger crystals is at the expense of the smaller ones so as to decrease the free energy of the system, known as "Ostwald ripening" [67]. We then surmise that for the bigger crystals the late joining layers (after ripening starts) are inclined to become *fcc* like. This then gives a complex structure, as discussed in section 3.4.5.

We reported these new findings concerned with crystal structures and offered possible explanations. However, to test these arguments, it is necessary to study the nucleation and growth processes in detail. It also might be interesting to study the thermal diffuse

scattering from colloidal crystals. In chapter 3 the experimental results show that the collective motion of the particles in colloidal crystals should not be ignored. However, to do this, the dispersion relation has to be developed and the velocity of acoustic shear wave (phonon) in colloidal crystals needs to be estimated. Once these data are available, it might be possible to understand the mode of thermal vibration of the particles in colloidal crystals. In addition, so far it is not clear whether the polydispersity and slight softness of colloidal particles influence the structure of colloidal crystals or not. Therefore, it is necessary to study the effect of different interparticle interaction in detail.

Appendices

Appendix A

Derivation of equation (2.10)

The displacement of the particle during the time increment δt will vary from one interval to the next so that there will be a distribution of jump lengths. According to the central limit theorem of probability theory that the distribution of sample means taken from a large population approaches a normal (Gaussian) curve, the probability for a particle to suffer a displacement in the neighbourhood dV of r should be the Gaussian distribution:

$$G_s(r,\tau) = \left[\frac{2\pi}{3}\left\langle \triangle r^2(\tau)\right\rangle\right]^{-3/2} \exp\left[\frac{-3r^2}{2\left\langle \triangle r^2(\tau)\right\rangle}\right] \tag{A.1}$$

where $\langle \triangle r^2(t)\rangle$ is the mean-square displacement of the particle in the time t. Therefore

$$\langle \exp i\mathbf{Q}\cdot[\mathbf{r}(t)-\mathbf{r}(t+\tau)]\rangle = \int_V dV G_s(r,\tau)\exp[i\mathbf{Q}\cdot\mathbf{r}(\tau)] \tag{A.2}$$

where the domain of this integration, V, is approached to infinity and dV can be taken as $r^2\sin\theta d\theta d\phi dr$. Therefore, equation (A.2) can be rewritten as

$$\langle \exp i\mathbf{Q}\cdot[\mathbf{r}(t)-\mathbf{r}(t+\tau)]\rangle = \left(\frac{\pi}{\rho}\right)^{-3/2}\int_{r=0}^{\infty}\int_\theta\int_\phi r^2\sin\theta d\theta d\phi dr e^{-\rho r^2}e^{i(Qr\cos\theta)}$$

$$= \left(\frac{\pi}{\rho}\right)^{-3/2} \frac{4\pi}{Q} \int_0^\infty r \sin(Qr) e^{-\rho r^2} dr \tag{A.3}$$

where $\rho = \frac{3}{2\langle \Delta r^2(\tau) \rangle}$. This can be evaluated further by expanding $\sin(Qr)$ by power series and then using Gaussian integral. The resulting form is quite simple:

$$\langle \exp i\mathbf{Q} \cdot [\mathbf{r}(t) - \mathbf{r}(t+\tau)] \rangle = \exp\left(\frac{-Q^2 \langle \Delta r^2(\tau) \rangle}{6}\right) \tag{A.4}$$

Appendix B

Derivation of the relation between $\left\langle \triangle r^2(\tau) \right\rangle$ and D

Here we reproduce the derivation of velocity autocorrelation function and the correlation between mean square displacement and diffusion coefficient which can be found in reference [22] and [24]. As mentioned in section 2.2.2, the random displacement $\triangle r(\tau)$ is the time integration of the particle's velocity $v(t)$ that is

$$\triangle r(\tau) = \int_0^\tau dt v(t) \tag{B.1}$$

The mean-square displacement is therefore

$$\left\langle \triangle r^2(\tau) \right\rangle = \int_0^\tau dt_2 \int_0^\tau dt_1 \left\langle v(t_1) v(t_2) \right\rangle \tag{B.2}$$

In order to evaluate this equation we have to consider the following properties [22]:

- $\langle \mathbf{v}(t) \cdot \mathbf{v}(t+\tau) \rangle$ is independent of the origin of time

$\langle \mathbf{v}(t) \cdot \mathbf{v}(t+\tau) \rangle = \langle \mathbf{v}(0) \cdot \mathbf{v}(\tau) \rangle$ because $\mathbf{v}$ is a stationary random process.

- $\langle \mathbf{v}(0) \cdot \mathbf{v}(t) \rangle \to 0$ as $t \to \infty$

because as time increasing $\mathbf{v}(0)$ and $\mathbf{v}(\tau)$ become uncorrelated shortly.

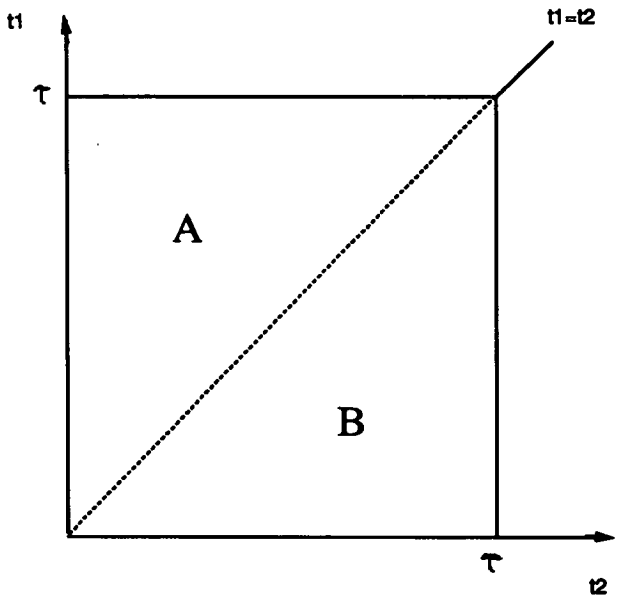

Figure B.1. The domain of integration of the integral in Eq.(B.2) is the square.

- $\langle \mathbf{v}(0) \cdot \mathbf{v}(\tau) \rangle$ is an even function of time

Now let's start working out this derivation. At first we have to consider the domain of integration of the integral in equation (B.2). The domain of integration in the t_1-t_2 plan is shown in figure B-1. Subregion A is defined by $t_2 < t_1$ and subregion B defined by $t_1 < t_2$. Integration of $\langle \mathbf{v}(t_1) \cdot \mathbf{v}(t_2) \rangle$ over A and B must give the same result. Consequently, equation (B.2) can be simplified to

$$\left\langle \triangle r^2(\tau) \right\rangle = 2 \int_0^{\tau} dt_2 \int_0^{t_2} dt_1 \, \langle v(0) v(t_2 - t_1) \rangle \tag{B.3}$$

Changing variables to $t = t_2 - t_1$ which has limits $(t_2, 0)$ gives

$$\left\langle \triangle r^2(\tau) \right\rangle = 2 \int_0^{\tau} dt_2 \int_0^{t_2} dt \, \langle v(0) v(t) \rangle \tag{B.4}$$

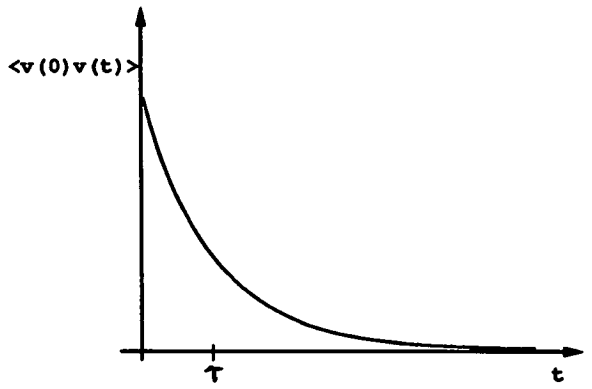

Figure B.2. The schematic plot of velocity autocorrelation function against time

Set $f(t_2) = \int_0^{t_2} dt \, \langle v(0)v(t) \rangle$, and use integration by parts with

$u = f(t_2), dv = dt_2$

$du = df(t_2), v = t_2$

Therefore,

$$\left\langle \triangle r^2(\tau) \right\rangle = 2t_2 f(t_2)|_0^\tau - 2\int_0^\tau t_2 df(t_2)$$

$$= 2\int_0^\tau (\tau - t) dt \, \langle v(0)v(t) \rangle \tag{B.5}$$

The time scale, τ, we were looking at in a DLS experiment is far larger than the correlation time τ^* which is correspondent to fluctuating function $F'(t)$ (see section 2.2.3). This correlation time τ^* characterised the rate at which $F'(t)$ varies between two successive maxima of the fluctuating function $F'(t)$. It is also called inertial relaxation time (see section 2.3.4). The schematic plot of correlation function against time is illustrated in figure (B-2). Consequently, for $t \to \infty$, $\langle v(0)v(t) \rangle \to 0$. However, $\tau \gg t$ and equation (B.5) can be rewritten to give

$$\left\langle \triangle r^2(\tau) \right\rangle = 2\tau \int_0^\infty dt \, \langle v(0)v(t) \rangle \tag{B.6}$$

To evaluate equation (B-6), the calculation requires a knowledge of velocity autocorrelation function. In section 2.2.3 we have indicateded the resulting form of $v(t)$ shown in eq. (2.18). The velocity autocorrelation function can be written as

$$\langle v(0)v(t) \rangle = \langle v(0)v(0) \rangle \exp\left[-\frac{\xi}{M}t\right] + \int_0^t dt' \, \langle v(0)F'(t') \rangle \exp\left[-\frac{\xi}{M}(t-t')\right] \qquad \text{(B.7)}$$

The second term of right-hand side can be ignored because it is usually assumed that the random force $F'(t')$ is uncorrelated with the initial velocity. Therefore,

$$\langle v(0)v(t) \rangle = \langle v(0)v(0) \rangle \exp\left[-\frac{\xi}{M}t\right] \qquad \text{(B.8)}$$

Considering the energy equipartition theorem:

$$\frac{1}{2}M < v^2 >= \frac{3}{2}kT \qquad \text{(B.9)}$$

we can obtain $< v^2 >= 3kT/M$, and then using Stokes's law $\xi = 6\pi\eta R$, where η is the viscosity of solvent, R particle's radius. Then equation (B-6) can be evaluated as

$$\left\langle \triangle r^2(\tau) \right\rangle = 6D\tau \qquad \text{(B.10)}$$

where $D = kT/6\pi\eta R$ is the Stokes-Einstein relation.

Appendix C

Schulz particle size distribution

Schulz particle size distribution [18][19] is given to be

$$G(R) = \frac{R^Z}{Z!}\left(\frac{Z+1}{\overline{R}}\right)^{Z+1} \exp\left[-\frac{R}{\overline{R}}(Z+1)\right] \tag{C.1}$$

where

$$\overline{R^n} \equiv \int R^n G(R) dR \tag{C.2}$$

Considering $R = \overline{R} + \triangle R = \overline{R}\left(1 + \frac{R-\overline{R}}{\overline{R}}\right)$,

$$\begin{aligned} \overline{R^n} &= \int \overline{R}^n \left(1 + \frac{\triangle R}{\overline{R}}\right)^n G(R) dR \\ &= \overline{R}^n \int \left[1 + \frac{\triangle R}{\overline{R}} + \frac{n(n-1)}{2}\frac{\triangle R^2}{\overline{R}^2} + ...\right] G(R) dR \\ &= \overline{R}^n \left(1 + \frac{n(n-1)}{2}\mu_2 + ...\right) \end{aligned} \tag{C.3}$$

where

$$\mu_n \equiv \int \left(\frac{R-\overline{R}}{\overline{R}}\right)^n G(R) dR, \tag{C.4}$$

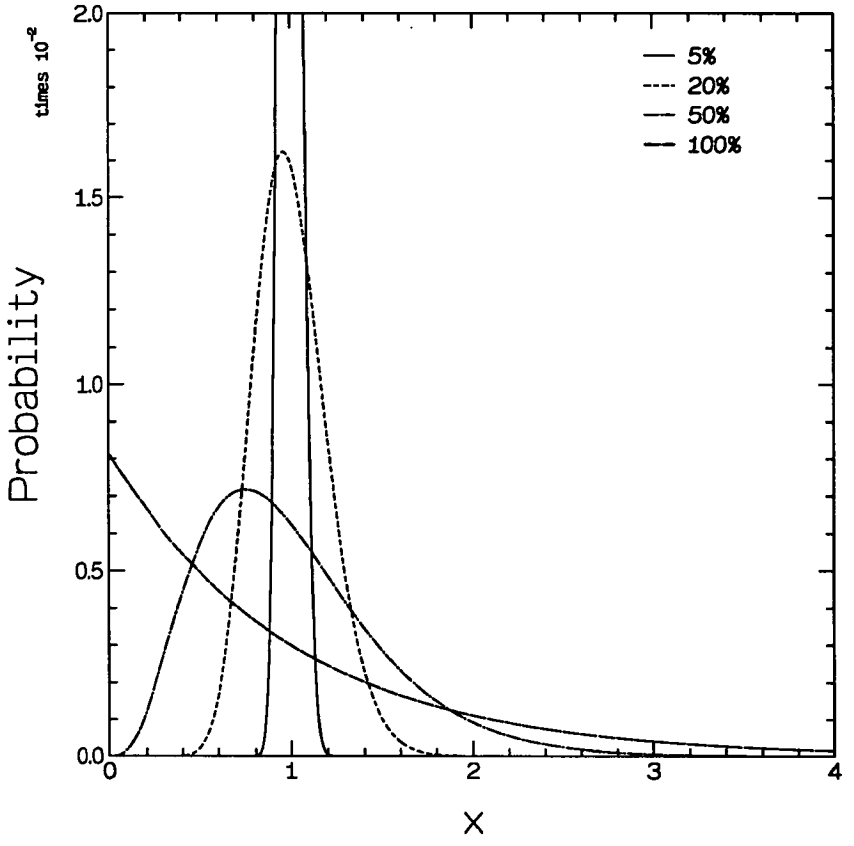

Figure C.1. Schulz particle size distribution for several polydispersities. $x = \frac{R}{\overline{R}}$.

and $\mu_1 = 0$. Therefore, the polydispersity σ, which is the relative standard deviation of the particle size distribution, is related to the parameter Z by

$$\sigma^2 \equiv \frac{\overline{R^2} - \overline{R}^2}{\overline{R}^2} = \frac{1}{Z+1} = \mu_2 \tag{C.5}$$

In addition, skewness s is defined as μ_3/σ^3.

In section 2.3.4 we discussed the effective diffusion coefficient. Here we discuss eq. (2.35) in detail. If considering continuous particle size distribution $G(R)$, where $G(R)$ and $G(\Gamma)$ are correlated because $\Gamma = DQ^2$ and $D = kT/6\pi\eta R$, then eq. (2.27) can be

written as

$$g^{(1)}(\tau) = \frac{\int_0^\infty R^6 P(QR)\exp[-D(R)Q^2\tau]G(R)dR}{\int_0^\infty R^6 P(QR)G(R)dR} \tag{C.6}$$

If expanding the exponential part of equation (C.6) by power series, one can obtain:

$$g^{(1)}(\tau) = 1 + (-\bar{D}Q^2)\tau + \frac{1}{2}(\overline{D^2}Q^4)\tau^2 + ... \tag{C.7}$$

where

$$\overline{D^n} = \frac{\int_0^\infty R^6 P(QR)D^n G(R)dR}{\int_0^\infty R^6 P(QR)G(R)dR}. \tag{C.8}$$

Considering the specific case that $Q \to 0$, then $P(QR) \to 1$. Thus,

$$\overline{D^n(0)} = \frac{\int R^6 D^n G(R)dR}{\int R^6 G(R)dR} \tag{C.9}$$

where $D = kT/6\pi\eta R$. For $n = 1$,

$$\overline{D(0)} = \frac{kT}{6\pi\eta\frac{\overline{R^6}}{\overline{R^5}}} \tag{C.10}$$

where $\frac{\overline{R^6}}{\overline{R^5}}$ is the apparent radius at $Q = 0$. In order to evaluate $\ln g^{(1)}(\tau)$, we set $x = (-\bar{D}Q^2)\tau + \frac{1}{2}(\overline{D^2}Q^4)\tau^2 + ...$, and then $\ln(1+x) = x - \frac{1}{2}x^2 + ...$ The result becomes clear:

$$\ln g^{(1)}(\tau) = -(\bar{D}Q^2)\tau + \left(\frac{\overline{D^2} - \overline{D}^2}{2}\right)Q^4\tau^2 + ... \tag{C.11}$$

Therefore, the initial decay of the first order correlation function declared in equation (C.11) is

$$\kappa_1 = \bar{D}Q^2 \tag{C.12}$$

Note that if one calculates $\kappa_2 / (\kappa_1)^2$ which was indicated in section 2.3.2, one can get

$$\frac{\kappa_2}{(\kappa_1)^2} = \frac{\overline{D^2} - \overline{D}^2}{\overline{D}^2} = \frac{\overline{\Gamma^2} - \overline{\Gamma}^2}{\overline{\Gamma}^2} \tag{C.13}$$

which is the standard deviation of decay rate, $\Gamma(R)$, divided by its mean.

Appendix D

Calculation of equation (3.10)

Between the difference and the differential calculus exist some remarkable analogies. Therefore, corresponding to the theory of differential equations there is a theory of difference equations. The details of this theory can be found in, for example, reference [70].

in chapter 3, one of the important goals is to solve eq. (3.10):

$$P_m + \alpha P_{m-1} - (1 - 2\alpha)P_{m-2} = \alpha, \tag{D.1}$$

a linear difference equation. Let us set $k = m - 2$, then (D.1) can be written as

$$P_{k+2} + \alpha P_{k+1} - (1 - 2\alpha)P_k = \alpha \tag{D.2}$$

To find the general solution of (D.2), it is necessary to find the complementary solution [i.e. the general solution of the homogeneous equation with zero right-hand side] and a particular solution. Firstly, let us solve this homogeneous linear difference equation:

$$P_{k+2} + \alpha P_{k+1} - (1 - 2\alpha)P_k = 0 \tag{D.3}$$

which can be expressed as $[E^2 + \alpha E - (1 - 2\alpha)]\, P_k = 0$ by adopting operator E. The auxiliary equation is $r^2 + \alpha r - (1 - 2\alpha) = 0$. The roots are

$$r = \frac{-\alpha + \sqrt{\alpha^2 - 8\alpha + 4}}{2}, \frac{-\alpha - \sqrt{\alpha^2 - 8\alpha + 4}}{2}$$

Set $\rho_e = \frac{-\alpha+\sqrt{\alpha^2-8\alpha+4}}{2}$ and $\rho_0 = \frac{-\alpha-\sqrt{\alpha^2-8\alpha+4}}{2}$. Corresponding to the roots ρ_e and ρ_0, we have the complementary solution $Q_e\rho_e^k + Q_0\rho_o^k$ [70] where coefficients Q_e and Q_0 can be decided by reference to boundary conditions. We then consider the particular solution which is $P_k = c$ because the right-hand side of (D.2) is a constant. Thus, $c + \alpha c - (1 - 2\alpha)c = \alpha$ leads to $c = \frac{1}{3}$. Accordingly, The general solution of (D.2) is

$$P_k = \frac{1}{3} + Q_e\rho_e^k + Q_0\rho_0^k \tag{D.4}$$

Recall the boundary conditions:$P_0 = 1$ and $P_1 = 0$. We can obtain the simultaneous equations:

$$\begin{cases} \frac{1}{3} + Q_e + Q_0 = 1 \\ \frac{1}{3} + Q_e\rho_e + Q_0\rho_0 = 0 \end{cases} \tag{D.5}$$

Then Q_e and Q_0 can be easily solved to give

$$\begin{aligned} Q_e &= \tfrac{1}{3}\left(1 - \tfrac{1-\alpha}{\sqrt{\alpha^2-8\alpha+4}}\right) \\ Q_0 &= \tfrac{1}{3}\left(1 + \tfrac{1-\alpha}{\sqrt{\alpha^2-8\alpha+4}}\right) \end{aligned} \tag{D.6}$$

Appendix E

Justification of P_m which is real

In section 3.3.2 we briefly described P_m. Here we will discuss P_m comprehensively. Recall eq. (3.11)

$$P_m = \frac{1}{3} + Q_e {\rho_e}^m + Q_o {\rho_o}^m \tag{E.1}$$

where $\rho_e = [-\alpha + \sqrt{4 - 8\alpha + \alpha^2}]/2$, $\rho_o = -[\alpha + \sqrt{4 - 8\alpha + \alpha^2}]/2$, and Q_e, Q_o are chosen to satisfy the boundary conditions. The values are found to be

$$Q_e = \frac{1}{3}\left[1 - \frac{1-\alpha}{\sqrt{4 - 8\alpha + \alpha^2}}\right]$$
$$Q_o = \frac{1}{3}\left[1 + \frac{1-\alpha}{\sqrt{4 - 8\alpha + \alpha^2}}\right]$$

Because $0 \leq \alpha \leq 1$, we found $\rho_{'s}$ and $Q_{'s}$ become complex if $\alpha > 4 - 2\sqrt{3}$. Let us consider the case that $\rho_{'s}$ and $Q_{'s}$ are complex. We can write

$$\rho_{'s} = \frac{-\alpha \pm i\sqrt{|4 - 8\alpha + \alpha^2|}}{2} = -a \pm bi \tag{E.2}$$

where $a = \frac{\alpha}{2}$, $b = \frac{1}{2}\sqrt{|4 - 8\alpha + \alpha^2|}$. Then the expression of $\rho_{\prime s}$ become simple:

$$\begin{aligned}\rho_{\prime s} &= (-1)\sqrt{a^2+b^2}\left(\frac{a}{\sqrt{a^2+b^2}} \mp \frac{b}{\sqrt{a^2+b^2}}i\right) \\ &= (-1)\left(a^2+b^2\right)^{\frac{1}{2}} e^{\mp i\frac{\pi}{x}}\end{aligned}$$

where $\frac{\pi}{x} = \cos^{-1}\left(\frac{b}{\sqrt{a^2+b^2}}\right)$. Therefore,

$$\rho_{\prime s}^m = (-1)^m\left(a^2+b^2\right)^{\frac{m}{2}} e^{\mp i\frac{m\pi}{x}} \tag{E.3}$$

Similarly,

$$\begin{aligned}Q_{\prime s} &= \frac{1}{3}\left[1 - \frac{1-\alpha}{\sqrt{4-8\alpha\pm\alpha^2}}\right] \\ &= \frac{1}{3}\left[1 \pm \frac{1+2a}{2bi}\right]\end{aligned}$$

Eq. (E.1) then can be written to give a real result,

$$\begin{aligned}P_m = \frac{1}{3} + \frac{1}{3}(-1)^m &\left(1 - \frac{1+2a}{2bi}\right)\left(a^2+b^2\right)^{\frac{m}{2}} e^{-i\frac{m\pi}{x}} \\ &+\frac{1}{3}(-1)^m\left(1 + \frac{1+2a}{2bi}\right)\left(a^2+b^2\right)^{\frac{m}{2}} e^{i\frac{m\pi}{x}} \\ = \frac{1}{3} + \frac{1}{3}(-1)^m&\left(a^2+b^2\right)^{\frac{m}{2}}\left[2\cos\frac{m\pi}{x} - \left(\frac{1+2a}{b}\right)\sin\frac{m\pi}{x}\right]\end{aligned}$$

if $\alpha > 4 - 2\sqrt{3}$.

Appendix F

Representation of Q in reciprocal space of hcp structure

In reciprocal space of *hcp* structure, let us construct the axis vectors $\mathbf{B}_1$, $\mathbf{B}_2$, and $\mathbf{B}_3$:

$$\mathbf{B}_1 = 2\pi \frac{\mathbf{a}_2 \times \mathbf{c}}{\mathbf{a}_1 \cdot \mathbf{a}_2 \times \mathbf{c}} = 2\pi \frac{1}{a_1 \cos 30^0} \mathbf{b}_1$$

$$\mathbf{B}_2 = 2\pi \frac{\mathbf{c} \times \mathbf{a}_1}{\mathbf{a}_1 \cdot \mathbf{a}_2 \times \mathbf{c}} = 2\pi \frac{1}{a_2 \cos 30^0} \mathbf{b}_2$$

$$\mathbf{B}_3 = 2\pi \frac{\mathbf{a}_1 \times \mathbf{a}_2}{\mathbf{a}_1 \cdot \mathbf{a}_2 \times \mathbf{c}} = 2\pi \frac{1}{c} \mathbf{b}_3$$

where $a_1 = a_2 = a$, $c = \sqrt{\frac{2}{3}}a$, and $\mathbf{a}_1$, $\mathbf{a}_2$, and $\mathbf{c}$ are crystal-axis vectors of *hcp* structure (refer to figure 3.1). Therefore,

$$\begin{aligned} \frac{\mathbf{Q}}{2\pi} &= h\mathbf{B}_1 + k\mathbf{B}_2 + l\mathbf{B}_3 \\ &= \frac{2}{\sqrt{3}a} \left(h\mathbf{b}_1 + k\mathbf{b}_2 + l\sqrt{\frac{9}{8}}\mathbf{b}_3 \right) \end{aligned}$$

Note that the included angle of $\mathbf{b}_1$ and $\mathbf{b}_2$ is 60^0, and $\mathbf{b}_3$ is normal to $\mathbf{b}_1$ and $\mathbf{b}_2$.

Bibliography

[1] Pusey, P. N. (1991). Colloidal suspensions. In *Liquids, Freezing and the Glass Transition* (J. P. Hansen, D. Levesque and J. Zinn-Justin, eds.), chapt. 10, Elsevier, Amsterdam.

[2] Russel, W. B., D. A. Saville and W. R. Schowalter (1989). *Colloidal Dispersions*, Cambridge University Press, Cambridge.

[3] Pusey, P. N., and W. van Megen (1987). Properties of concentrated suspensions of slightly soft colloidal spheres. In *Complex and Supermolecular Fluids* (S. A. Safran and N. A. Clark, eds.), pp. 673-698, Wiley Interscience.

[4] Jones, R. B., and P. N. Pusey (1991). Dynamics of suspended colloidal spheres. *Annu. Rev. Phys. Chem.*, **42**, 137-169.

[5] Vrij, A. (1976). Polymers at interfaces and the interactions in colloidal dispersions. *Pure Appl. Chem.*, **48**, 471-483.

[6] Fluka chemical and biochemical Catalogue 1993/94, Fluka Chemicals Ltd., England.

[7] Pusey, P. N., and W. van Megen (1986). Phase behaviour of concentrated suspensions of nearly hard colloidal spheres. *Nature*, **320**, 340-342.

[8] Paulin, S. E., and B. J. Ackerson (1990). Observation of a phase transition in the sedimentation velocity of hard spheres. *Phys. Rev. Lett.*, **64**, 2663-2666; with Erratum in *Phys. Rev. Lett.*, **65**, 668 (1990).

[9] Hoover, W. G., and F. H. Ree (1968) Melting transition and communal entropy for hard spheres. *J. Chem. Phys.*, **49**, 3609-3617.

[10] Alder, B. J., W. G. Hoover, and D. A. Young (1968). Studies in molecular dynamics. V. High-density equation of state and entropy for hard disks and spheres. *J. Chem. Phys.*, **49**, 3688-3696.

[11] Kirkwood, J. G. (1939). Molecular distribution in liquids. *J. Chem. Phys.*, **7**, 919-925.

[12] Baus, M. (1987). Statistical mechanical theories of freezing: An overview. *J. Stat. Phys.*, **48**, 1129-1146.

[13] Wertheim, M. S. (1963). Exact solution of the Percus-Yevick integral equation for hard spheres. *Phys. Rev. Lett.*, **10**, 321-323.

[14] Frenkel, D. (1993). Order through disorder: entropy strikes back. *Phys. World*, 24-25.

[15] Ackerson, B. J. (1993). When order is disordered. *Nature*, **365**, 11-12.

[16] Dickinson, E., and R. Parker (1985). Polydispersity and the fluid-crystalline phase transition. *J. Physique Lett.*, **46**, L-229 - L-232.

[17] Pusey, P. N. (1987). The effect of polydispersity on the crystallization of hard spherical colloids. *J. Physique*, **48**, 709-712.

[18] Pusey, P. N., and W. van Megen (1984). Detection of small polydispersities by photon correlation spectroscopy. *J. Chem. Phys.*, **80**, 3513-3520.

[19] Aragón, S. R., and R. Pecora (1976). Theory of dynamic light scattering from polydisperse systems. *J. Chem. Phys.*, **64**, 2395-2404.

[20] Pusey, P. N., and J. M. Vaughan (1975). Light scattering and intensity fluctuation spectroscopy. In *Dielectric and Related Molecular Processes* (M. Davies, ed), Specialist Periodical Report, London: The Chemical Society, **2**, 48-105.

[21] Pusey, P. N., and R. J. A. Tough (1985). Particle interactions. In *Dynamic Light Scattering: Applications of Photon Correlation Spectroscopy* (R. Pecora, ed.), Plenum, New York, 85-179.

[22] Berne, B., and R. Pecora (1976). *Dynamic Light Scattering*, John Wiley and Sons, New York.

[23] Sakurai, J. J. (1985). *Modern Quantum Mechanics*, Benjamin/Cummings.

[24] Reif, F. (1985). *Fundamentals of statistical and thermal physics*, McGraw-Hill, New York.

[25] Fowles, G. R. (1975). *Introduction to Modern Optics.* Holt, Rinehart and Winston, New York.

[26] Koppel, D. E. (1972). Analysis of macromolecular polydispersity in intensity correlation spectroscopy: The method of cumulants. *J. Chem. Phys.*, **57**, 4814-4820.

[27] Rallison, J. M., and E. J. Hinch (1985). The effect of particle interactions on dynamic light scattering from a dilute suspension. *J. Fluid Mech.*, **167**, 131-168.

[28] Ford, N. C., Jr. (1985). Light scattering apparatus. In *Dynamic Light Scattering:Applications of Photon Correlation Spectroscopy* (R. Pecora, ed.), Plenum, New York, 7-58.

[29] Bibette, J. (1991). Depletion interactions and fractionated crystallization for polydisperse emulsion purification. *J. Colloid Interface Sci.*, **147**, 474-478.

[30] Vrij, A., and H. De Hek (1981). Interactions in mixtures of colloidal silica spheres and polystyrene molecules in cyclonhexane. I. Phase separation. *J. Colloid Interface Sci.*, **84**, 409-422.

[31] Gast, A. P., C. K. Hall, and W. B. Russel (1983). Polymer-induced phase separations in nonaqueous colloidal suspensions. *J. Colloid Interface Sci.*, **96**, 251-267.

[32] Patel, P. D., and W. B. Russel (1988). An experimental study of aqueous suspensions containing dissolved polymer. A. Phase separation. *J. Colloid Interface Sci.*, **131**, 192-200.

[33] Lekkerkerker, H. N. W., W. C.-K. Poon, P. N. Pusey, A. Stroobants, and P. B. Warren (1992). Phase behaviour of colloid+polymer mixtures. *Europhys. Lett.*, **20**, 559-564.

[34] Poon, W. C. K., J. S. Selfe, M. B. Robertson, S. M. Ilett, A. D. Pirie, and P. N. Pusey (1993). An experimental study of a model colloid-polymer mixture. *J. Physique II*, **3**, 1075-1086.

[35] Leal Calderon, F., J. Bibette, and J. Biais (1993). Experimental phase diagrams of polymer and colloid mixtures. *Europhys. Lett.*, **23**, 653-659.

[36] Chui, T. T. (1993). Annual research report, The University of Edinburgh.

[37] Segrè, P., W. van Megen, P. N. Pusey, K. Schätzel, and W. Peters (1994). Two colour dynamic light scattering. *J. Mod. Optics*, Submitted.

[38] Zemansky, M. W., and R. H. Dittman (1981). *Heat and Thermodynamics.* McGraw-Hill, New York.

[39] Williams, R., R. S. Crandall, and P. J. Wojtowicz (1976). Melting of crystalline suspensions of polystyrene spheres. *Phys. Rev. Lett.*, **37**, 348-351.

[40] Stiffler, S. R., M. O. Thompson, and P. S. Peercy (1988). Supercooling and nucleation of Silicon after laser melting. *Phys. Rev. Lett.*, **60**, 2519-2522.

[41] Guinier, A. (1963). *X-Ray Diffraction*, Freeman, New York.

[42] Hansen, J. P., and I. R. McDonald (1986). *Theory of Simple Liquids*, Academic Press, London.

[43] Kittel, C. (1986). *Introduction to solid state physics*, John Wiley and Sons, Singapore.

[44] Schwartz, L. H., and J. B. Cohen (1977). *Diffraction from materials*, Academic press, New York.

[45] Colot, J. L., and M. Baus (1985). The freezing of hard spheres II. A search for structural (f.c.c.-h.c.p.) phase transitions. *Molec. Phys.*, **56**, 807-824.

[46] Iglói, F. (1986). Density functional theory of freezing of the hard sphere liquid into FCC against HCP structures. *J. Phys. C*, **19**, 6907-6914.

[47] Edwards, O. S., H. Lipson, and A. J. C. Wilson (1941). Structure of cobalt, *Nature*, **148**, 165.

[48] Edwards, O. S., and H. Lipson (1942). Imperfections in the structure of cobalt I. Experimental work and proposed structure. *Proc. Roy. Soc.* London, **A 180**, 268-276.

[49] Sanders, J. V. (1967). Diffraction of light by opals. *Acta Cryst.*, **A 24**, 427-434.

[50] Wilson, A. J. C. (1942). Imperfections in the structure of cobalt II. Mathematical treatment of proposed structure. *Proc. Roy. Soc.* London, **A 180**, 277-284.

[51] Wilson, A. J. C. (1949). *X-Ray Optics*, Methuen, London.

[52] Vrij, A. (1978). Light scattering of a concentrated multicomponent system of hard spheres in the Percus-Yevick approximation. *J. Chem. Phys.*, **69**, 1742-1747.

[53] Vrij, A. (1979). Mixtures of hard spheres in the Percus-Yevick approximation. Light scattering at finite angles. *J. Chem. Phys.*, **71**, 3267-3270.

[54] van Beurten, P., and A. Vrij (1981). Polydispersity effects in the small-angle scattering of concentrated solutions of colloidal spheres. *J. Chem. Phys.*, **74**, 2744-2748.

[55] Zachariasen, W. H. (1940). A theoretical study of the diffuse scattering of x-rays by crystals. *Phys. Rev.*, **57**, 597-602.

[56] Helmholdt, R. B., and A. Vos (1976). Errors in atomic parameters and in electron density distribution due to thermal diffuse scattering of x-rays. *Acta Cryst.*, **A 33**, 38-45.

[57] James, R. W. (1958). *The optical principles of the diffraction of x-rays,* G. Bell and Sons, London.

[58] Warren, B. E. (1990). *X-ray diffraction,* Dover, New York.

[59] Joanny, J. F. (1979). Acoustic shear waves in colloidal crystals. *J. Colloid Interface Sci.*, **71**, 622-624.

[60] Born, M. (1942-3). Theoretical investigations on the relation between crystal dynamics and x-ray scattering. *Rep. Prog. Phys.*, **9**, 294-333.

[61] Lonsdale, K. (1948). *Crystals and x-rays,* G. Bell & Sons, London.

[62] Wilson, A. J. C. (1949). X-ray diffraction by random layers: Ideal line profiles and determination of structure amplitudes from observed line profiles. *Acta. Cryst.*, **2**, 245-251.

[63] Brindley, G. W., and J. Méring (1951). Diffractions des rayons X par les structures en couches désordonnées. I. *Acta. Cryst.*, **4**, 441-446.

[64] Young, D. A., and B. J. Alder (1974). Studies in molecular dynamics. XIII. Singlet and pair distribution functions for hard-disk and hard-sphere solids. *J. Chem. Phys.*, **60**, 1254-1267.

[65] Pusey, P. N., W. van Megen, P. Bartlett, B. J. Ackerson, J. G. Rarity and S. M. Underwood (1989). Structure of crystals of hard colloidal spheres. *Phys. Rev. Lett.*, **63**, 2753-2756.

[66] Verlet, L.,and J. J. Weis (1972). Equilibrium theory of simple liquids. *Phys. Rev.*, **A5**, 939-952.

[67] Kahlweit, M. (1975). Ostwald ripening of precipitates. *Adv. Colloid Interface Sci.*, **5**, 1-35.

[68] Smits, C. (1991). Ph.D. thesis, University of Utrecht.

[69] Strickland-Constable, R. F. (1968). *Kinetics and Mechanism of Crystallization*, Academic, London.

[70] Spiegel, M. R. (1971). *Finite Differences and Difference Equations*, McGraw-Hill, New York.